

# **Design of a Broadband Array Using the Foursquare Radiating Element**

Carey G. Buxton

Dissertation submitted to the Faculty of the Virginia  
Polytechnic Institute and State University in partial  
fulfillment of the requirements for the degree of

Doctor of Philosophy  
in  
Electrical and Computer Engineering

Warren L. Stutzman, Chair  
William A. Davis  
Tim Pratt  
Ahmad Safaai-Jazi  
Lee Johnson

June 12, 2001  
Blacksburg, Virginia

Keywords: Broadband Arrays, Finite Arrays, Infinite  
Arrays

Copyright 2001, Carey G. Buxton

# Design of a Broadband Array Using the Foursquare Radiating Element

Carey G. Buxton

(ABSTRACT)

Broadband scanning arrays require small element spacing over a broad frequency band to achieve the desired scan capabilities. Previous research has concentrated on the development of small broadband elements to meet the demands of broadband arrays. However, mutual coupling between elements in a tightly spaced array can change the operating frequency and bandwidth from that of the single isolated element. Several research efforts have focused on minimizing the mutual coupling to maintain the frequency response of the single isolated element. This dissertation focuses on using the strong coupling between Foursquare antennas to obtain the broadband frequency response while maintaining a small element spacing.

The isolated Foursquare antenna was modeled using an in-house FDTD code. The modeled current distribution over the frequency band of operation revealed how the antenna achieved a broadband frequency response. Because of this understanding of the single element, the downward shift in the frequency response of the Foursquare antenna in a fully active array could be anticipated. Furthermore, the infinite array models of the Foursquare revealed an increase in bandwidth. Both are desirable characteristics for a broadband scanning array. Therefore, through this research using the Foursquare element, it has been shown that the strong mutual coupling in a tightly spaced array can have advantages if initially taken into consideration when designing the array.

## ACKNOWLEDGEMENTS

I would like to thank Dr. Warren Stutzman for supporting my research ideas when at times I am sure they seemed bizarre and thereby allowing me the freedom to do independent research. I would like to thank Dr. William Smith for his support, encouragement and friendship above and beyond anything that is required or expected from a previous masters advisor. I would also like to thank Dr. Stephen Gedney for enthusiastically giving of his time to answer my questions about FDTD and only asking in return that I be a good representative for the University of Kentucky.

I want to give credit to my older siblings, Amy, Meg, Chris and Pat who always believed that I could do anything. My parents, Susan and Jack Buxton who gave me the strength and self-confidence to pursue my dreams and who taught me the value of the pursuit of knowledge. I want to also thank the next generation of women in my family (Clayre, Alex, Lauren and Gwynne) for motivating me to set the best possible example in order that I may be as valuable of a role model to them as their mothers and grandmother were to me. I would like to thank my husband, Charlie Symons, for being extremely supportive and patient throughout my education.

# CONTENTS

<b>Acknowledgements</b> .....	iii
<b>List of Figures</b> .....	v
<b>List of Tables</b> .....	viii
<i>Chapter 1</i> <b>Introduction</b> .....	1
<i>Chapter 2</i> <b>Broadband Array Elements</b> .....	6
<b>2.1</b> Arrays of Open-ended Waveguide Elements.....	9
<b>2.2</b> Multifunctional Arrays .....	10
<b>2.3</b> Tapered Slot Antennas.....	11
<b>2.4</b> Microstrip Patch Antennas.....	14
<b>2.5</b> Low-Profile Broadband Array Elements .....	16
<b>2.5.1</b> Planar Equiangular Spiral Antenna.....	16
<b>2.5.2</b> Archimedean Spiral Antenna.....	18
<b>2.5.3</b> Sinuous Antenna .....	19
<b>2.5.4</b> Foursquare Antenna .....	20
<b>2.6</b> Summary .....	22
<i>Chapter 3</i> <b>Array Bandwidth</b> .....	23
<b>3.1</b> Wideband Array and Element Principles .....	24
<b>3.2</b> Low-profile Wideband Radiating Elements .....	30
<b>3.3</b> Summary.....	33
<i>Chapter 4</i> <b>Finite Difference Time Domain Method (FDTD)</b> .....	35
<b>4.1</b> Absorbing Boundary Conditions (ABC's) and Update Equations ...	36
<b>4.2</b> Far-field Pattern Calculations .....	38
<b>4.3</b> Antenna Specifications .....	41
<b>4.4</b> Antenna Characteristics .....	42
<b>4.5</b> Infinite Array.....	43
<b>4.6</b> Summary.....	45
<i>Chapter 5</i> <b>Foursquare Antenna</b> .....	46
<b>5.1</b> The Foursquare Element Geometry .....	47
<b>5.2</b> The Foursquare Element Experimental Results .....	49
<b>5.2.1</b> Measured Far-field Patterns .....	49
<b>5.2.2</b> Measured Input Impedance .....	52
<b>5.3</b> FDTD Model Results for the Foursquare Antenna .....	56
<b>5.3.1</b> Modeled Far-field Patterns .....	56
<b>5.3.2</b> Modeled Input Impedance.....	65

<b>5.3.3</b>	Modeled Current Distribution .....	66
<i>Chapter 6</i>	<b>Characteristics of Strongly Coupled Finite Arrays</b> .....	74
<b>6.1</b>	Active Element Pattern .....	75
<b>6.2</b>	Power Loss in Transmission Line Model .....	77
<b>6.3</b>	An Array of Three Half-Wave Dipoles .....	80
<b>6.3.1</b>	Input Impedance .....	82
<b>6.3.2</b>	Scanning a Parallel Dipole Array .....	86
<b>6.4</b>	Pattern Compensation Example Using a Cardioid Pattern.....	90
<b>6.5</b>	Summary .....	92
<i>Chapter 7</i>	<b>The Foursquare as a Finite Array Element</b> .....	94
<b>7.1</b>	Far-field Patterns of 3x3 Foursquare Array .....	95
<b>7.2</b>	Far-field Pattern Scanning .....	102
<b>7.3</b>	Input Impedance of the 3x3 Foursquare Array .....	109
<i>Chapter 8</i>	<b>Infinite Array of Foursquare Elements</b> .....	111
<b>8.1</b>	Geometry of Arrays Investigated .....	111
<b>8.2</b>	FDTD Model for Infinite Array Computations .....	112
<b>8.3</b>	Investigation of Height Above Ground Plane .....	113
<b>8.4</b>	Element Spacing Variation Effects .....	116
<b>8.5</b>	Summary .....	119
<i>Chapter 9</i>	<b>Summary and Conclusions</b> .....	120
	<b>References</b> .....	123
	<b>Vita</b> .....	126

## LIST OF FIGURES

Figure 2.1: . Open-ended waveguide aperture dimensions.....	10
Figure 2.2: Tapered slot geometry .....	14
Figure 2.3: Rectangular patch geometry.....	15
Figure 2.4: Rectangular stacked patch geometry .....	16
Figure 2.5: Equiangular spiral geometry .....	18
Figure 2.6: Archimedean spiral antenna geometry .....	19
Figure 2.7: Sinuous geometry .....	20
Figure 2.8: Foursquare antenna geometry .....	21
Figure 3.1: Minimum element spacing ( $d=D$ ) normalized to wavelength as function of normalized frequency for various element types. ....	29
Figure 4.1: Unit cell of two dimensional infinite array .....	44
Figure 5.1: Geometry of the prototype Foursquare antenna.....	48
Figure 5.2: Foursquare feed connections through a $0^\circ/180^\circ$ hybrid to create a balanced feed for pattern measurements .....	50
Figure 5.3: Measured E-plane pattern of the prototype Foursquare antenna of Fig. 5.1.....	51
Figure 5.4: Measured H-plane pattern of the prototype Foursquare antenna of Fig. 5.1 .....	52
Figure 5.5: Two port circuit model of the Foursquare antenna and Feed.....	53
Figure 5.6: Measured and modeled input impedance and VSWR for the prototype Foursquare antenna of Fig. 5.1 .....	55
Figure 5.7: Calculated and measured E-plane patterns of the Foursquare antenna of Fig. 5.1 at 4.5 GHz.....	57
Figure 5.8: Calculated and measured E-plane patterns of the Foursquare antenna of Fig. 5.1 at 6.0 GHz.....	58
Figure 5.9: Calculated and measured E-plane patterns of the Foursquare antenna of Fig. 5.1 at 7.25 GHz.....	59
Figure 5.10: Calculated and measured H-plane patterns of the Foursquare antenna of Fig. 5.1 at 4.5 GHz.....	60
Figure 5.11: Calculated and measured H-plane patterns of the Foursquare antenna of Fig. 5.1 at 6.0 GHz.....	61
Figure 5.12: Calculated and measured H-plane patterns of the Foursquare antenna of Fig. 5.1 at 7.25 GHz.....	62
Figure 5.13: Computed $45^\circ$ plane, E-plane and H-plane patterns of the Foursquare antenna of Fig. 5.1 at 4.5 GHz .....	63
Figure 5.14: Computed $45^\circ$ plane, E-plane and H-plane patterns of the Foursquare antenna of Fig. 5.1 at 6.0 GHz .....	64
Figure 5.15: Computed $45^\circ$ plane, E-plane and H-plane patterns of the Foursquare antenna of Fig. 5.1 at 7.25 GHz.....	65
Figure 5.16: Current distribution at 5 GHz on square #1 of the excited pair on the Foursquare antenna of Fig. 5.1 .....	67
Figure 5.17: Current distribution at 5 GHz on square #2 of the parasitic squares on the Foursquare antenna of Fig. 5.1 .....	68

Figure 5.18: Current distribution at 6 GHz on square #1 of the excited pair on the Foursquare antenna of Fig. 5.1 .....	69
Figure 5.19: Current distribution at 6 GHz on square #2 of the parasitic squares on the Foursquare antenna of Fig. 5.1 .....	70
Figure 5.20: Current distribution at 7 GHz on square #1 of the excited pair on the Foursquare antenna of Fig. 5.1 .....	71
Figure 5.21: Current distribution at 7 GHz on square #2 of the parasitic squares on the Foursquare antenna of Fig. 5.1 .....	72
Figure 6.1: Transmission line model of radiation from a two element array .....	78
Figure 6.2: Array of three parallel half-wave dipoles .....	81
Figure 6.3: Tightly spaced three element offset array of 300 MHz resonant dipoles .....	85
Figure 6.4: Calculated input impedance for: (a) a single 300 MHz resonant dipole and (b) the 3 element array of 300 MHz resonant dipoles shown in Fig. 6.3 .....	86
Figure 6.5: Normalized cardioid pattern formed from two parallel resonant dipoles $\lambda/4$ apart with compensated voltages compared to the normalized pattern without compensation. ....	92
Figure 7.1: 3x3 array of Foursquare elements .....	95
Figure 7.2: Calculated E-plane active element patterns for center element of the 3x3 Foursquare array of Fig. 7.1 for frequencies from 2.0 – 4.0 GHz.....	97
Figure 7.3: Calculated H-plane active element patterns for center element of the 3x3 Foursquare array of Fig. 7.1 for frequencies from 2.0 – 4.0 GHz.....	98
Figure 7.4: E-plane pattern of fully active 3x3 Foursquare array for frequencies from 2.0 – 4.0 GHz .....	101
Figure 7.5: H-plane pattern of fully active 3x3 Foursquare array for frequencies from 2.0 – 4.0 GHz .....	102
Figure 7.6: Calculated H-plane patterns of 3x3 Foursquare array for frequencies from 2.0 – 4.0 GHz. The excitation voltage is for a desired scan angle of 30° of 0.52 rad.....	105
Figure 7.7: Calculated H-plane patterns of 3x3 Foursquare array for frequencies from 2.0 – 4.0 GHz. The excitation voltage is for a desired scan angle of 40° of 0.70 rad.....	106
Figure 7.8: Calculated H-plane patterns of 3x3 Foursquare array for frequencies from 2.0 – 4.0 GHz. The excitation voltage is for a desired scan angle of 50° of 0.87 rad.....	107
Figure 7.9: Scanned beam of 3x3 Foursquare array with a voltage phase taper 10 times larger than the expected phase taper for a 30° scanned beam.....	108
Figure 7.10: Active input impedance for 3x3 and infinite Foursquare array .....	110
Figure 8.1: Geometry of infinite array of Foursquare elements.....	113
Figure 8.2: Calculated input impedance and VSWR of infinite array of Foursquare elements with separation between Foursquares twice that of the separation between squares, $W$ , as listed in Geometry I of Table 8.1. The height above the ground plane is $h=7.0$ mm. ....	114
Figure 8.3: Input impedance and VSWR of the infinite array of Foursquare elements with separation between Foursquares twice that of the separation between	

	squares, $W$ , as listed in Geometry II of Table 8.1. The height above the ground plane is $h=12.0$ mm.....	115
Figure 8.4:	Input impedance and VSWR of infinite array of Foursquare elements with separation between Foursquares twice that of the separation between squares, $W$ , as listed in Geometry III of Table 8.1. The height above the ground plane is $h=3.5$ mm.....	116
Figure 8.5:	Input impedance and VSWR of infinite Array of Foursquare elements with element spacing four times that of the feed spacing, $w$ as listed in Geometry IV of Table 8.1. The height above the ground plane is $h=7.0$ mm.....	117
Figure 8.6:	Input impedance and VSWR of infinite Array of Foursquare elements with element spacing four times that of the feed spacing, $w$ as listed in Geometry V of Table 8.1. The height above the ground plane is $h=7.0$ mm.....	118



## LIST OF TABLES

Table 2.1:	Characteristics of antennas commonly found as array elements.....	8
Table 3.1:	Comparison of bandwidth defenitions.....	26
Table 3.2:	Wideband radiating element characteristics.....	32
Table 5.1:	Foursquare parameters.....	48
Table 7.1:	3x3 Foursquare array geometry.....	96
Table 7.2:	3x3 Foursquare array geometry and scan angle.....	103
Table 8.1:	Geometry of Foursquare in an infinite array.....	112

## **INTRODUCTION**

Communication technology is growing at a phenomenal rate and is fueling tremendous expansion in commercial ventures in communications. The average household no longer has just one phone line, but has two phone lines, one of which is a dedicated modem line. This same household will have DSS and/or cable TV. It has become more important to stay in touch even when we are away from home. This has created a huge demand for pagers and cell phones. Ideally users would like PCS, cellular, and GPS communication on there cell phone. This increased consumer demand for information has pushed the design limits of broadband communication networks. Wireless broadband communication systems require broadband antennas to meet the demands for more users and faster data rates. The communication industry would like their satellites to have multiple beams at multiple frequency bands without increasing the size or weight of their satellite. Broadband scanning arrays can accommodate multiple beams over a broad band of frequencies with a single antenna aperture. Broadband, scanning arrays offer the greatest ability to meet the communication industries demands. Because of this demand for broadband, scanning arrays much effort has been devoted to its design.

There are also military applications for broadband scanning arrays. The military also has an increased demand for communication technologies. Military success depends on the ability to operate as a synchronized unit. This requires reliable, secure, high speed communication links. Many military vehicles are crowded with antennas for multiple communication links. The topside of naval ships are heavily populated with antennas, each with a different function. Not only are these antennas used for communication, but they are also used for radar tracking and electronic counter measures. The number of incoming missiles that a radar system can track depends on its ability to have multiple beams scanning the horizon. Arrays which allow frequency and polarization diversity are

also desired to avoid jamming. Broadband array antennas are the military's best option for keeping up with their communication and radar demands.

Broadband scanning arrays are difficult to design because of the conflicting design criterion. The first and most obvious criterion is to find appropriate broadband elements. Broadband elements are typically large compared to narrow band elements, relative to a wavelength, at the highest frequency of operation. This compromise between size and bandwidth makes designing a broadband antenna element a very difficult problem, requiring new and innovative approaches to element design.

Element size is important because it limits how closely elements can be spaced in an array. Element spacing greater than  $\lambda/2$  limits the maximum scan angle of the array; see Chapter 3. If large scan angles are desired, close element spacing is necessary. Ideally less than  $\lambda/2$  spacing over the entire frequency band of operation is desired. Therefore, the element needs to exceed the size requirement at the low end of the frequency band to be able to meet the spacing requirements at the high end of the frequency band.

In addition to size and spacing, the element should have a broad pattern in the E- and H-plane over the entire frequency band. The broad E- and H-plane patterns are necessary to reduce the gain loss at large scan angles. Many broadband antennas have significant pattern variation over their bandwidth. This variation affects the scanning capabilities of the array. If scanning is desired in all directions, the broad beam characteristics must exist in both the E- and H-plane. Many innovative antennas have been designed to meet the criterion listed above; however, there are still more improvements to be made in the area of broadband scanning arrays.

To meet the difficult demands of broadband scanning arrays, most research efforts have concentrated on the design and study of small, broadband, antenna elements as summarized in Chapter 2. Some of these elements include the Archimedean spiral and the equiangular spiral which are both circularly polarized elements. The sinuous and the Foursquare are also very broad band, but have dual linear polarizations. The Vivaldi antenna in its original configuration allowed only linear polarization; however, a dual

polarized configuration has been designed using four Vivaldi elements. All of these small broadband antennas have uniform E- and H- plane patterns.

Instead of designing an array for a single, broad frequency range, some designers have developed antenna arrays with multiple frequency bands to serve different functions. These arrays are referred to as multifunctional arrays. Most of these multifunctional arrays consist of multiple arrays embedded in a single aperture. Each array corresponds to a different frequency band and consists of narrow band elements specifically designed for that frequency band. Multifunctional arrays were the first attempts at limiting space occupied by antennas on military vehicles.

Other designers have taken this approach one step further and designed re-configurable arrays. Re-configurable arrays often use electronic switches to connect several elements of an array to form a single larger element. These larger elements operate at a lower frequency band than the original element. When the switches are off the array operates in the higher frequency band and when the switches are on the array is reconfigured to operate in a lower frequency band.

All the approaches presented above have limitations. Broadband elements are difficult to make in compact form, which limits how closely they can be spaced in an array as discussed in Chapter 3. Multifunctional arrays typically operate in discrete narrow bands. The re-configurable array can only operate in one configuration at a time. Future designs for scanning arrays will require that the array be continuously operational over a continuous broad frequency range. In addition, polarization diverse elements will be necessary for many applications.

Continuous broadband coverage is still the most desirable array design. If the bandwidth of scanning arrays is to be increased, either a very small broadband element is needed or an element that can overlap its adjacent element without interfering with its operation. Because of the wavelength dependency of antennas, making a very small broadband element is physically restrictive, however, overlapping elements are not limited by size.

The Foursquare element in an array was found to have this overlapping property. The strong mutual coupling in the array allowed the single Foursquare element to also radiate

from the surrounding elements in the array, therefore, operating at a lower frequency. The effective increase in size of the element due to mutual coupling, increases the impedance bandwidth and allows a closer array grid spacing.

The FDTD code described in Chapter 4 was used to model the Foursquare element in various array configurations. The FDTD model of the Foursquare element was used to explain the operating characteristics of the Foursquare element (Chapter 5). The FDTD model of the 3x3 array showed an operating frequency shift and distortion in the active element patterns of the Foursquare in the array (Chapter 7). The infinite array FDTD model showed an impedance shift and increased impedance bandwidth of the Foursquare element in an infinite array (Chapter 8). The development of the FDTD code allowed the modeling of the Foursquare antenna and Foursquare array. These models led to the discovery of the following major contributions of this research:

- The broadband operating characteristics of the Foursquare antenna were explained by the strong mutual coupling between the diagonally excited squares and the parasitic squares (Chapter 5)
- Through numerical analysis, a shift in resonant frequency of antennas, in particular the Foursquare antenna, placed in a strongly coupled array was predicted and demonstrated.
- An increase in the effective size of the element due to mutual coupling by radiation from adjacent elements was demonstrated.
- Through numerical analysis, an increase in impedance bandwidth of the Foursquare element in an infinite array due to strong mutual coupling was predicted and demonstrated.
- Through numerical analysis, a decreased element spacing, achieved because of the downward shift in resonant frequency of the element in an array environment, was predicted and demonstrated.

- A numerical methods code was developed, specifically the FDTD code, for modeling the characteristics of the Foursquare antenna in a infinite array.

## **BROADBAND ARRAY ELEMENTS**

Broadband array antennas have been investigated for many years because of their benefits to commercial and military applications. The ideal single antenna operates at any frequency, with a  $90^\circ$  scan capability, polarization diversity and compact size. Though this is not a practical design criterion, the desire for the ideal broadband scanning array element is pushing the design of small antennas that operate over octaves and decades of bandwidth. Broadband array designs have yet to reach the limits of their capabilities. Future innovations in broadband scanning array designs will require designing the entire array as a unit, considering element characteristics, array grid performance, and mutual coupling effects as part of the array design process.




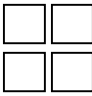



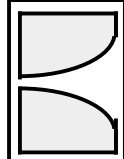
There are several steps to designing a broadband array. The first and most obvious is element selection. Characteristics of selected array elements are summarized in Table 2.1. The array is inherently limited by the bandwidth of the single array element. Therefore, choosing a broad bandwidth element is necessary. The limitation of most broadband elements is that they tend to be larger in size than narrow bandwidth elements relative to a wavelength at the highest frequency of operation. The size of the element limits the minimum element spacing that can be obtained. This in turn limits the scan angle for higher frequencies. Thus, there is a compromise between element bandwidth and element size. In addition to the broad bandwidth requirement, it is desired to have a low profile structure for mounting on the outer surface of vehicles and dual polarization capabilities for many applications. These requirements make designing a broad bandwidth array challenging.

Previous broadband array designs concentrated mainly on selecting broadband antenna elements. Some of the first antennas chosen for use in arrays were open-ended waveguides. To increase the functionality of the array, multiple arrays of open-ended waveguides were placed in a single array aperture. This configuration would operate over several different radar bands and is referred to as a multi-functional array.

The tapered slot antenna, specifically the Vivaldi, was designed to handle a 3:1 bandwidth. The tapered slot can be designed for high power handling capabilities or if etched on substrate can be easily connected to microstrip transmission lines. Some broadband scanning array applications do not require the power handling capabilities of waveguides. These applications may prefer low-profile, low-power, light weight antennas such as the Archimedean spiral, Equiangular spiral, Sinuous and Foursquare antennas. All the antennas mentioned above will be discussed in detail in the following sections.

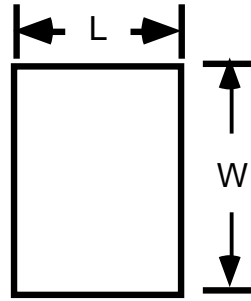


**Table 2.1** Characteristics of antennas commonly found as array elements

Element Type	Element Bandwidth	Beamwidth (HP)	Electrical Size		Polarization
			Diameter	Height	
Archimedean spiral 	~10:1	75	$0.5 \lambda_L$		Circular
Equiangular spiral 	~8:1	70	$0.5 \lambda_L$		Circular
Sinuuous 	~9:1	60-110	$0.4 \lambda_L$		Dual linear
Foursquare 	1.8:1	60-70	$0.35 \lambda_L$	$0.11 \lambda_L$	Dual linear
Microstrip patch 	3%	110	$\frac{0.49}{\sqrt{\epsilon_r}} \lambda_L$	$\ll \lambda_L$	Dual linear
Stacked patch 	40%	65	$\frac{0.40}{\sqrt{\epsilon_r}} \lambda_L$	$0.13 \lambda_L$	Dual linear
Open-ended waveguide 	20%	150	$\frac{0.7 \lambda_L}{\sqrt{\epsilon_r}}$	0	Linear
Vivaldi 	3:1	45-85	$\frac{1.2 \lambda_L}{\sqrt{\epsilon_r}}$	$\frac{2}{\sqrt{\epsilon_r}} \lambda_L$	Linear

## 2.1 Arrays of Open-Ended Waveguide Elements

The open-ended waveguide is the simplest aperture antenna. The aperture fields of a rectangular, open-ended waveguide have a cosine taper in the x-direction (E-plane) and are uniform in the y-direction (H-plane) for the  $TE_{10}$  mode of operation. The beamwidth resulting from the aperture field distribution has a very broad pattern. Early phased arrays consisted of open-ended waveguide elements. Open-ended waveguide elements interfaced well with the waveguide transmission lines and are able to handle high power. However, waveguide apertures have an inherently low bandwidth, limiting the bandwidth of the array. Though the bandwidth of a waveguide for single mode operation is typically around 50% due to VSWR considerations the bandwidth of an open-ended waveguide reduces to as little as 20% [1]. The WR(284) open-ended waveguide has been reported to operate between 2.9 to 3.5 GHz. Therefore at the low frequency of operation the open-ended waveguide dimensions are  $L=0.69\lambda_L$  and  $W=0.33\lambda_L$  as seen in Fig. 2.1. In 1972, Laughlin et al. [2] proposed expanding the bandwidth of the rectangular lattice waveguide array by using an array consisting of triangular grid spaced waveguide and radiators utilizing a dielectric impedance matching transformer on the radiating aperture. This array was able to operate over a frequency band of 3.5-6.6 GHz with a  $\pm 60^\circ$  scan angle. In 1998, Foti et al. [3] proposed expanding the bandwidth of the elements by exciting evanescent mode waveguide cavities with a printed probe near the aperture. In addition, a wide angle, impedance matching (WAIM) sheet was applied to increase scan capability. This design allowed for  $\pm 60^\circ$  scan over an octave with polarization diversity.



Top View

**Figure 2.1** Open-ended waveguide aperture dimensions

## 2.2 Multifunctional Arrays

Multifunctional arrays were developed, in response to the demand for fewer antennas. Multifunctional arrays, unlike broadband arrays, consist of two or more arrays meshed into the same aperture. Each array operates in its own unique band of frequencies. Multi-functional arrays can consist of several types of elements or the same element designed for different frequency bands.

In 1972, Boynes et al. [1] created an array with three operating bands by interlacing an *L*, *S*, and *C* band open-ended waveguide array in a single array aperture. Later, in 1997, Lee et al. [4] created a dual-band, dual-polarized, crossed dipole and cavity backed, disc element array that operated at two separate bands with the bands having a ratio of 2:1. A multi-layered, windowed microstrip implementation was developed by Strickland et al. [5] in 1997 to create a dual-polarized, dual-band array operating in the *L* and *C* bands. Pokuls et al. [6] in 1998 introduced microstrip patches and dual slot elements to create a dual-polarization, dual-band array for use in *C* and *X* band.

Other multi-functional array designs can reconfigure the antenna elements through switches to operate at a specified frequency band. A structurally-integrated, optically-reconfigurable, antenna array, developed and built by Gilbert et al. [7] in 1995 is a reconfigurable array of crossed dipole elements. Optical switches between the crossed

dipole elements are used to short multiple dipoles to form a larger dipole with a lower operating frequency. In this manner the bandwidth of a crossed dipole array can be extended over a large frequency range. The array has three configurations that operate in the 500-900 MHz, 900-1200 MHz and 1.2-2.0 GHz bands with a VSWR under 3.0. The crossed dipole array is mounted over a ground plane. Ideally, the distance above the ground plane is  $1/4\lambda$  for all frequencies. This is effectively accomplished by placing frequency selective surfaces (FSS) at corresponding levels below the cross dipole array. This system has the potential to operate over a very wide bandwidth but is limited by its instantaneous bandwidth of a single frequency band of a dipole array.

These multi-functional systems work well for specific frequency bands, however they do not allow continuous coverage over large frequency bands. In some cases the close proximity of other array elements interferes with the operation of the array due to strong mutual coupling. If the interference is severe, time multiplexing of the array may be necessary. In a re-configurable, multi-functional array time multiplexing is required. Therefore, the operating frequency band of the array is not instantaneous and time multiplexing would be required to take advantage of the entire bandwidth of this array.

### **2.3 Tapered Slot Antennas**

Tapered slot antennas or flared notch antennas are commonly discussed in the literature. The interest in the antenna is due to their small size and characteristically large bandwidth usually around 3:1. These characteristics make the tapered slot a viable antenna element for broadband phased arrays. Depending on the application, the tapered slot antenna can be free standing or etched on a dielectric substrate. Dielectric substrate tapered slot antennas are ideal for connection to microstrip transmission line feeds. In addition, increasing the dielectric value of the substrate can reduce the size of the tapered slot antenna. However, high power applications, such as radar, use a free standing tapered slot antenna because of the increased power handling capabilities.

The tapered slot antenna can have several forms. A linear tapered slot antenna (LTSA) is easily constructed with a linear flare of the slot that is truncated at a distance

corresponding to the length of the antenna. The LTSA is specified by its height and flare angle. The stepped taper is often used in numerical models to approximate a LTSA or Vivaldi. Rather than a continuous linear taper as in the LTSA, the stepped taper is constructed from sections of slots with increasing size chosen to approximate a continuous taper. The Vivaldi antenna is a commonly studied type of tapered slot. The Vivaldi has an exponentially tapered slot for a broad bandwidth with minimal length and mismatch.

Mansky et al. [8] in 1984, Povinelli et al [9] in 1989 and Schaubert et al. [10] in 1994 all recommended notch antennas as a good choice for a broadband array element due to the size, bandwidth and simple construction of the element. However, optimal design of tapered slots is still being studied. An array element is desired to have broad uniform E- and H-plane patterns as well as small dimensions. Janaswamy et al. [11] used a step approximation to the taper of a slot antenna to numerically model the effects of varying length,  $\epsilon_r$  of the substrate and flare angles. In general, it was shown that shorter elements produce narrower E-plane patterns and that height reduction may come with a penalty in beamwidth.

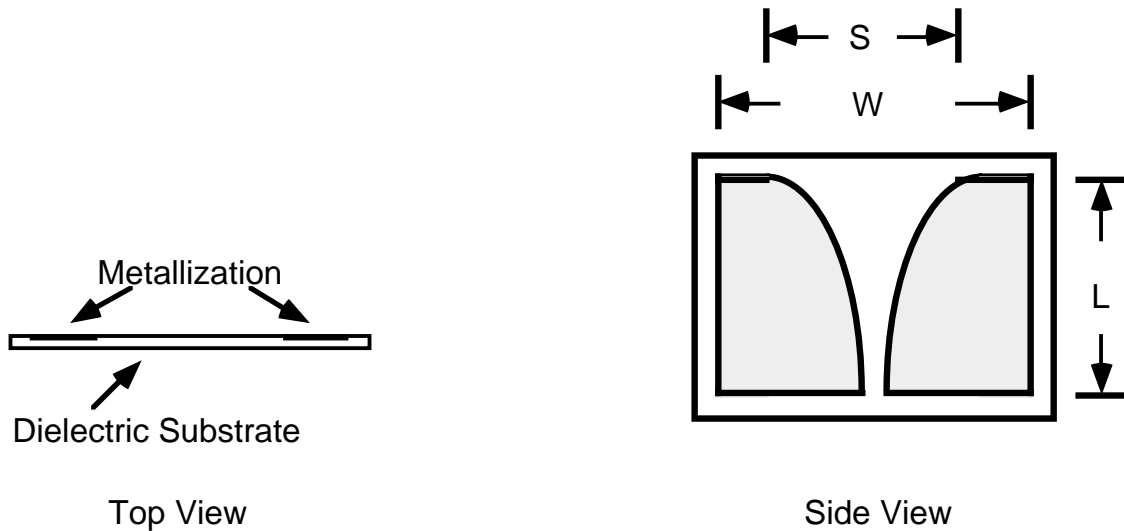
The beamwidth of the Vivaldi antenna is also dependent on the length. Gazit [12] measured the half power beamwidth of four Vivaldi antennas with flare lengths of  $L=150, 110, 80$  and  $60\text{mm}$  lengths in the frequency band of 6-18 GHz see Fig. 2.2. The slots' largest separation is  $S=2\lambda_L$  at 6 GHz and remained constant for the four taper lengths. He found that shorter taper lengths yield larger beamwidths with greater variation between the E- and H-plane patterns. The variation in beamwidth for each geometry in the E-plane is approximately  $20^\circ\text{-}40^\circ$  and the variation in the H-plane is approximately  $20^\circ$  over a 3:1 bandwidth.

Langley et al. [13] designed the Vivaldi antenna with a smooth transition from microstrip to twin line by flaring the metalization on either side of the substrate in opposite directions to form the tapered slot. Their design has high levels of cross-polarization at high frequencies due to the dielectric spacing between the flares of the antenna. The beamwidths for both the E- and H-plane from 6-18 GHz are between  $40^\circ\text{-}60^\circ$  for a flare length  $L=0.6\lambda_L$  and width  $S=0.8\lambda_L$  width with an  $\epsilon_r=2.32$  see Fig. 2.2.

To further reduce the size of the element,  $\epsilon_r$  was increased to 10.5. The increase in the dielectric constant increased the reflections off the dielectric to air boundary. To overcome these reflections, a dielectric dome was placed over the end of the Vivaldi antenna. When this Vivaldi antenna was placed in a 7-element E-plane array a  $40^\circ$  scan could be accomplished with less than 3 dB of gain loss at the center of the 3:1 band. At the upper end of the frequency band a  $40^\circ$  scan could be accomplished with less than 6dB of gain loss.

A single Vivaldi antenna allows only linearly polarized excitations. In many applications dual linear polarization is desired. This can be accomplished by positioning two elements orthogonal to each other to act as a single element. Axness et al. [14] built a dual-polarized Vivaldi antenna by combining four Vivaldi elements in a cross where each element forms an arm of the cross and the orthogonal feeds are not at the same position. This creates a larger element dimension, but allows dual-polarization with the feeds at different positions. The phase center of the four elements, when excited as a single element, is at the center of the cross creating a dual linear Vivaldi antenna.

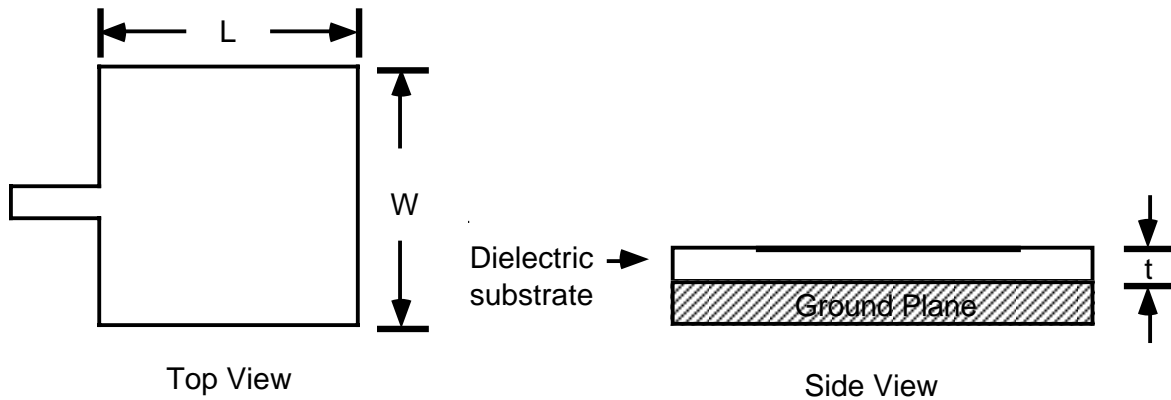
The tapered slot antenna advantage for use in a broadband array is the 3:1 bandwidth and ease of connecting to microstrip transmission lines. The beamwidth typically varies between  $45^\circ$ - $85^\circ$  over the frequency band of operation. At the low frequency of operation the width of the antenna is around  $W=1.2\lambda_L$  and the length is  $L=2\lambda_L$  as seen in Fig 2.2.



**Figure 2.2** Tapered slot geometry

## 2.4 Microstrip Patch Antennas

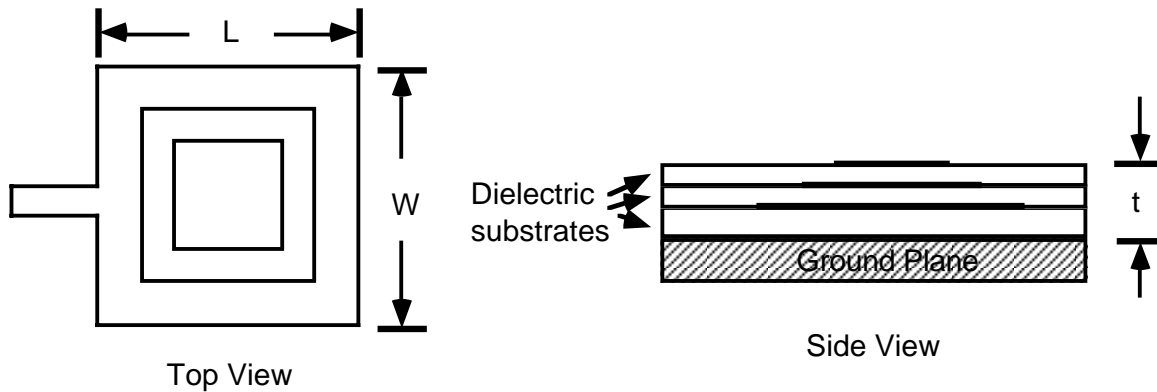
Microstrip patch antennas consist of a radiating part of a microstrip transmission line (MTL). They are easy to construct on printed circuit boards as an extension to the MTL. The simplest design is a half-wavelength rectangular patch microstrip antenna. The microstrip patch antenna can be attached to a single microstrip transmission line at the center of one side to excite a linear polarization. Attaching the microstrip transmission line to one of the orthogonal sides excites the orthogonal polarization. These orthogonal polarizations can be excited simultaneously to create circular polarization. Microstrip patch antennas are not necessarily rectangular. They come in many variations such as circular or rectangular with notches for tuning. However, most microstrip patch antennas have a narrow bandwidth of about 3%, unacceptable in broadband scanning arrays. The simple geometry of a single rectangular patch antenna is shown in Fig. 2.3.



**Figure 2.3** Rectangular patch geometry

Simple microstrip patch antennas are bandwidth limited. However, stacking patches designed for increasing frequency can increase the element bandwidth. The capacitive coupling between the stacked elements allows them to radiate as a single element with a greatly increased bandwidth. The rectangular stacked patch geometry is shown in Fig. 2.4. Rowe et al [15] stacked two square microstrip patch antennas to increase the bandwidth over that of a single patch. There was 11% difference in the center frequencies for each of the patches. In a stacked configuration the element bandwidth increased from 3% to 40%. The largest patch is  $W=L=0.36\lambda_L$  in length and width with a height  $t=0.13\lambda_L$ . However, since the patch radiates from the edges the antenna in an array must have a separation greater than the size of the element. Ghorbani et al. [16] modeled an infinite array of stacked patch elements with a 30% bandwidth. The element spacing of the array was  $0.4\lambda_L$ . Wang et al. [17] in 1997 used stacked-disc radiators to create a wide bandwidth element. The element has continuous coverage over a 45% bandwidth.





**Figure 2.4** Rectangular stacked patch geometry

## 2.5 Low-Profile Broadband Array Elements

For a scanning array to be broadband, the element spacing must be small enough to avoid grating lobes in the pattern over the entire bandwidth of the array for the desired scan angle. Grating lobes will begin to appear at  $90^\circ$  scan angle when the element spacing is greater than  $\lambda/2$  at the frequency of excitation. However, the element spacing of an array is limited by the size of the element. Therefore it is desirable to have small elements in the array. Typically, small elements have limited bandwidth as determined by the input impedance, far-field patterns or polarization purity. To avoid grating lobes, a relatively small broadband element is needed.

Scan angle may also be limited by the beamwidth of the antenna over some or all of the desired frequency range of operation. In addition, a low profile element is desired. There are several viable elements that may be used in broadband arrays. The three elements of interest are the planar equiangular spiral, the Archimedean spiral and the Sinuous antenna. These antennas provide an excellent choice for comparison to the Foursquare element.

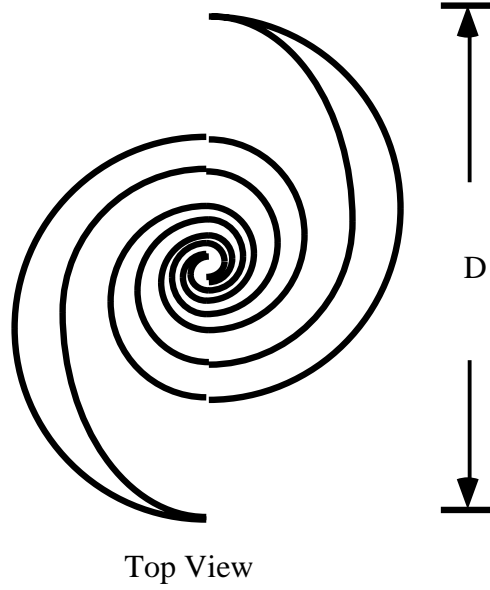
### 2.5.1 Planar Equiangular Spiral Antenna

The planar, equiangular, spiral antenna is a self-complementary antenna consisting of two

arms spiraled about a common center with one arm rotated 180° referenced to the other arm. The radius of the spiral and the width of the arms increase exponentially with rotation angle  $\phi$ . The planar equiangular spiral antenna is created using the equiangular spiral curve generated from the equation [18]

$$r = r_0 e^{a\phi - \delta} \quad (2.1)$$

where  $r_0$  is the radius for  $\phi = 0$ ,  $a$  is a constant controlling the flare rate of the spiral and  $\delta$  defines the rotation of the spiral. The four edges of the planar equiangular spiral antenna are formed using (2.1) for four values of  $\delta$  to form symmetric arms of the antenna as seen in Fig. 2.5. The equiangular spiral can be easily constructed on a substrate and has a low profile. The diameter is approximately given by  $D = \lambda_L/2$ , where  $\lambda_L$  is wavelength at the lower frequency of operation. The element produces a half-power beamwidth of 90° [18]. The polarization of the equiangular spiral is circular and will maintain this polarization up to 70° off axis [18]. Most importantly, the planar equiangular spiral typically supports a bandwidth of 8:1 [18].



**Figure 2.5** Equiangular spiral geometry

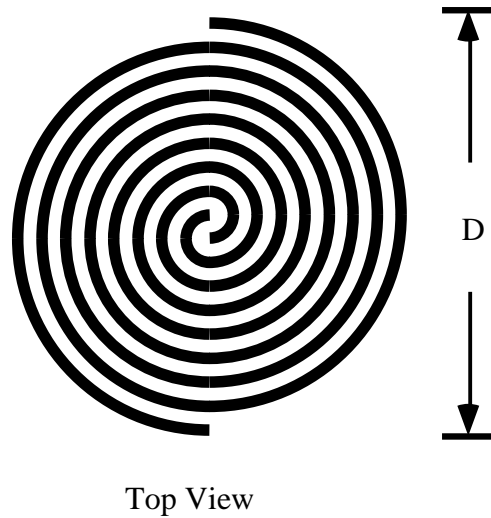
### 2.5.2 Archimedean Spiral Antenna

The Archimedean spiral antenna is also a self-complimentary antenna consisting of two arms spiraled about a center rotated  $180^\circ$  relative to each other. However, the Archimedean spiral varies its radius,  $r_0$ , linearly with respect to the angle of rotation,  $\phi$ , and maintains a constant arm width. The equation of the Archimedean spiral is given by [18]

$$r = r_0\phi \quad \text{and} \quad r = r_0(\phi - \pi) \quad (2.2)$$

which creates the two arms of the Archimedean spiral. The arms of the antenna create a circularly polarized antenna. The lower frequency of operation of the antenna is limited by the diameter. The diameter is approximately given by  $D = \lambda_L/2$ , where  $\lambda_L$  is the wavelength at the lower frequency of operation. The dimensions of the Archimedean spiral are shown in Fig. 2.6. The Archimedean spiral antenna can be cavity backed which introduces a fixed physical length to the geometry of the antenna. This fixed length

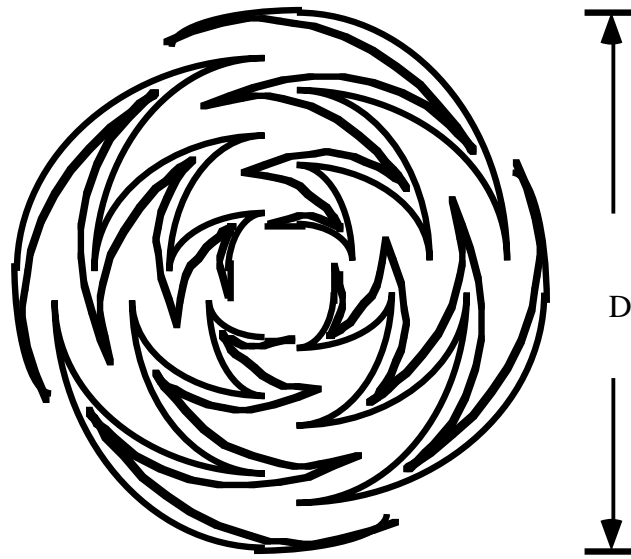
affects the frequency independent nature of the antenna. The Archimedean spiral has a HP beamwidth of about  $74^\circ$  and typically supports a bandwidth of 10:1 [18].



**Figure 2.6** Archimedean spiral antenna geometry

### 2.5.3 Sinuous Antenna

The Sinuous antenna has four arms rotated at  $90^\circ$  relative to each other. The four arms circularly oscillate  $\pm 45^\circ$  with increasing distance from the center. The Sinuous antenna is related to the spiral antenna but has the added advantage of two feed points. The two feed points can produce orthogonal linear polarization. This allows polarization diversity for transmit and receive operation or LHCP or RHCP. The circumference of the antenna is approximately 1 wavelength at the lower frequency of operation. The diameter of the Sinuous antenna is  $D=0.4\lambda_L$  as seen in the geometry of Fig. 2.7 [22]. The Sinuous antenna typically supports a bandwidth of 5:1 [22].



Top View

**Figure 2.7** Sinuous geometry

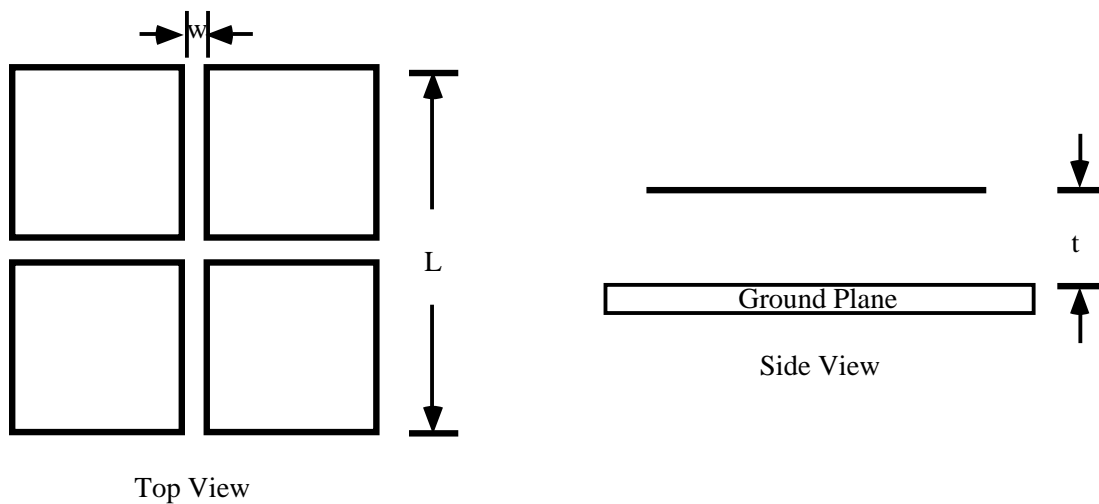
#### 2.5.4 Foursquare Antenna

The Foursquare antenna is a low profile broadband antenna developed at Virginia Tech. The Foursquare in its simplest form, shown in Fig. 2.8, consists of four metallic squares placed in a 2-by-2 grid structure and placed approximately  $\lambda/4$  above a ground plane at the center frequency of operation [20]. There are two feed points at the inner corners of diagonally opposed metallic squares. The metallic squares flare from the feed points similar to a bow-tie antenna. Flaring effectively gives the bow-tie antenna a larger diameter than a dipole of equivalent length and increases its bandwidth. Similarly, the diagonally opposed metallic squares of the Foursquare are excited like a bow-tie antenna, where the width of the squares increases the bandwidth over that of a dipole of the same length. This alone does not account for the broadband characteristics of the Foursquare antenna.

The Foursquare also consists of two parasitic metallic squares that contribute to the broadband characteristics of the Foursquare. The parasitic squares of the Foursquare are similar to the sleeve of a sleeve dipole. At the low frequency band of operation of a sleeve dipole the dominant radiating currents are on the dipole. However, when the

frequency of operation is increased the dominant radiating currents are on the sleeve. This creates two distinct frequency bands of operation for a sleeve dipole. Similarly, the Foursquare at low frequencies of operation radiates predominantly from the metallic squares attached to the feed points. However, when the frequency of operation is increased the dominant radiating currents are on the parasitic elements. Rather than having two distinct frequency bands, such as the sleeve dipole, the Foursquare has a single broad frequency band of operation.

The diameter of the Foursquare antenna at the lower frequency of operation is  $L=0.35\lambda_L$  and  $t=0.11\lambda_L$  [20]. Like the sinuous antenna, the Foursquare can be operated in dual orthogonal linear polarization. Of course, the two linear polarization signals can be combined to produce RHCP and LHCP responses. The antenna pattern is a broad pattern and is uniform in both the E- and H-plane over the operating frequencies. These characteristics make the Foursquare a desirable choice for a wide bandwidth array element.



**Figure 2.8** Foursquare antenna geometry

## 2.6 Summary

There have been many variations of scanning arrays since the first open-ended waveguide arrays. The shortage of space on military vehicles encouraged the design of multifunctional arrays. Multifunctional arrays typically consist of multiple array elements interlaced in a single aperture. The structurally-integrated optically re-configurable antenna array uses optical switches to reconfigure the radiating element for each frequency band. Unlike the multifunctional arrays, the re-configurable array can not simultaneously operate in multiple frequency bands. Other research has concentrated on the design of small broadband elements such as the previously mentioned stacked-disc radiators and tapered slot antennas. The sinuous, Foursquare, Archimedean spiral and equiangular spiral are also broadband elements. Table 2.1 summarizes the characteristics of elements discussed in this chapter for comparison. The sinuous and Foursquare antennas both allow polarization diversity along with a relatively small size and low profile. The Archimedean spiral and equiangular spiral allow only circular polarization but are small in size and have a low-profile. These four antennas will be compared in detail in Chapter 3.

Each previously described element could be the best element for a given situation. Some applications require high power at the expense of bandwidth. Other applications may require lightweight elements or polarization diversity. Low profile and simplicity of the feed network are also important, considerations. The emphasis in this dissertation is to demonstrate the capabilities of the Foursquare array.

## Chapter 3

### **ARRAY BANDWIDTH<sup>1</sup>**

Phased array antennas are finding more applications in commercial and military systems for both communications and sensing. Increased use is made possible through advances in manufacturing techniques, lowering microwave material costs, and wider availability of hardware for beamforming. Phased arrays offer many advantages over mechanically scanned aperture antennas or fixed-phase arrays. The most significant feature of a phased array is that the signal of interest from a mobile platform can be tracked with no antenna movement. In fact, multiple signals of interest can be tracked simultaneously. In addition, adaptive algorithms can be employed for interference rejection while tracking the desired signal.

Bandwidth requirements on phased arrays are increasing because of new applications demanding wider operating bandwidths. Wideband phased arrays have many applications, with multifunctional systems being one of the most popular uses. An example of a multifunctional system is a single phased array supporting multiple communication and radar bands. Bandwidths of such systems can be 5:1 or more. This places extreme demands on all three aspects of phased array design: the element, the array architecture, and the feed network. Although several wideband elements are available, the element must be appropriate for the array architecture, which is determined by requirements on the bandwidth, scan range, and the pattern. Also, a feed network

---

<sup>1</sup> *This chapter is largely taken from a paper submitted to the Microwave Journal by Dr. Warren L. Stutzman and Carey Buxton titled “Radiating Elements for Wideband Phased Arrays.”*



must be designed for the chosen elements and array architecture in order to meet system performance specifications. These array design aspects are highly interrelated.

The design process often proceeds in the following manner. The array architecture is investigated first because the array grid has the strongest influence on performance. The fixed physical inter-element spacing for an array grid increases with frequency and leads to wide performance variations with frequency. Next, element specifications are developed from the selected array grid and the system requirements. Finally, a feed network is designed for the element and array architecture selected. In many cases this process is repeated several times with different combinations of array configurations and element types.

For wideband arrays the limiting factor is almost always the physical size of the element. That is, for wideband operation, array performance degrades in the upper end of the operating frequency band where the fixed physical separation of the elements in the array grid becomes large in terms of a wavelength. Another severe constraint on element size arises from the fact that the maximum inter-element spacing becomes smaller with wider scan angle requirements. Thus, system requirements are met by using close inter-element spacings. This, in turn, places an upper limit on the size of the elements. This chapter examines the relationship between array grid and element size. The most direct way to evaluate element suitability for use in an array is to determine its acceptable element electrical size based on its performance in the array. This information together with the scan requirements determines array bandwidth. A graphical method is presented that displays this relationship and serves as a guide in the selection of the element.

### **3.1 Wideband Array and Element Principles**

A wideband array has acceptable performance over a frequency range extending from a lower frequency  $f_L$  to an upper frequency  $f_U$ . Acceptable performance is determined by meeting pattern, gain, impedance, and polarization requirements over the bandwidth and scan range. Performance requirements can vary with frequency. For example, in multifunctional array applications requirements differ over sub bands within the total

bandwidth. The subsequent discussion assumes continuous frequency coverage, but is readily applied to multi-band, multifunctional situations.

Bandwidth is expressed in two ways, as a ratio and as a percentage [18]. Bandwidth as a ratio is usually used for very wide bandwidth applications and is defined as

$$B_r = \frac{f_U}{f_L} \quad (3.1)$$

and often denoted as  $B_r:1$ . Bandwidth for moderately wideband antennas is usually expressed as a percentage relative to the center frequency  $f_c$ :

$$B_p = \frac{f_U - f_L}{f_c} \times 100 \quad (3.2)$$

Both of these definitions are in common use and are related to each other by

$$B_p = 2 \frac{B_r - 1}{B_r + 1} \times 100 \quad (3.3)$$

For example, an octave bandwidth ( $B_r=2$ ) corresponds to a percentage bandwidth of 67%. Table 3.1 provides a complete list that is helpful in comparing bandwidths expressed using either definition.

**Table 3.1** Comparison of Bandwidth Definitions

<i>Element Bandwidth</i>	
$B_r$	$B_p$
1.29	25%
1.67	50%
2 (1 octave)	67%
3	100%
4 (2 octaves)	120%
8 (3 octaves)	156%
10 (decade)	164%

The phased array design problem is to meet performance requirements over the specified bandwidth and scan range of the array. Maximum scan angle can be limited by several performance factors of an array, such as the appearance of grating lobes, scan loss due to element pattern effects, and null formation due to blind spots. The appearance of grating lobes determines the upper limit on the maximum scan angle of an array with broad element patterns. Null formation, due to mutual coupling between elements, can limit the maximum scan angle more than grating lobe appearance. In this treatment we will use grating lobe appearance as the criterion for the scan limit. However, other criteria can be substituted as appropriate. Emphasis is on the process of element selection.

The element spacing  $d$ , normalized to wavelength  $\lambda$ , that can be achieved without the appearance of the grating lobe peak for a maximum scan angle,  $\theta_{\max}$ , is given by

$$\frac{d}{\lambda} \leq \frac{1}{1 + \sin \theta_{\max}} \quad (3.4)$$

For example, to achieve a maximum scan angle of  $\theta_{\max}=90^\circ$  the spacing between the elements must be less than  $\lambda/2$  over the entire frequency band of operation. Usually scan angles as large as  $90^\circ$  are not possible because performance will be limited by other factors such as element pattern scan loss. A reduction in the maximum scan angle to less than  $90^\circ$  permits element spacing to be greater than  $\lambda/2$ . The maximum value of physical element spacing is found from (3.4) at the lowest operating wavelength (highest operating frequency):

$$d \leq \frac{\lambda_U}{1 + \sin \theta_{\max}} \quad (3.5)$$

On the other hand, wideband element performance is almost always limited by the element physical size. That is, the element must be electrically large (and thus physically large), in order to radiate efficiently at the lowest operating frequency. Thus, the lowest operating frequency of a wideband array  $f_L$  is determined by element size, which is usually determined by element impedance or gain performance.

The lowest operating frequency is fixed by the physical extent of the element in the plane of the array grid,  $D$ :

$$D = a\lambda_L \quad (3.6)$$

where  $a$  is a dimensionless constant that is the fractional wavelength size of the element at the lowest operating frequency; that is,  $a = D/\lambda_L$ . Here we are assuming that the elements have the same extent  $D$  in both directions in the array plane, permitting full two-dimensional scan. Choosing the element size  $D$  to be as large as possible without overlapping elements gives  $D=d$  and using the largest spacing governed by scan limits in (3.5) leads to

$$D = d = \frac{\lambda_U}{1 + \sin \theta_{\max}} \quad (3.7)$$

The discussion here assumes a uniform array grid, but wider bandwidth arrays can be designed having elements of different sizes and less dense array grid geometries. [19]

Thus, array bandwidth is determined by the element size at the low end of the operating frequency range and by scan performance at the upper end. Array bandwidth as a ratio is found by substituting the results of (3.6) and (3.7) into (3.1) to obtain

$$B_r = \frac{f_U}{f_L} = \frac{\lambda_L}{\lambda_U} = \frac{D/a}{D(1 + \sin \theta_{\max})} = \frac{1}{a(1 + \sin \theta_{\max})} \quad (3.8)$$

For example, an array with elements of diameter  $D=0.4\lambda_L$  (i.e.,  $a=0.4$ ) and a scan limit of  $90^\circ$  has a bandwidth of  $B_r=[0.4(1+1)]^{-1}=1.25$ , which from (3.3) corresponds to  $B_p=22\%$ .

If the scan limit is reduced to  $45^\circ$ , then  $B_r=1.46$ , or  $B_p=38\%$ .

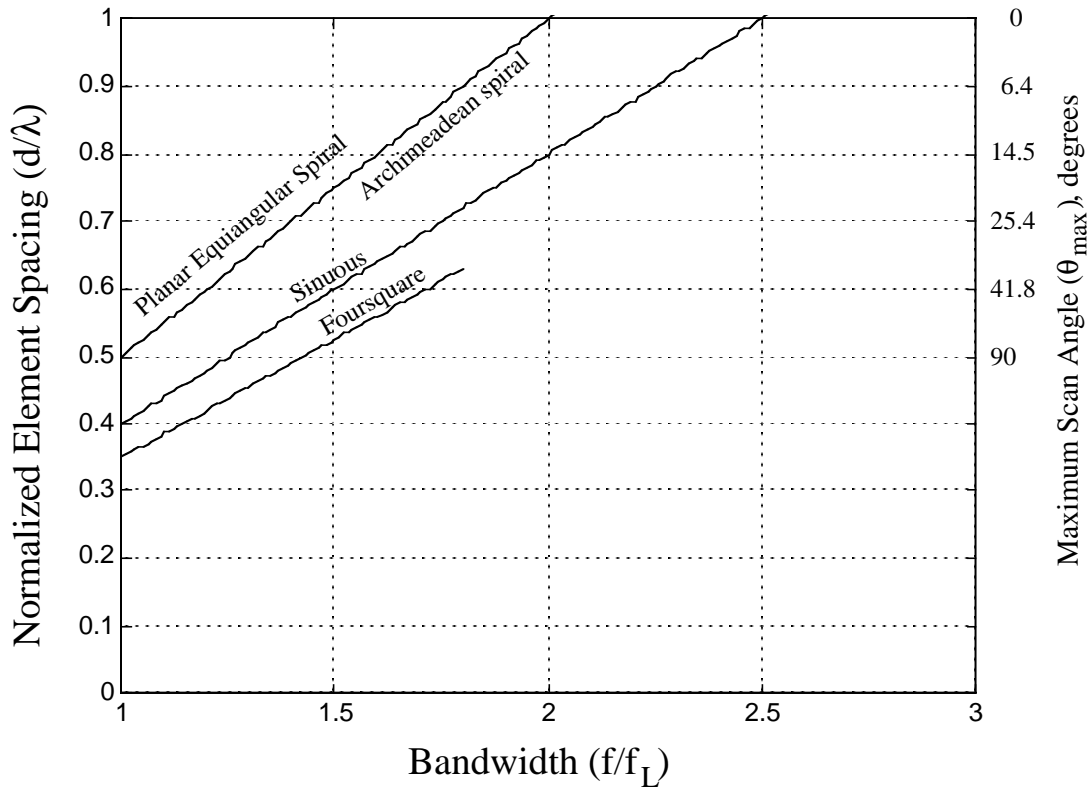
Element performance can be plotted versus normalized frequency to produce a plot that reveals bandwidth for various scan angles. This array design plot is shown in Fig. 3.1 for several radiating element types (which are discussed in the next section). Each line in the plot is generated from its slope and the point of intersection with the ordinate. The dependent variable, element spacing normalized to wavelength ( $d/\lambda$ ), can be expressed in terms of the independent variable  $f/f_L$  as

$$\frac{d}{\lambda} = \frac{d}{\lambda_L} \left( \frac{f}{f_L} \right) \quad (3.9)$$

This is the equation for a line passing through the origin with a slope of  $d/\lambda_L$ . The intersection point of the element line with the ordinate (located at  $f=f_L$ ) is  $d/\lambda=d/\lambda_L$ .

Using the maximum element size ( $D=d$ ), the ordinate intersection point is  $d/\lambda_L=D/\lambda_L=a$ ,

where (3.6) was used. The right end point of the element line corresponds to the upper operating frequency of the element,  $f_U/f_L$ . Also shown in Fig. 3.1, on the right hand vertical axis, is the maximum scan angle,  $\theta_{\max}$ , which is found from (3.4). Points on the right ordinate correspond to the element spacing,  $d/\lambda$ .



**Figure 3.1** Minimum element spacing ( $d=D$ ) normalized to wavelength as a function of normalized frequency for various element types. The right ordinate shows maximum scan angle.

The primary use of Fig. 3.1 is to compare the performance of elements over the specified array bandwidth and scan range. The upper operating frequency  $f_U$  is determined from the intersection of a horizontal line from the maximum scan angle on the right ordinate and the element line. A vertical line from this point crosses the abscissa at the point corresponding to  $(f_U/f_L)$ , giving the array bandwidth for that element

for the desired value of  $\theta_{\max}$ . For example, an array of Archimedean spirals with a maximum scan angle of  $\theta_{\max}=25^\circ$  has a bandwidth of  $B_r=1.4$ .

Figure 3.1 can also be used to determine the maximum element size that is suitable for a given scan range and bandwidth. A vertical line drawn through the abscissa value for bandwidth ( $f_U/f_L$ ) intersects the lines corresponding to various elements. Horizontal lines drawn from these points of intersection through the  $\theta_{\max}$  ordinate correspond to the maximum scan angles achievable over the desired bandwidth ( $f_U/f_L$ ) for each element type. The lower the element line in Fig. 3.1, the smaller the electrical size of the element and the larger is the obtainable array bandwidth.

Though broadband characteristics of the element in an array are desirable, the element with the largest bandwidth may not yield the widest array bandwidth for wide scan requirements. Figure 3.1 shows that the Archimedean spiral, planar equiangular spiral and sinuous elements all have much larger bandwidths than the Foursquare element. However, array bandwidths for the Archimedean spiral, planar equiangular spiral and Sinuous elements with a maximum array scan angle of  $45^\circ$  are 1.2:1, 1.2:1 and 1.5:1 respectively. The Foursquare element permits array bandwidths of 1.7:1. Therefore, Fig. 3.1 demonstrates the important fact that element size is as important as element bandwidth when choosing an antenna for use in broadband scanning arrays.

### **3.2 Low-Profile Wideband Radiating Elements**

The previous section presented the process for evaluating elements for use in wideband phased arrays. This section discusses several candidate elements along with their characteristics. The performance values for elements listed in Table 3.2 were determined from experiments performed by the Virginia Tech Antenna Group and from the literature [18]. All the elements listed in Table 3.2 are low profile. In order to produce the unidirectional beam needed for planar arrays, these elements are backed by a ground plane. Element bandwidth and element diameters are especially sensitive to feed, balun,

and ground plane details. The values listed in Table 3.2 are based on acceptable impedance and gain; and will vary with application.




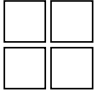
The Archimedean and equiangular spirals are circularly polarized elements capable of very wide bandwidth. The sinuous antenna is dual linearly polarized and is also capable of wide bandwidth. The Foursquare is a new element that offers several performance features highly desirable for phased arrays [20]. It has very small lateral extent and shallow depth, making it low profile. The Foursquare has nearly equal E- and H-plane beamwidths that remain constant over its bandwidth.

There are several factors in the choice of element type. The depth of the element is a major consideration. Depth is the dimensional extent perpendicular to the surface of the array grid. An element with small depth is referred to as a low profile element. Many applications require low profile elements so that the array can be placed on the skin of a vehicle. This requirement eliminates several very wideband element types, such as the tapered slot antenna, from consideration as a candidate.

The Archimedean spiral, planar equiangular spiral, Sinuous, and Foursquare elements were chosen to be evaluated for broad bandwidth scanning arrays based on their small size, low profile, uniform E- and H-plane patterns, and broad bandwidth. The Archimedean spiral, planar Equiangular spiral and Sinuous achieve bandwidths greater than 8:1 [18,22] and the Foursquare's bandwidth is 1.8:1. These bandwidth values are listed in Table 3.2.



**Table 3.2** Wideband radiating element characteristics

Element Type	Element Bandwidth (Br)	Beamwidth (HP), degrees	Enclosing Diameter (D)	Array Bandwidth (45° scan)	Polarization
Archimedean spiral 	~10:1	75	$0.5 \lambda_L$	1.2:1	Circular
Equiangular spiral 	~8:1	70	$0.5 \lambda_L$	1.2:1	Circular
Sinuuous 	~9:1	60-110	$0.4 \lambda_L$	1.5:1	Dual linear
Foursquare 	1.8:1	60-70	$0.35 \lambda_L$	1.7:1	Dual linear

As presented in the previous section, array bandwidth is likely to be limited by element size rather than element bandwidth. A very wideband element is often physically large and the full bandwidth of the element cannot be utilized in the array because of scan angle limitations. For example, from Table 3.2 we see that the bandwidth of the Foursquare is less than that of the sinuous, but this does not eliminate the Foursquare from consideration as an array element. For a maximum scan angle of 40° the array bandwidth achieved with Foursquare elements is 1.7 whereas it is only 1.5 with sinuous elements. The dimension of the antenna at the lower frequency of operation,  $f_L$ , determines the minimum spacing between the elements in an array; see (3.6). Close spacing between elements is required to ensure that the maximum scan angle is not limited by spacing at the upper end of the frequency band; see (3.5). Viewed slightly

differently; selecting an element with large electrical size in order to leave wide element bandwidth will limit the achievable maximum scan angle.

Thus, small electrical size is a very important feature in the selection of phased array elements. Of the four elements considered, the Sinuous and the Foursquare have the smallest diameter,  $D$ ; see Table 3.2. The Archimedean spiral has a diameter of  $D=\lambda_c/2$  [1]. The Foursquare has a diameter of  $D=0.35\lambda_c$  [20]. The planar equiangular spiral has a diameter of  $D=\lambda_c/2$  [18] and the sinuous has a diameter of  $D=0.4\lambda_c$  [22].

Element size and bandwidth are very important considerations, but the polarization requirements of an array must also be considered. The array may require linear polarization, or circular polarization, or both. The Archimedean spiral and planar equiangular spiral produce circular polarization [18]. In many communications applications polarization diversity or reuse require dual-polarized elements. The Sinuous and the Foursquare provide dual linear polarization [21,22].

To achieve large scan angles in all planes, broad beamwidths are required in both the E- and H-plane. A narrow beamwidth element reduces the maximum scan angle achieved by an array due to loss of gain at large scan angles. In wideband arrays, the broad element patterns should be constant over the entire frequency band of operation. Element beamwidths are listed in Table 3.2. The planar equiangular spiral has a half-power beamwidth of 70 degrees, which is similar to the Archimedean spiral beamwidth of 75 degrees, [18]. The Foursquare has a 60 to 70 degree beamwidth, [20]. The sinuous has a beamwidth that varies from 110 to 60 degrees between 2 to 18 GHz, [22]. IV.

### **3.3 Summary**

In the process of designing a broadband scanning array antenna many criteria must be balanced in order to find the optimum antenna element for the application. The bandwidth of the element must be large enough to meet the required array bandwidth. The beamwidth of the element in both the E- and H-plane should be broad so that the maximum scan angle of the array is not limited by gain loss. Dual polarization may be

required, depending on the application. For some communication and sensing applications lack of polarization diversity alone may eliminate a candidate element. Element size is perhaps the most important parameter when selecting an element for a broadband phased array. Element selection for specific array scans and bandwidth requirements is facilitated by the process illustrated in Fig. 3.1.

## FINITE DIFFERENCE TIME DOMAIN METHOD

The finite difference time domain (FDTD) method was chosen because of its ability to easily model finite dielectric objects. Other numerical methods such as the method of moments can easily model infinite dielectric slabs. However, the formulation is not trivial for a finite dielectric slab. Unlike FDTD, the method of moments is inherently well suited for objects radiating in free space because the free space Green's function is defined for an infinite space. In comparison, FDTD is inherently well suited for finite regions. Since antennas are typically radiating in free space, the FDTD grid is terminated in an absorbing boundary to effectively simulate a free space environment. Because of the introduction of the perfectly matched layer (PML) and Uniaxial PML (UPML) absorbing boundary conditions, it is possible to model an antenna radiating in free space using the FDTD method.

The FDTD method is a time domain method used to numerically model electromagnetic problems. This method divides a finite space into cells. In three dimensions this is called a Yee cell. Each edge of the cell is defined by a field value that exists at the center of the edge and is pointing parallel to the edge. The Yee algorithm has two interlocking grids that are offset by half a cell in the  $x$ -,  $y$ -, and  $z$ -directions and a half time step. One grid consists of electric field values and the other grid consists of magnetic field values. The field values are updated every time step,  $\Delta t$ , to yield the time domain response of the electromagnetic problem being modeled.

The FDTD method was proposed for electromagnetic problems by Yee [23] in 1966. Until the development of absorbing boundary conditions (ABCs), FDTD was limited to the modeling of finite space problems. The ABCs permit modeling of infinite problems such as an antenna radiating in free space. ABCs such as Mur, Higdon and perfectly matched layer (PML) are all methods of absorbing the fields radiating from the source as they propagate towards the boundary [24]. The advantage of the FDTD method advantage over other numerical methods is that it can easily model dielectric and

magnetic materials of finite extent. This is of particular interest when modeling the effects of dielectric substrates or magnetic loading of antennas. The FDTD method has the added advantage of being able to provide the frequency response of an antenna with the output response from a single run by calculating the discrete Fourier transform of the time domain output signal.

An FDTD code was developed to analyze the Foursquare element and Foursquare arrays because of its versatility in modeling dielectric materials. The primary subroutine of the FDTD code is the UPML ABCs update equations. These equations are the update equations for the ABCs and the update equations for the entire grid space. To calculate the far-field patterns of the antenna one subroutine performs a near-to-far-field transformation using frequency domain equivalent currents on a closed surface surrounding the antenna. The frequency domain equivalent currents are found from the discrete Fourier transform of the time domain equivalent currents. The modeling of the antenna feed and the input impedance are also described in this chapter.

#### **4.1 Absorbing Boundary Conditions (ABCs) and Update Equations**

The ABCs are the most significant subroutine of any FDTD code for modeling antennas radiating in free space. Without good ABCs the model cannot accurately predict the far-field pattern, input impedance or surface currents. The FDTD code that was developed for this study uses Uniaxial PML (UPML) boundary conditions to model a free space environment. The UPML boundary conditions were first introduced for the FDTD method by Gedney [25]. The UPML ABCs are an improvement over the original PML developed by Berenger [26] in 1994 because the formulation allows the material parameters of the PML to be stored as three vectors rather than a three-dimensional matrix of parameters.

Uniaxial PML ABCs attempt to match the impedance of the PML boundary with that of the interior grid space. By matching the impedance, the reflections off the boundary do not exist, therefore modeling a free space environment. In a discrete space, as modeled by the FDTD code, the reflection is minimized if the loss in the UPML is

tapered appropriately through a sufficient number of boundary cells. With the introduction of loss into the UPML boundary the wave is attenuated as it travels through the UPML. The UPML update equations are also the update equations for the interior space when the losses are set to zero. One of the six sets of UPML update equations from [27] is given as

$$D_x \Big|_{i+\frac{1}{2},j,k}^{n+\frac{1}{2}} = \left( \frac{K_y - \frac{\sigma_y}{2\epsilon_0}}{\Delta t} \right) D_x \Big|_{i+\frac{1}{2},j,k}^{n-\frac{1}{2}} + \left( \frac{1}{\frac{K_y + \frac{\sigma_y}{2\epsilon_0}}{\Delta t}} \right) \times \quad (4.1 \text{ a})$$

$$\left( \frac{H_z \Big|_{i+\frac{1}{2},j+\frac{1}{2},k}^n - H_z \Big|_{i+\frac{1}{2},j-\frac{1}{2},k}^n}{\Delta y} - \frac{H_y \Big|_{i+\frac{1}{2},j,k+\frac{1}{2}}^n - H_y \Big|_{i+\frac{1}{2},j,k-\frac{1}{2}}^n}{\Delta z} \right)$$

$$E_x \Big|_{i+\frac{1}{2},j,k}^{n+\frac{1}{2}} = \left( \frac{K_z - \frac{\sigma_z \Delta t}{2\epsilon_0}}{K_z + \frac{\sigma_z \Delta t}{2\epsilon_0}} \right) E_x \Big|_{i+\frac{1}{2},j,k}^{n-\frac{1}{2}} + \left[ \frac{1}{\left( K_z + \frac{\sigma_z \Delta t}{2\epsilon_0} \right) \epsilon_0 \epsilon_r} \right] \times \quad (4.1 \text{ b})$$

$$\left[ \left( K_x + \frac{\sigma_x \Delta t}{2\epsilon_0} \right) D_x \Big|_{i+\frac{1}{2},j,k}^{n+\frac{1}{2}} - \left( K_x + \frac{\sigma_x \Delta t}{2\epsilon_0} \right) D_x \Big|_{i+\frac{1}{2},j,k}^{n-\frac{1}{2}} \right]$$

where  $(i,j,k)$  is the spatial position of the fields and  $n$  is the time step. The spacing between the fields in the  $x$ ,  $y$  and  $z$  directions are given by  $\Delta x$ ,  $\Delta y$  and  $\Delta z$ . The spacing in time is given by  $\Delta t$ . The appropriate spatial scaling of the material parameters can be found from

$$\sigma(x) = \left( \frac{x}{d} \right)^m \sigma_{\max} \quad (4.2)$$

and

$$K(x) = 1 + (K_{\max} - 1) \left( \frac{x}{d} \right)^m \quad (4.3)$$

where

$$\sigma_{\max} = \frac{m+1}{150\pi\sqrt{\epsilon_r}\Delta x} \quad \text{and} \quad K_{\max} = 4.5 \quad (4.4)$$

The distance into the absorbing boundary is  $d$ . Parameter  $m$  is typically chosen between 3 and 4. The stability of the UPML update equations is given by the Courant limit as

$$\Delta t \leq \frac{1}{c\sqrt{\frac{1}{\Delta x^2} + \frac{1}{\Delta y^2} + \frac{1}{\Delta z^2}}} \quad (4.5)$$

The UPML material parameters,  $\sigma_i$  and  $K_i$ , are defined as vectors that represent the variation in the material parameters in the corresponding  $x$ ,  $y$  and  $z$  directions. Because the material parameters of the UPML are separable in the  $x$ ,  $y$ , and  $z$ -directions they can be described with three vectors. The vector representation of the material parameters requires less storage space than the PML method, which requires the material parameters to be specified for every grid position in the PML boundary.

Typically a UPML boundary of 10 cells deep is adequate. It is also recommended to leave a spacing of 5 cells between the antenna edge and the UPML boundaries. If the UPML boundary conditions are formed correctly, the reflections from the boundary surface will be minimized. The minimal reflections allow accurate calculation of the far-field and input impedance.

## 4.2 Far-field Pattern Calculations

The update equations are the primary subroutine of any FDTD code. However many more subroutines are required too effectively model an antenna. Calculating the far-field pattern from the field values given by the update equations requires several subroutines. The far-field pattern can be determined from the frequency domain equivalent currents on a closed surface surrounding the antenna. The equivalent currents are found from the closed boundary, frequency domain field values. Since FDTD is a time domain method,

the field values calculated by the update equations are in the time domain. A DFT is performed to convert the time domain field values to the frequency domain. This process of calculating the far-field pattern will be described.

First the equivalent frequency domain currents,  $J_s$  and  $M_s$ , on a closed surface surrounding the antenna are given by

$$\bar{J}_s = \hat{n} \times (\bar{H}_1 - \bar{H}) \Big|_{\bar{H}=0} \quad (4.6 \text{ a})$$

$$\bar{M}_s = -\hat{n} \times (\bar{E}_1 - \bar{E}) \Big|_{\bar{E}=0} \quad (4.6 \text{ b})$$

Where  $n$  is the unit normal to the surface surrounding the antenna and  $(\bar{E}, \bar{H})$  are the fields inside the surface and  $(\bar{E}_1, \bar{H}_1)$  are the fields outside the surface. Since FDTD is a time domain method the field values are converted to the frequency domain for specified frequencies. The frequency domain currents are found from the discrete fourier transform (DFT) formulated as

$$E_{i,j,k}^r = E_{i,j,k}^r + E_{i,j,k}^n * \cos(\omega n \Delta t) \quad (4.7 \text{ a})$$

$$E_{i,j,k}^i = E_{i,j,k}^i + E_{i,j,k}^n * \sin(\omega n \Delta t) \quad (4.7 \text{ b})$$

$$E_{i,j,k} = E_{i,j,k}^r - E_{i,j,k}^i \quad (4.7 \text{ c})$$

Where  $E_{i,j,k}^r$  is the real part of the frequency domain electric field values and  $E_{i,j,k}^i$  is the imaginary part of the frequency domain electric field values at position  $(i,j,k)$ . The same formulation is applied to the magnetic field values.

Next, the near-to-far-field transformation using the frequency domain equivalent currents will be used to determine the far-field pattern of the antenna. The near-to-far-field transformation is described in [24] and is given by



$$\bar{N} = \iint_s (\hat{x}\bar{J}_x + \hat{y}\bar{J}_y + \hat{z}\bar{J}_z) e^{+jkr' \cos \Psi} ds' \quad (4.8 \text{ a})$$

$$\bar{L} = \iint_s (\hat{x}\bar{M}_x + \hat{y}\bar{M}_y + \hat{z}\bar{M}_z) e^{+jkr' \cos \Psi} ds' \quad (4.8 \text{ b})$$

where

$$\bar{N} = \bar{N}_\theta + \bar{N}_\phi \quad (4.9 \text{ a})$$

$$\bar{L} = \bar{L}_\theta + \bar{L}_\phi \quad (4.9 \text{ b})$$

$\bar{N}_\theta, \bar{N}_\phi, \bar{L}_\theta$  and  $\bar{L}_\phi$  can be found by performing the coordinate transformation from cartesian to spherical coordinates. These values in spherical coordinates are used to calculate  $E_\theta$  and  $E_\phi$  given by

$$E_\theta = \frac{-je^{-jkr}}{2\lambda_0 r} (L_\phi + \eta_0 N_\theta) \quad (4.10 \text{ a})$$

$$E_\phi = \frac{je^{-jkr}}{2\lambda_0 r} (L_\theta - \eta_0 N_\phi) \quad (4.10 \text{ b})$$

$E_\theta$  and  $E_\phi$  can be found in both the E- and the H-plane. If the antenna is mounted over an infinite ground plane the equivalent currents are found from a closed surface surrounding the antenna. The near-to-far-field transformation is then performed using these equivalent currents and the currents imaged through the ground plane.

### 4.3 Antenna Specifications

Far-field patterns along with the UPML ABC's and update equations are the dominant subroutines of the FDTD code. However, supporting subroutines that specify the antenna design parameters are required for modeling antennas. The antenna structure is modeled by PEC boundaries at positions in the FDTD grid that correspond to the antenna surface. The time domain excitation is calculated for the desired frequency response. Also, the source position relative to the FDTD grid is specified.

The PEC surfaces of an antenna can be easily specified in an FDTD code by simply enforcing Dirchlet Boundary conditions. The Dirchlet Boundary conditions for the PEC boundaries simply state that the tangential electric fields on the surface are zero. Therefore, at every FDTD grid point corresponding to the surface of the antenna the tangential electric fields are forced to zero.

The time domain excitation can be defined several ways. Some common excitations are gaussian pulse, a sinusoid and a differentiated gaussian pulse. The time domain source should be chosen to excite the frequency range of interest, since, the grid size is based on the maximum frequency of excitation so that  $\Delta x$ ,  $\Delta y$  and  $\Delta z$  are less than  $\lambda/20$ . If this limit is greatly exceeded, instabilities may occur. The gaussian pulse is chosen to limit undesired high frequency components that greatly exceed the  $\lambda/20$  limit. By formulating the source as a differentiated gaussian source the DC component of the gaussian pulse can be eliminated. The differentiated gaussian source is used in this FDTD code.

Once the time domain signal is specified it is injected into the FDTD model via a source. There are two types of sources that can be simulated in the FDTD method. The easiest to implement is the hard source given as

$$E_z|_{i,j,k}^n = f(t) \tag{4.11}$$

Where  $f(t)$  is the differentiated gaussian pulse. This model is called a hard source because any fields reflected back towards the source will scatter as if it is a PEC boundary.

The second type of source called the soft source eliminates scattering from the source by formulating the source as the sum of the updated fields at that position plus the differentiated gaussian source excitation. The soft source formulation is given by

$$E_z|_{i,j,k}^n = E_z|_{i,j,k}^n + f(t) \quad (4.12)$$

With a soft source any fields reflected back towards the source pass through the source as if it were free space. The soft source is most useful when modeling plane waves or waveguide modes because it does not add an incidental PEC plane or a discontinuity to the waveguide.

#### 4.4 Antenna Characteristics

There are three antenna characteristics that are calculated by the FDTD code far-field pattern, input impedance and surface current distribution. Input Impedance is a measurable characteristic of an antenna and is commonly used to predict bandwidth. The surface current distribution is not a measurable characteristic and can only be simulated. However, knowing the surface current distribution can give insight into the performance characteristics of the antenna.

Input impedance calculations are necessary for analyzing antennas. The input impedance is determined from the input voltage and current of the antenna. The FDTD code determines the input current and voltage by applying the following equations where

$$V(t, x_i, y_j, z_k) = - \int_{C_v} \vec{E}(t, x_i, y_j, z_k) \cdot d\vec{l} \quad (4.13)$$

and

$$I(t, x_i, y_j, z_k) = \oint_{C_i} \vec{H}(t, x_i, y_j, z_k) \cdot d\vec{l} \quad (4.14)$$

Once the time domain voltage and current have been found at the input to the antenna, the discrete fourier transform of the voltage and current are calculated to determine the frequency domain voltage and current responses at the feed of the antenna. These values are used to calculate the input impedance using

$$Z_o(\omega, x_i, y_j, z_k) = \frac{F[V(t, x_i, y_j, z_k)]}{F[I(t, x_i, y_j, z_k)]} \quad (4.15)$$

where  $Z_o$  is the input impedance to the antenna that is located at  $(x_i, y_j, z_k)$  for values of  $\omega$ . “ $F$ ” indicates the fourier transform operator.

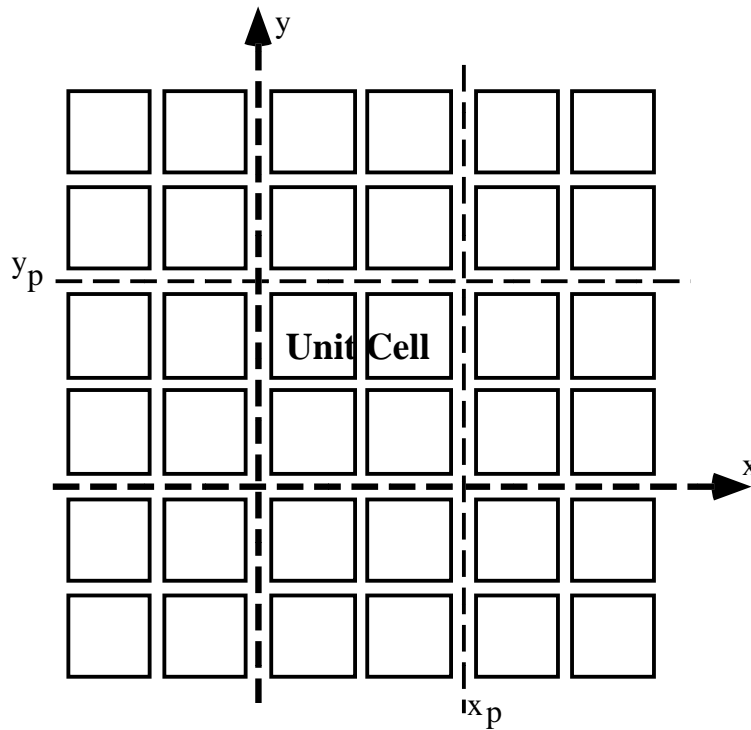
It is often desirable to be able to observe the currents on the surface of the antenna. Visualization of the surface currents is a luxury that can only be obtained through numerical modeling techniques. The surface currents can give insight into the input impedance and radiation characteristics of the antenna. The currents on any surface of the antenna can be found by applying (4.14) to all the grid positions on the desired PEC surface. This method yields current magnitude and direction of the surface currents. The time domain currents on the surface can be stored in memory, however, for large surfaces the memory space required would be significant. Therefore, the frequency domain currents, for specified frequencies, found from the discrete fourier transform of the currents in the time domain, are stored in memory. Visualization of these surface currents is useful for understanding variations in radiation characteristics with frequency.

#### 4.5 Infinite Array

In large arrays elements not at the edge of the array are effectively in an infinite array environment. Modeling a large finite array requires large amounts of computer memory

and long computational times. An alternative is to model the element in an infinite array environment. An infinite array model requires only the memory to model a single element, though edge elements are neglected. For an infinite array solution to converge, run times longer than that of a single element are required.

An infinite array of antenna elements can be modeled using the FDTD method by applying periodic boundary conditions to the four sides of the unit cell shown in Fig. 4.1.



**Figure 4.1** Unit cell of two dimensional infinite array

The periodic boundary conditions require that the fields on one side of the unit cell be equal to field values on the parallel side. The two dimensional infinite array, boundary conditions for the H-fields are

$$\begin{aligned}
H_z(x_p, j, k) &= H_z(0, j, k) \\
H_y(x_p, j, k) &= H_y(0, j, k) \\
H_z(i, y_p, k) &= H_z(i, 0, k) \\
H_x(i, y_p, k) &= H_x(i, 0, k)
\end{aligned} \tag{4.15}$$

The two dimensional infinite array, boundary conditions for the E-fields are

$$\begin{aligned}
E_z(0, j, k) &= E_z(x_p, j, k) \\
E_y(0, j, k) &= E_y(x_p, j, k) \\
E_z(i, 0, k) &= E_z(i, y_p, k) \\
E_x(i, 0, k) &= E_x(i, y_p, k)
\end{aligned} \tag{4.16}$$

By applying the four H-field and four E-field boundary conditions the antenna within the unit cell is an element of a fully excited infinite array. Therefore, the voltage and current at the input to the antenna can be found from (4.13) and (4.14). Then by substituting into (4.15) the input impedance of the element in a fully excited array is determined.

## 4.6 Summary

The FDTD code requires many subroutines to model an antenna accurately. The most important subroutine is the UPML ABC's and update equations. If this subroutine is not formulated correctly it effects the results of all the other subroutines. For antenna modeling other subroutines are required to model the PEC structure of the antenna and the source. From these models antenna characteristics such as far-field pattern, input impedance and surface current distribution can be determined.

## FOURSQUARE ANTENNA

It is difficult to realize element antennas that have acceptable electrical performance over wide bandwidth when operating in an array. Some element antennas have broad bandwidth but are not small enough to fit into the grid required to realize the maximum scan angle over the desired array bandwidth as seen in Fig. 3.1. In addition, many small, broadband elements, such as the equiangular spiral and the Archimedean spiral, are not dual polarized. To meet the demands of the broadband, scanning array a new element, the Foursquare, was designed, constructed and measured at the Virginia Tech Antenna Lab. The Foursquare antenna has desirable characteristics for use as a broadband, scanning array element. These characteristics include nearly equal E- and H-plane patterns, a 1.4:1 impedance and pattern bandwidth and a small size of planar dimension,  $D = 0.36 \lambda_L$ , where  $\lambda_L$  is the wavelength at the lower frequency of operation. Though several prototypes of the Foursquare antenna were built and measured, the operation of the antenna was not fully understood.

The broadband characteristics of the Foursquare antenna were modeled using an FDTD code. The far-field patterns and input impedance calculated by the FDTD program compare well with the measured data, giving confidence in the code. The FDTD program's advantage over measured data is that it can be used to calculate the currents flowing on the antenna. These currents give insight into the broadband characteristics of the Foursquare.

The Foursquare antenna has a simple architecture, consisting of four metallic squares arranged in a 2-by-2 array configuration as shown in Fig. 5.1. Though the Foursquare is easily fabricated by etching the metallic squares on a printed circuit board, this antenna is not a patch antenna. Microstrip patch antennas have a single (unbalanced) feed and are mounted close to the ground plane, usually at a height much less than a wavelength.

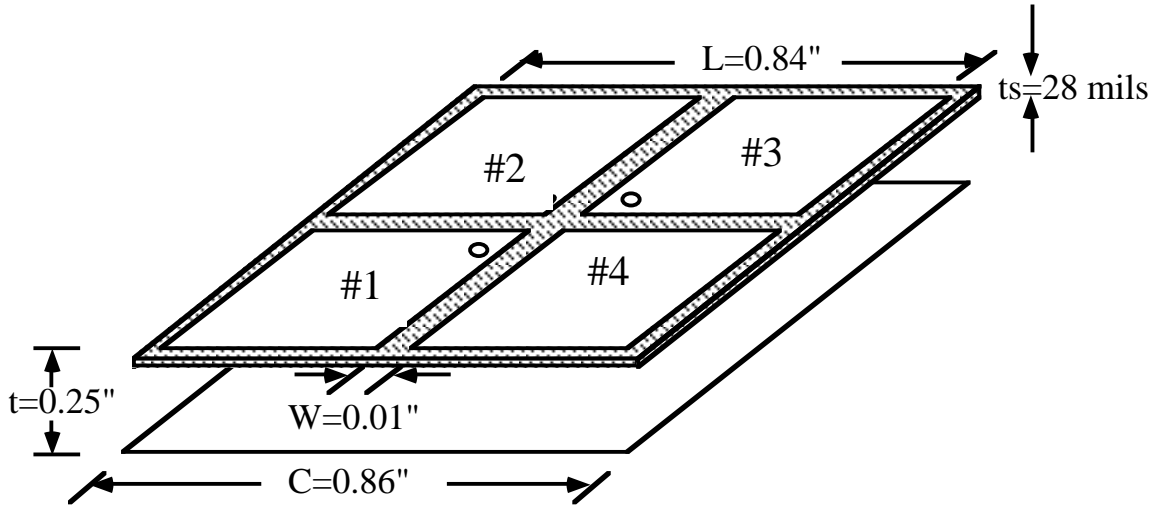
Because the patch antenna is close to the ground plane, the element radiates from the fringing fields at the edges of the patch.

The Foursquare antenna is distinguished from the patch antenna by its radiation from the currents flowing on the surface of the antenna. The Foursquare is placed approximately  $0.15 \lambda$  above the ground plane at the center frequency. The Foursquare antenna's balanced transmission line feed is connected across the two diagonally opposed central corners of two squares. The Foursquare antenna radiation mechanism is more closely related to a dipole over a ground plane. The squares not connected to the feed act as parasitic elements, and can be fed separately to produce circular or orthogonal linear polarizations. Thus, diagonally opposing squares are fed as pairs, producing and orthogonal linear polarization. These two perpendicularly polarized fed outputs can also be combined to produce RHCP and LHCP with the appropriate phase shift between the excitations [21].

## 5.1 The Foursquare Element Geometry

The Foursquare antenna was developed by the Virginia Tech Antenna Group in response to requests for compact broadband array elements. The prototype Foursquare that was built and tested at Virginia Tech is shown in Fig. 5.1. This antenna has a dimension,  $L$ , of 0.84". The dimension,  $C$ , of the antenna is 0.86" which includes  $L$  plus the 0.01" space surrounding the squares. The squares have a separation of  $W=0.01$ ". The squares are etched on a one-sided printed circuit board made of Duroid 5870 with a thickness of  $t_s=28$ mils, and a relative permittivity of  $\epsilon_r=2.33$ . The printed circuit board is placed a distance  $t_d=0.25$ " above the ground plane using Styrofoam ( $\epsilon_r=1.01$ ). These Foursquare parameters are tabulated in Table 5.1.





Frequency (GHz)	L	t
4.50	$0.32\lambda$	$0.106\lambda$
6.00	$0.43\lambda$	$0.141\lambda$
7.25	$0.52\lambda$	$0.171\lambda$

**Figure 5.1** Geometry of the prototype Foursquare antenna.

**Table 5.1** Foursquare antenna parameters

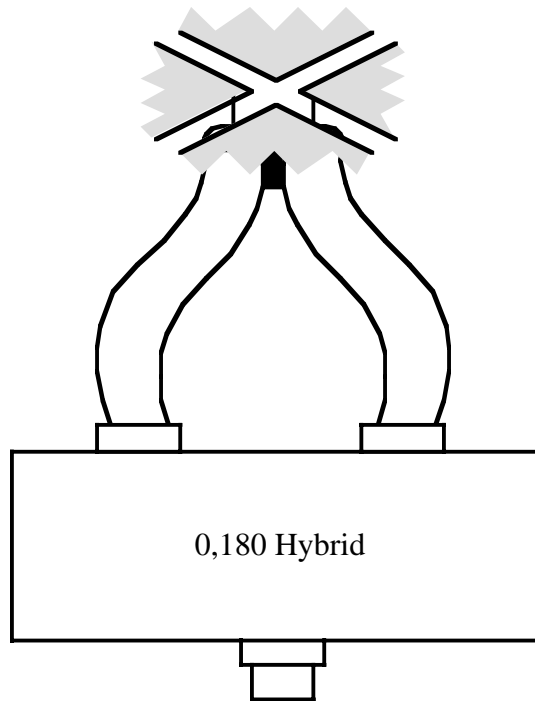
Parameter	Symbol	Value (SI)	Value
Substrate Thickness	$t_s$	0.071 cm	28 mils
Distance from ground plane	$t_d$	0.625 cm	0.25"
Side Length of Foursquare	L	2.13 cm	0.84"
Side Length, Including Distance Between Elements	C	2.18 cm	0.86"
Spacing Between Squares	W	0.025 cm	0.01"
Relative Dielectric Constant	$\epsilon_r$	2.33	2.33

## 5.2 The Foursquare Element Experimental Results

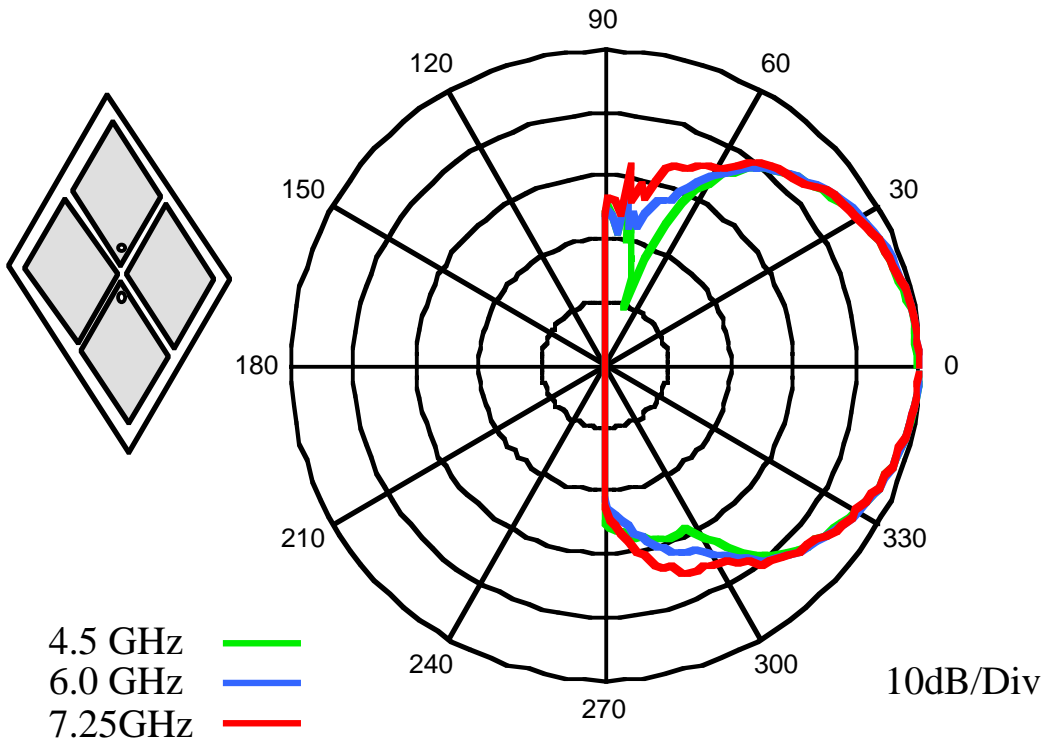
The E- and H-plane patterns of the Foursquare antenna in Fig. 5.1 were measured on the antenna range from 4 to 8 GHz with uniform E- and H-plane patterns from 4.5 to 7.25 GHz. The input impedance was measured from 4 to 8 GHz and was found to be nearly constant from 5 to 7 GHz [28].

### 5.2.1 Measured Far-Field Patterns

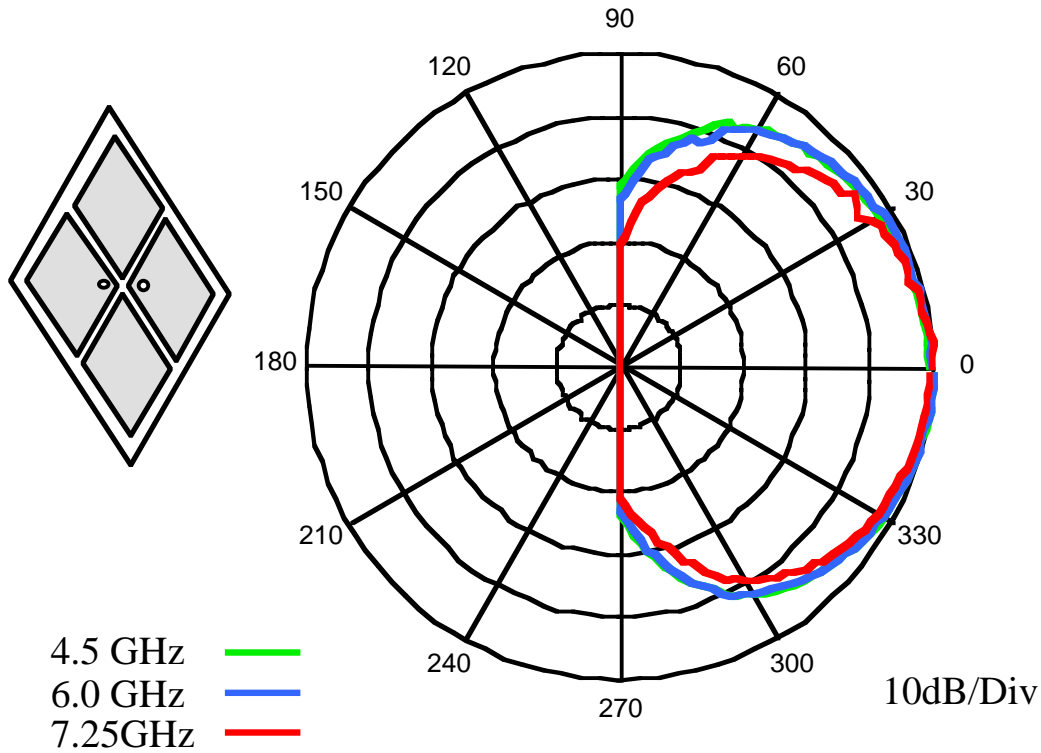
The Foursquare far-field patterns were measured on the 20 m-outdoor antenna range at Virginia Tech. The range provides good results for frequencies above 4 GHz. Both E- and H-plane patterns were measured. The E-plane of the Foursquare antenna cuts diagonally through the two squares attached to the feed lines, i.e. the plane contained the dots on the squares shown in Fig. 5.1. The H-plane pattern is perpendicular to the E-plane pattern and cuts diagonally through the parasitic elements. To create a balanced feed the Foursquare element was fed using a  $0^\circ/180^\circ$  hybrid. The  $0^\circ$  output of the hybrid is connected at the inside corner of one square and the  $180^\circ$  output is connected to the inside corner of the diagonally opposing squares as shown in Fig 5.2. The outer conductors of the  $0^\circ$  and  $180^\circ$  outputs are soldered together near the squares. The E- and H-plane patterns were measured at several different frequencies using this configuration. The 4.5, 6.0, and 7.25 GHz patterns are shown for both the E- and H-planes in Fig. 5.3 and Fig. 5.4. The cross-pole patterns are below the noise floor of the measurements and therefore are not shown. The E- (H-plane) patterns of the 4.5 and 7.25 GHz patterns have small variation from the E- (H-plane) patterns at 6.0 GHz, the center of the frequency band. In addition, the E- and H-plane patterns are not greatly different, distinguishing the antenna from others such as the half-wave dipole. This property is desirable for full scan phased arrays. This constant pattern and impedance behavior is characteristic of frequency independent antennas.



**Figure 5.2** Foursquare feed connections through a  $0^\circ/180^\circ$  hybrid to create a balanced feed for pattern measurements.



**Figure 5.3** Measured E-plane pattern of the prototype Foursquare antenna of Fig. 5.1.



**Figure 5.4** Measured H-plane pattern of the prototype Foursquare antenna of Fig. 5.1.

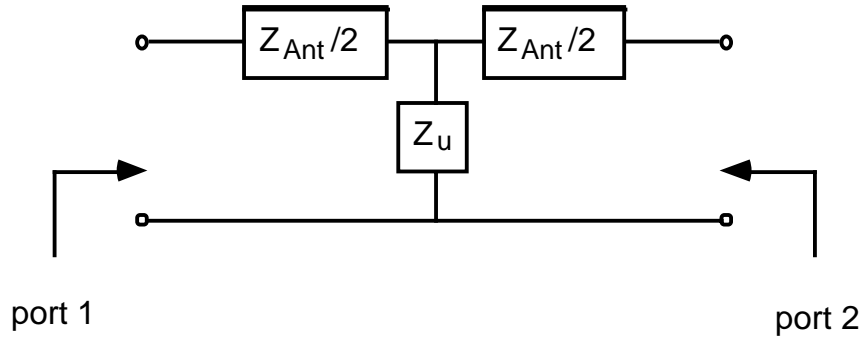
### 5.2.2 Measured Input Impedance

The input impedance characteristics of the Foursquare antenna limits the bandwidth of the element. Power is radiated by the antenna at frequencies where the input impedance is nearly real-valued. VSWR is used to quantify impedance mismatch. VSWR is the ratio of the maximum voltage to the minimum voltage of the standing wave caused by the impedance mismatch between the transmission line impedance and the antenna input impedance. The percent reflected power is related to the VSWR as [18]

$$P^r = \left( \frac{VSWR - 1}{VSWR + 1} \right)^2 \quad (5.1)$$

In all the calculations the VSWR is referenced to a 50  $\Omega$  line.

The input impedance was measured using an HP 8510B network analyzer. Coaxial transmission lines feed the two inputs of the Foursquare antenna with the outer conductors soldered together near the ports. The antenna was measured as a two-port device where the 0° input of the antenna is port 1 and the 180° input is port 2. The two ports of the network analyzer are calibrated at the input of the Foursquare. This configuration measures the input impedance of the two-port circuit that is shown in Fig. 5.5, where  $Z_{Ant}$  is the input impedance to the antenna and  $Z_u$  is the coupling between the two ports at the antenna feed. Derivation of the input impedance for another equivalent circuit configuration is described in [29]



**Figure 5.5** Two port circuit model of the Foursquare antenna and feed. Ports 1 and 2 represent the two feed points of the antenna.

To find the input impedance of the antenna,  $S_{11}$  and  $S_{21}$  of the two-port configuration are measured using the network analyzer. The ABCD two-port parameters of Fig. 5.5 are given as [30]

$$A = 1 + \frac{Z_{Ant}}{2Z_u} \quad (5.2a)$$

$$B = Z_{Ant} + \frac{Z_{Ant}^2}{4Z_u} \quad (5.2b)$$

$$C = \frac{1}{Z_u} \quad (5.2c)$$

$$D = 1 + \frac{Z_{Ant}}{2Z_u} \quad (5.2d)$$

The scattering parameters  $S_{11}$  and  $S_{21}$  of the two-port circuit can easily be found from the ABCD parameters using the transformations given as [30]

$$S_{11} = \frac{A + B/Z_0 - CZ_0 - D}{A + B/Z_0 + CZ_0 + D} \quad (5.3a)$$

$$S_{21} = \frac{2}{A + B/Z_0 + CZ_0 + D} \quad (5.3b)$$

Substituting (5.2) into (5.3) yields  $S_{11}$  and  $S_{21}$  given in terms of  $Z_{Ant}$  and  $Z_u$  as

$$S_{11} = \frac{Z_{Ant}Z_u + Z_{Ant}^2/4 - Z_0}{2Z_uZ_0 + Z_{Ant}Z_0 + Z_{Ant}Z_u + Z_{Ant}^2/4 + Z_0^2} \quad (5.4a)$$

$$S_{21} = \frac{2Z_0Z_u}{2Z_uZ_0 + Z_{Ant}Z_0 + Z_{Ant}Z_u + Z_{Ant}^2/4 + Z_0^2} \quad (5.4b)$$

Both equations are in terms of  $Z_{Ant}$  and  $Z_u$  and neither are known values. The reflection coefficient,  $\Gamma$ , at the antenna, which is only a function of  $Z_{Ant}$  and the characteristic

impedance  $Z_0$ , is given by

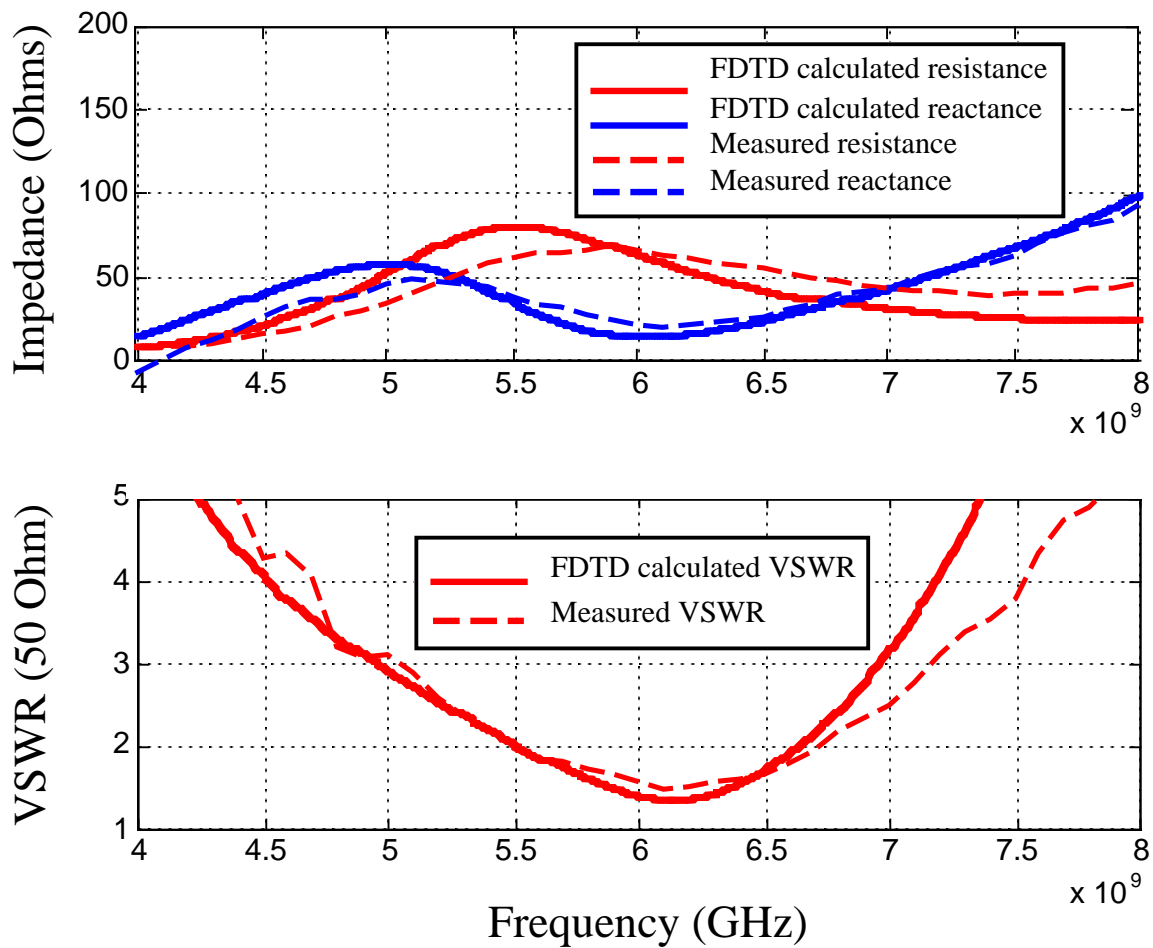
$$\Gamma = S_{11} - S_{21} = \frac{Z_{Ant} - 2Z_0}{Z_{Ant} + 2Z_0} \quad (5.5)$$

Solving for  $Z_{Ant}$  gives

$$Z_{Ant} = 2Z_0 \frac{1 + S_{11} - S_{21}}{1 - S_{11} + S_{21}} \quad (5.6)$$

Given the measured values of  $S_{11}$  and  $S_{21}$ , the input impedance of the antenna can be found using (5.6).

The measured input impedance and VSWR for the prototype Foursquare antenna of Fig. 5.1 are shown in Fig. 5.6. The impedance bandwidth of the Foursquare antenna is 1.4:1 for a VSWR less than 3 over the frequency range from 5 to 7 GHz.



**Figure 5.6** Measured and modeled input impedance and VSWR for the prototype Foursquare antenna of Fig. 5.1.



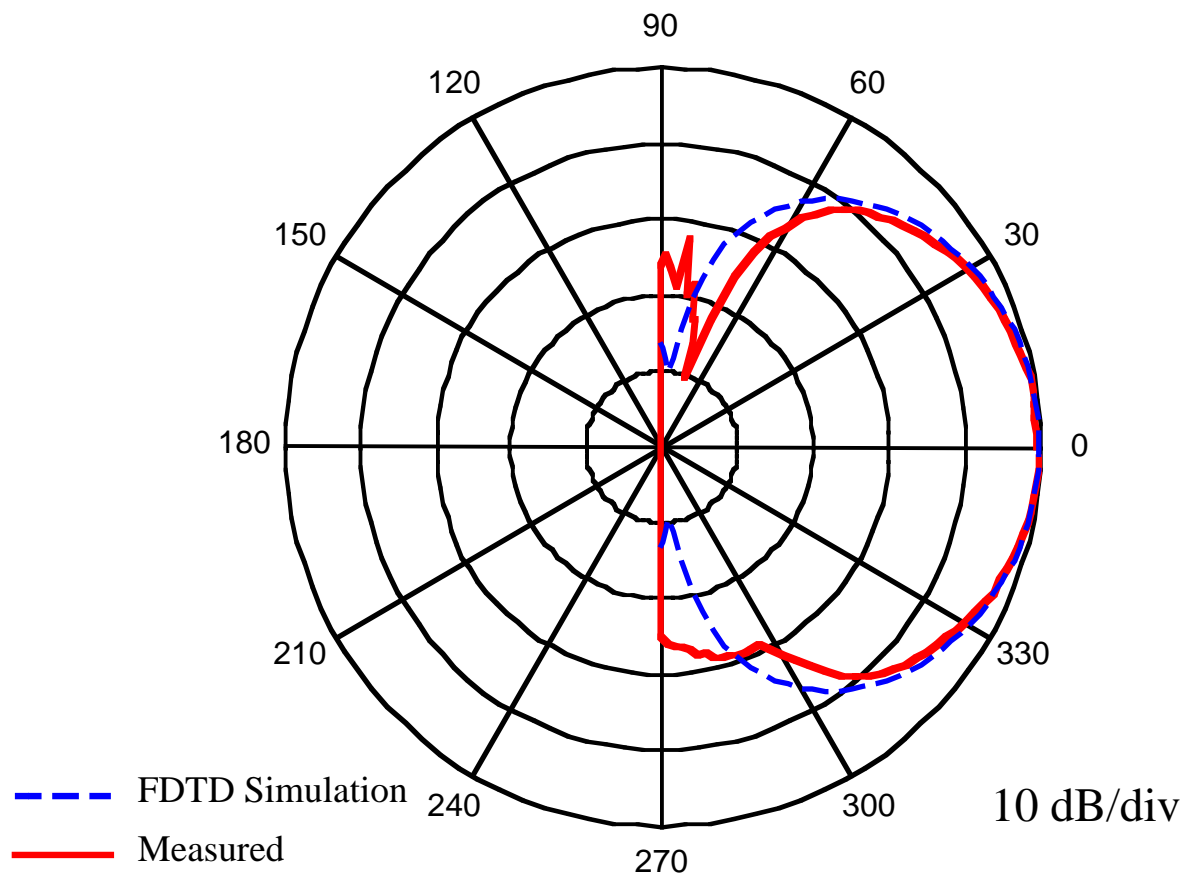
### 5.3 FDTD Model Results for the Foursquare Antenna

The FDTD program, described in Chapter 4, for modeling antennas was used to aid in understanding the broadband characteristics of the Foursquare antenna. Characteristics such as the current distribution and design parameter variation influence can be examined with the FDTD numerical analysis tool. Confidence is gained in the accuracy of the computed current distribution by first comparing computed and measured radiation patterns and impedance. Confirmation of the FDTD program provides confidence in the modeled current distribution, that cannot be measured, and the variations in the characteristics due to design parameter changes.

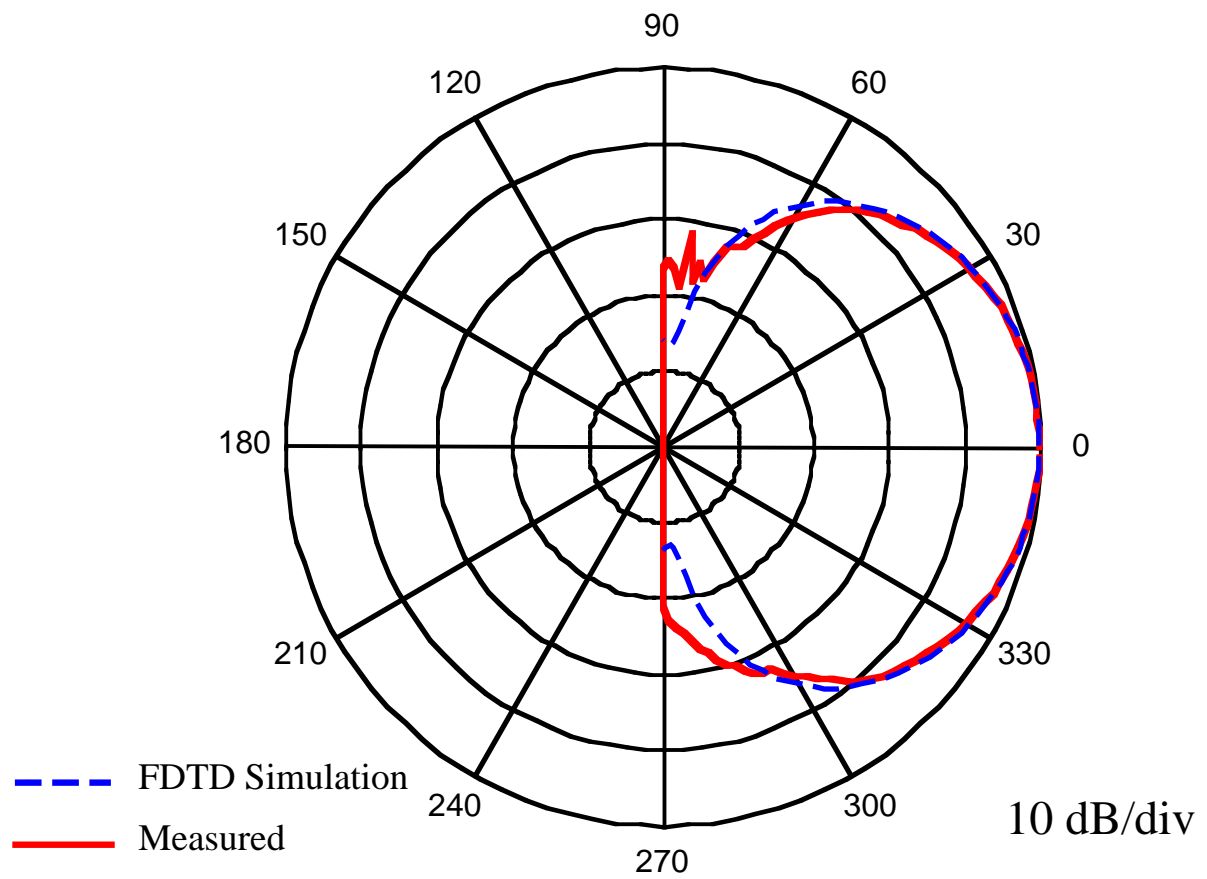
The Foursquare element is modeled in the FDTD program as four infinitesimally thin perfectly conducting squares. Each square is 42x42 cells with a 1 cell spacing between the squares. The cell size is 0.01". A dielectric substrate below the squares has  $\epsilon_r=2.33$  and is three cells thick. The ground plane is infinite in extent with apertures to allow for parallel transmission line connections to the feed of the Foursquare antenna. The ground plane is placed 25 cells below the dielectric. The parallel wire feed lines are attached to the corners of the diagonally opposing squares.

#### 5.3.1 Modeled Far-Field Patterns

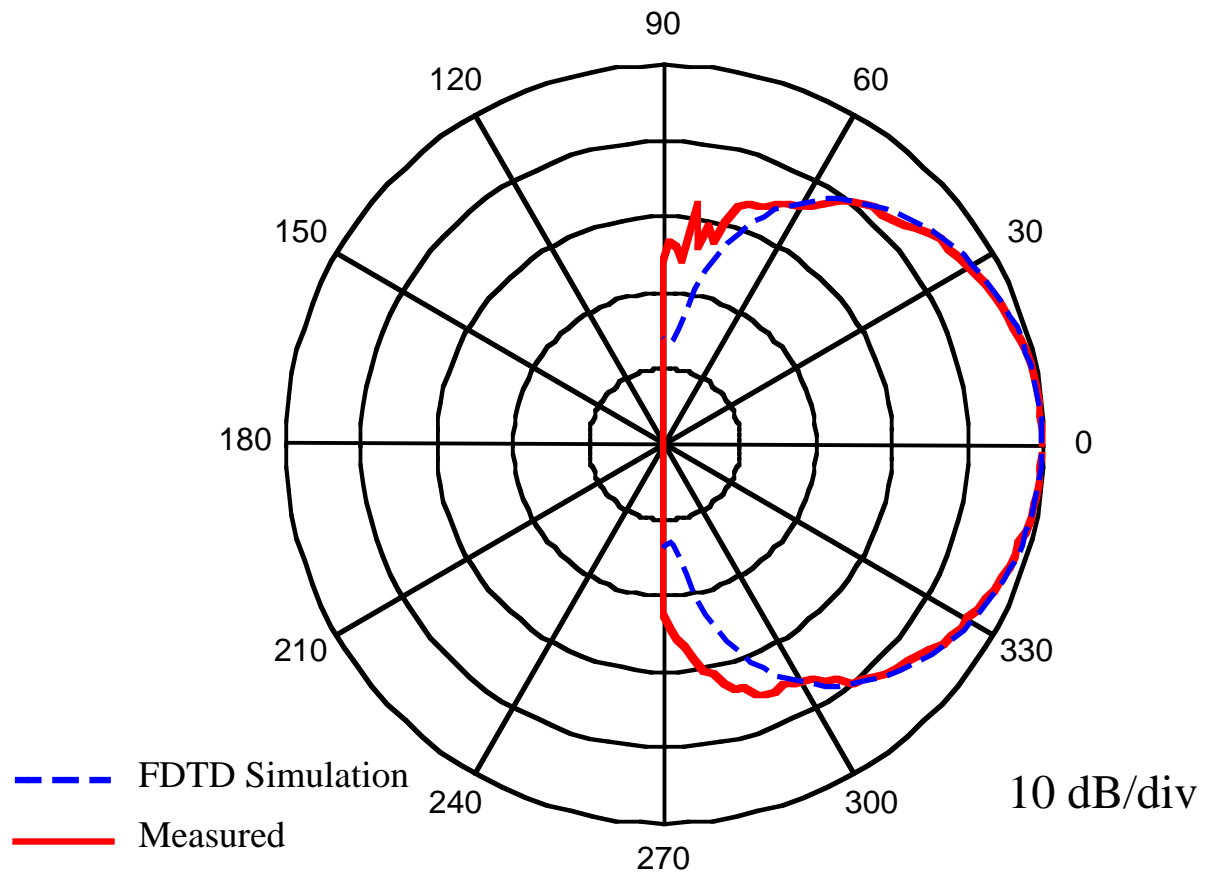
The E-plane pattern was calculated in the plane passing diagonally through the two feed squares. The H-plane pattern was calculated in the plane perpendicular to the E-plane. The measured versus FDTD calculated far-field patterns are in close agreement, as shown in Figures 5.7 through 5.12. The pattern in the 45°-plane, located between the E-plane and H-plane, was also calculated and is shown in Figures 5.13 through 5.15. The 45°-plane pattern shape is intermediate between the E-plane to H-plane pattern shapes, as expected. The symmetry of the Foursquare antenna structure dictates that there will be no cross-pole pattern in the simulated data.



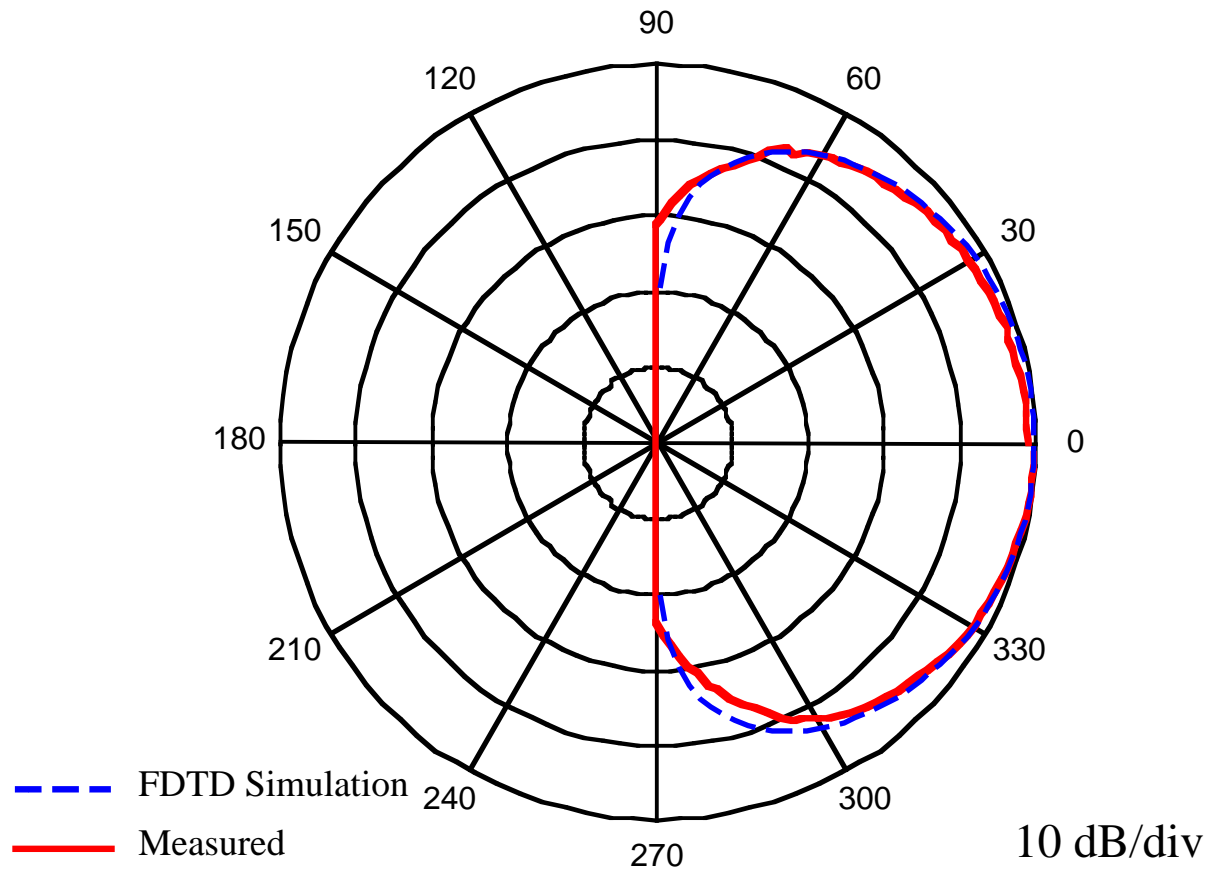
**Figure 5.7** Calculated and measured E-plane patterns of the Foursquare antenna of Fig. 5.1 at 4.5 GHz.



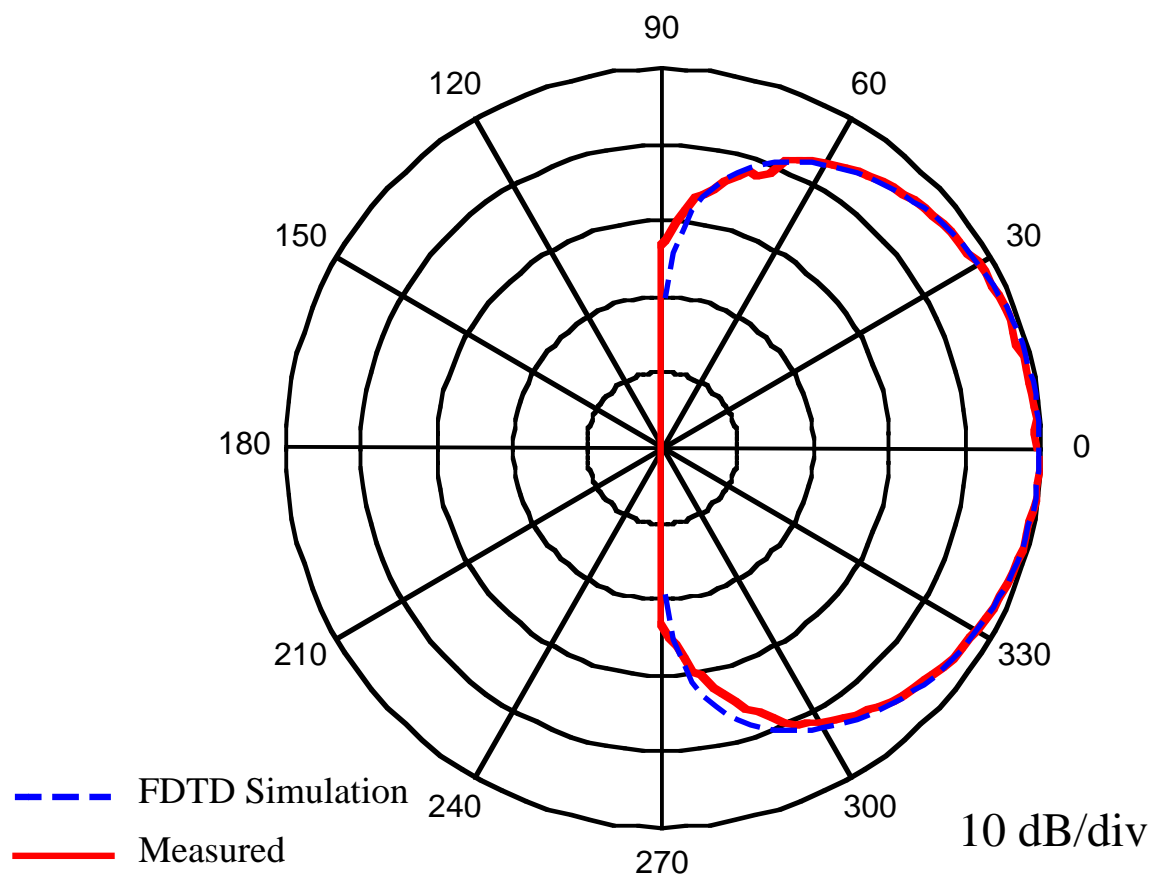
**Figure 5.8** Calculated and measured E-plane patterns of the Foursquare antenna of Fig. 5.1 at 6.0 GHz.



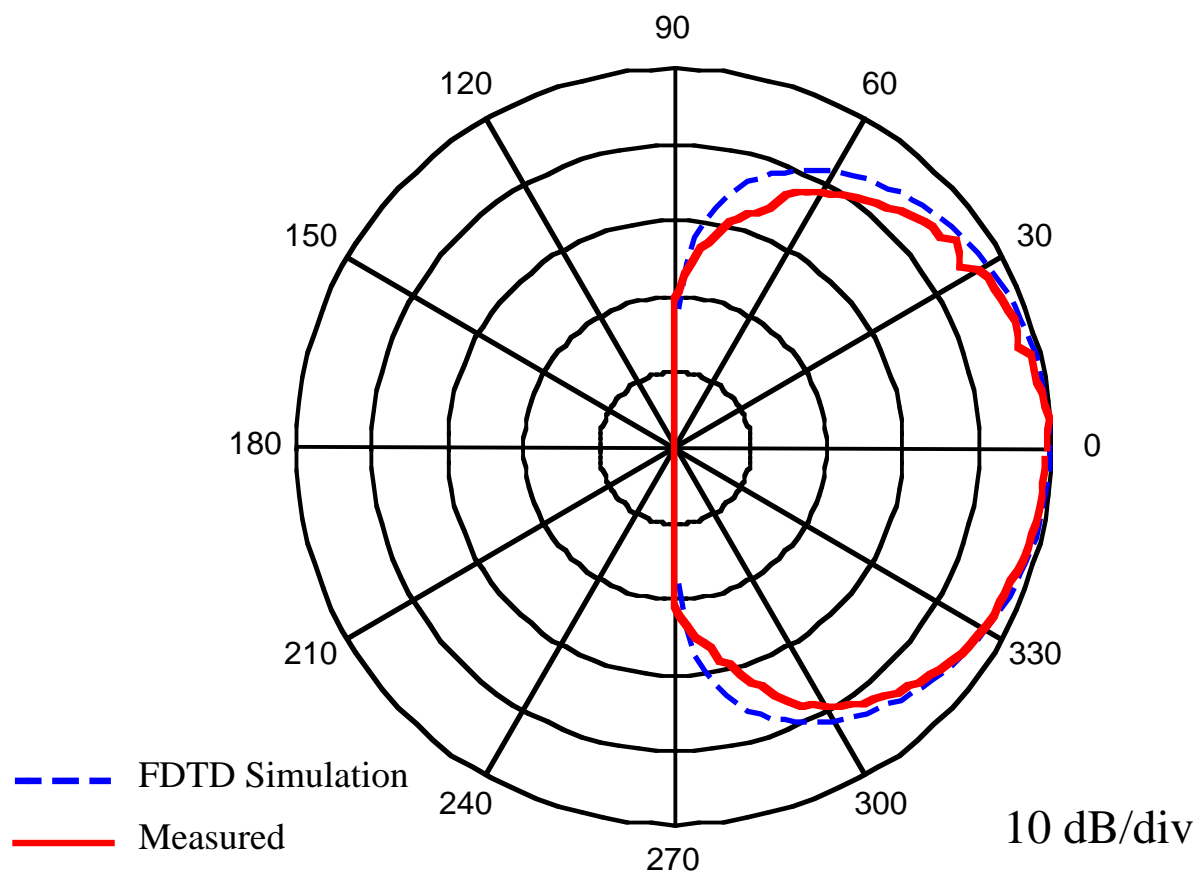
**Figure 5.9** Calculated and measured E-plane patterns of the Foursquare antenna of Fig. 5.1 at 7.25 GHz.



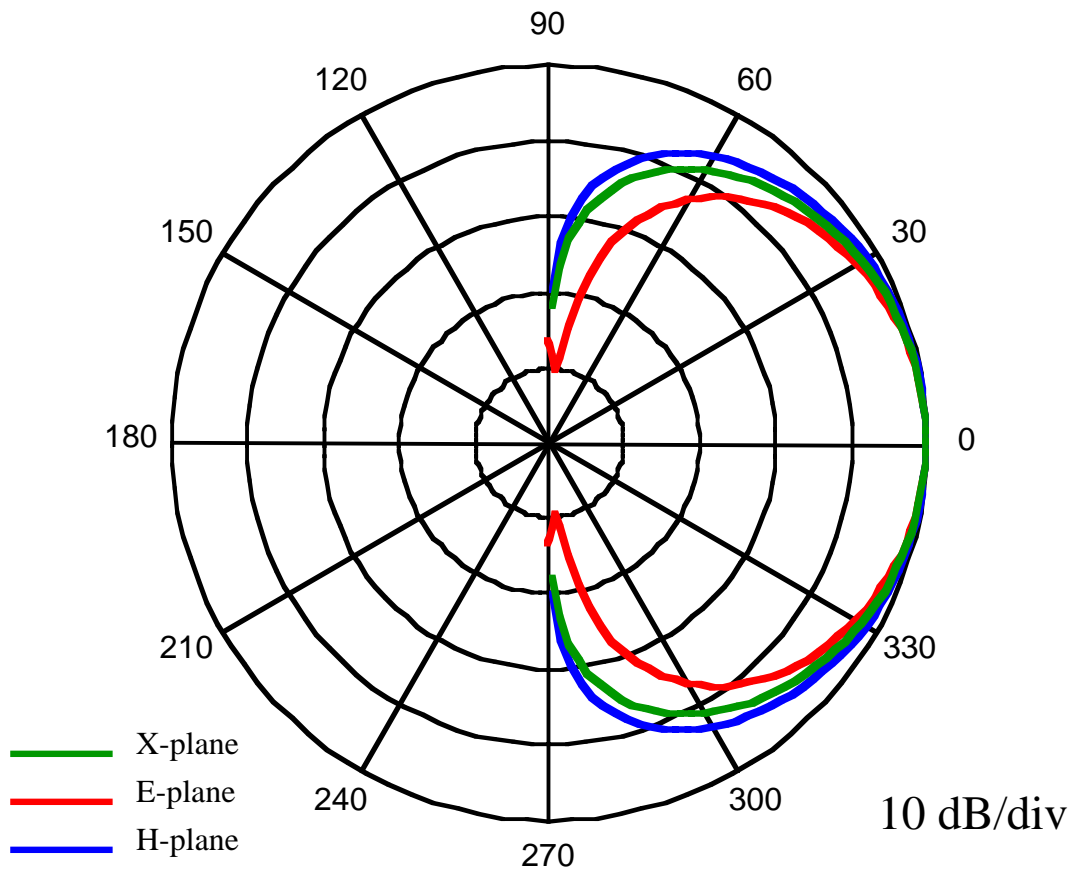
**Figure 5.10** Calculated and measured H-plane patterns of the Foursquare antenna of Fig. 5.1 at 4.5 GHz.



**Figure 5.11** Calculated and measured H-plane patterns of the Foursquare antenna of Fig. 5.1 at 6.0 GHz.

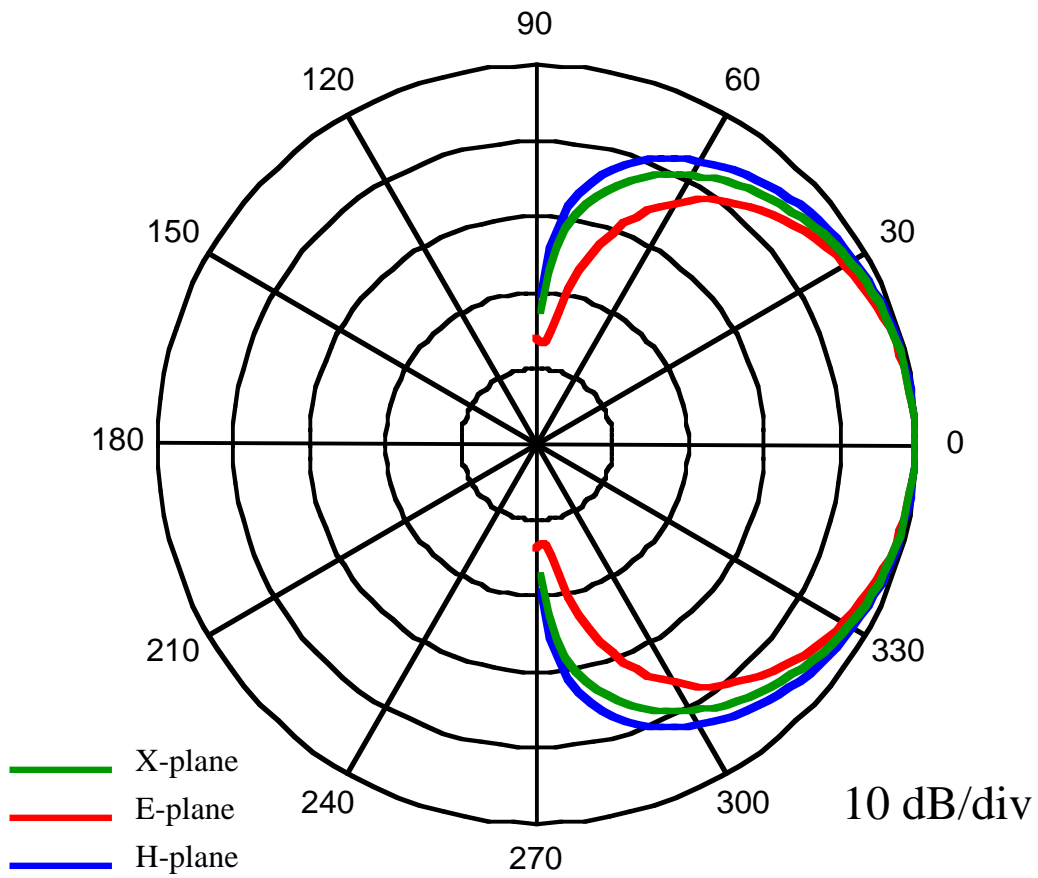


**Figure 5.12** Calculated and measured H-plane patterns of the Foursquare antenna of Fig. 5.1 at 7.25 GHz.

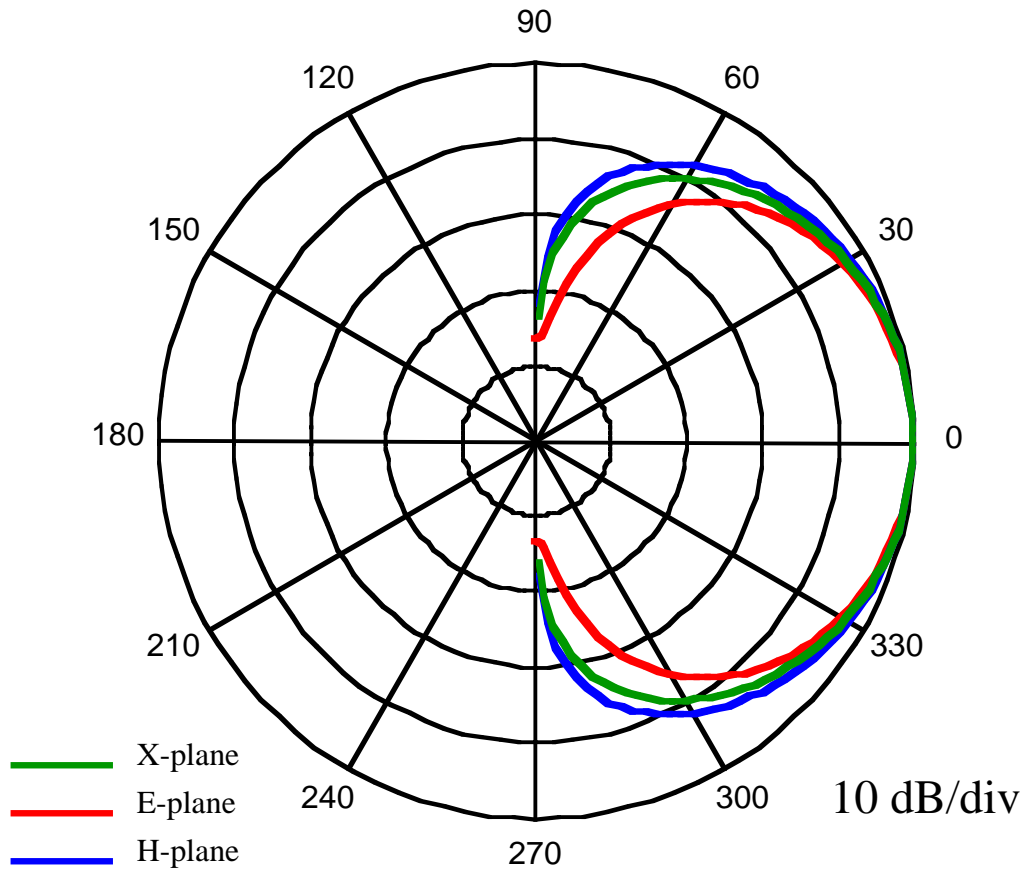


**Figure 5.13** Computed 45°-plane, E-plane and H-plane patterns of the Foursquare antenna of Fig. 5.1 at 4.5 GHz.





**Figure 5.14** Computed 45°-plane, E-plane and H-plane patterns of the Foursquare antenna of Fig. 5.1 at 6.0 GHz



**Figure 5.15** Computed 45°-plane, E-plane and H-plane patterns of the Foursquare antenna of Fig. 5.1 at 7.25 GHz

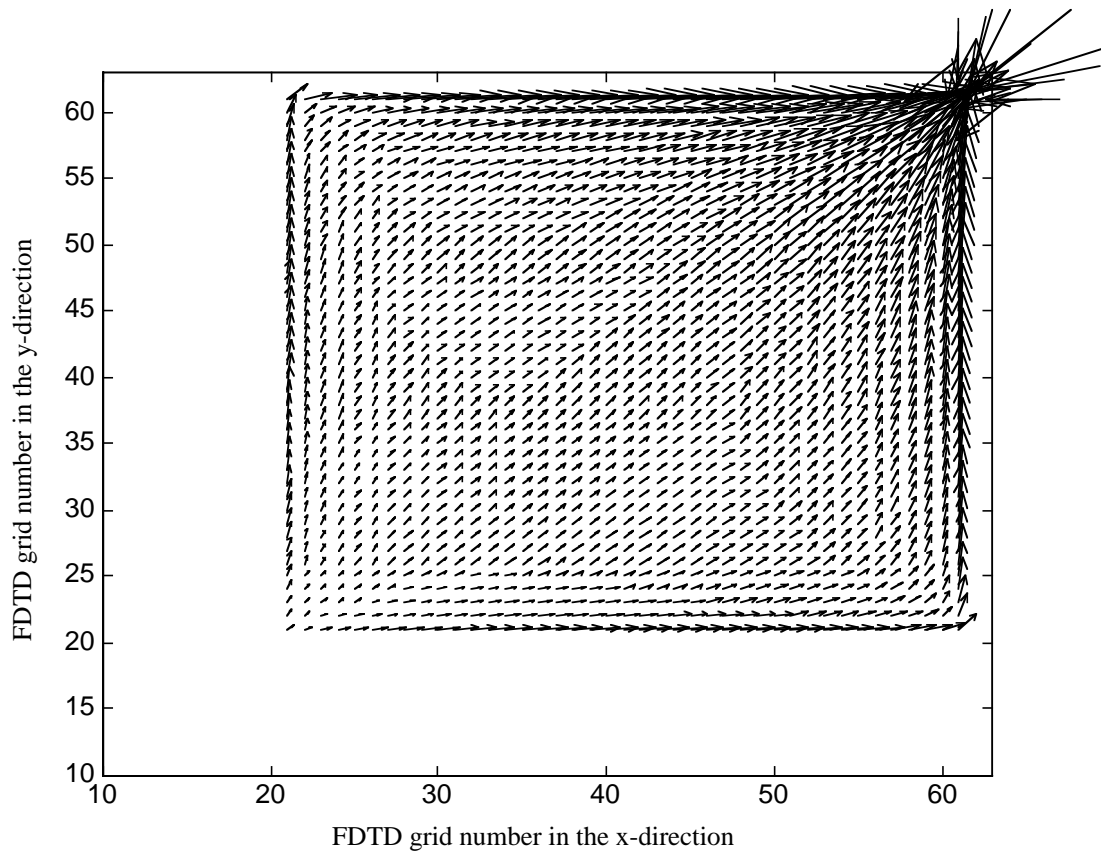
### 5.3.2 Modeled Input Impedance

The input impedance of the Foursquare antenna was modeled using the FDTD code. The feed to the antenna was modeled as a parallel transmission line fed through an infinite PEC plate. The current was calculated on the transmission line at the feed points of the Foursquare antenna. The voltage was calculated across the feed of the Foursquare antenna. The discrete Fourier transform of the frequency domain voltage and current were calculated to find the input impedance of the Foursquare antenna versus frequency from (4.3.4). The results of the input impedance calculations are compared to the measured input impedance and VSWR in Fig. 5.6.

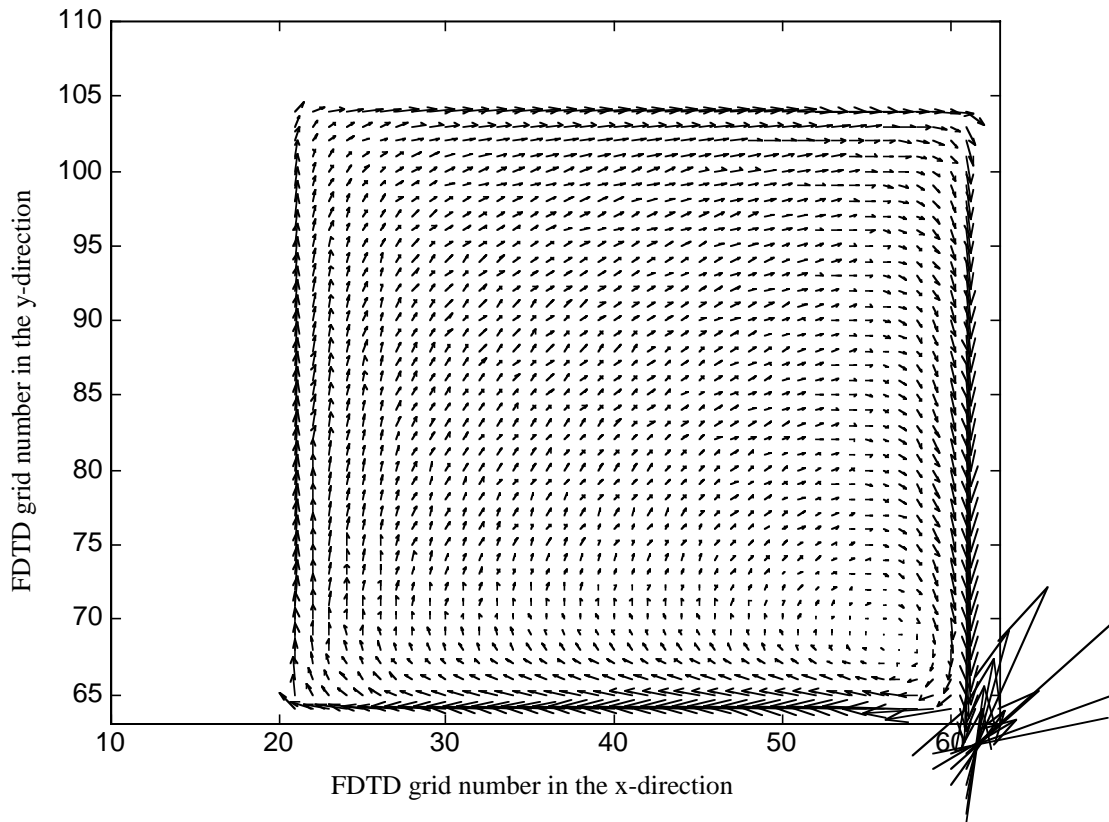
### 5.3.3 Modeled Current Distribution

The current distribution on the Foursquare gives insight into the operation of the antenna. The current distribution on the surface of the antenna was found from (4.2.1a). The current distribution for one parasitic square, #2, and one diagonally excited square, #1, as numbered in Fig. 5.1, is shown in Figures 5.16-5.21 for 5, 6 and 7 GHz. The surface currents on squares #3 and #4 can be determined by symmetry. The FDTD code gives the currents as  $x$ - and  $y$ -directed currents that exist at positions on off-set grids on the surface of the antenna. A linear interpolation in the  $y$ -direction of the  $x$ -directed currents and a linear interpolation in the  $x$ -direction of the  $y$ -directed currents places these currents at the same position. These  $x$ - and  $y$ -directed interpolated currents form the vector plots of Figures 5.16-5.21, which graphically show the magnitude and direction of the current flow on the surface of the Foursquare antenna. The vector length is proportional to the magnitude of the current and the vector direction is pointing in the direction of the current arrow.

The lower end of the frequency band at 5 GHz has dominant current flow on the diagonally excited squares; see Fig. 5.16. The current on the parasitic square is small and circulatory; see Fig. 5.17. This is a reasonable expectation for the current flow since at the low frequencies of operation the wavelengths are long and the active region of the current occupies a large region of the metallic area.

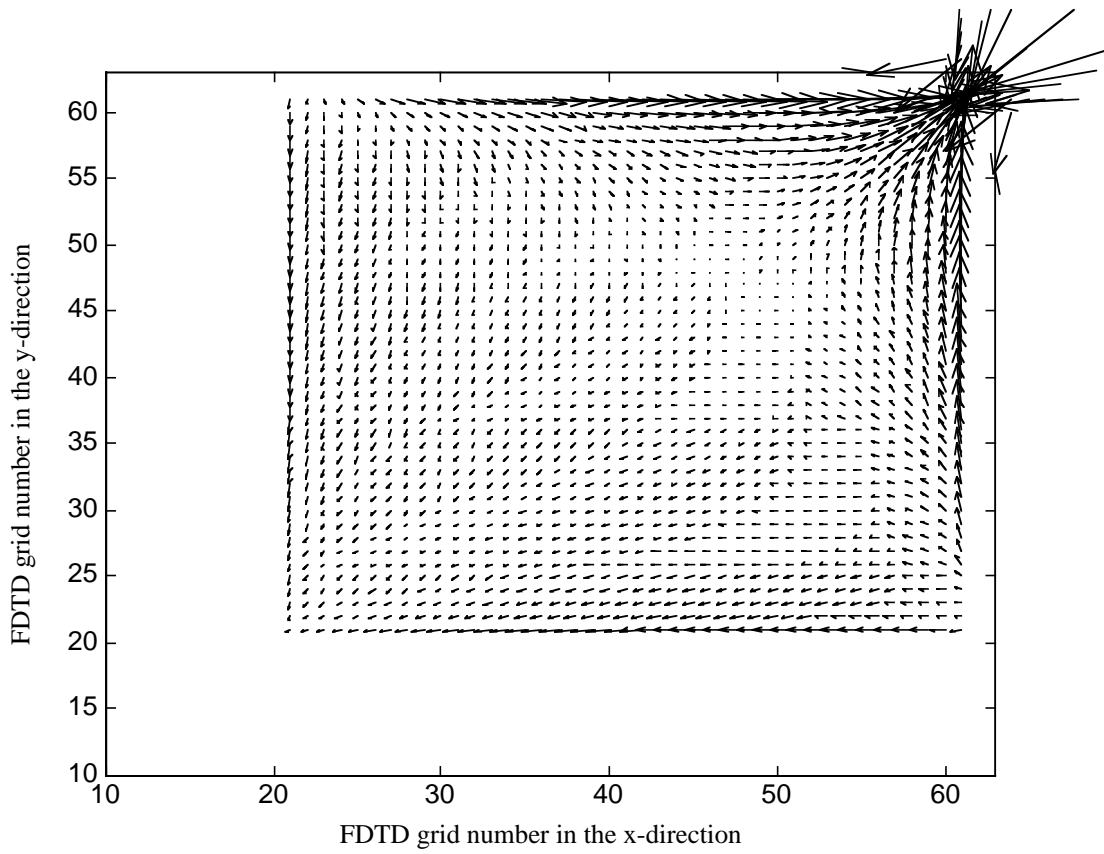


**Figure 5.16** Current distribution at 5 GHz on square #1 of the excited pair on the Foursquare antenna of Fig. 5.1.

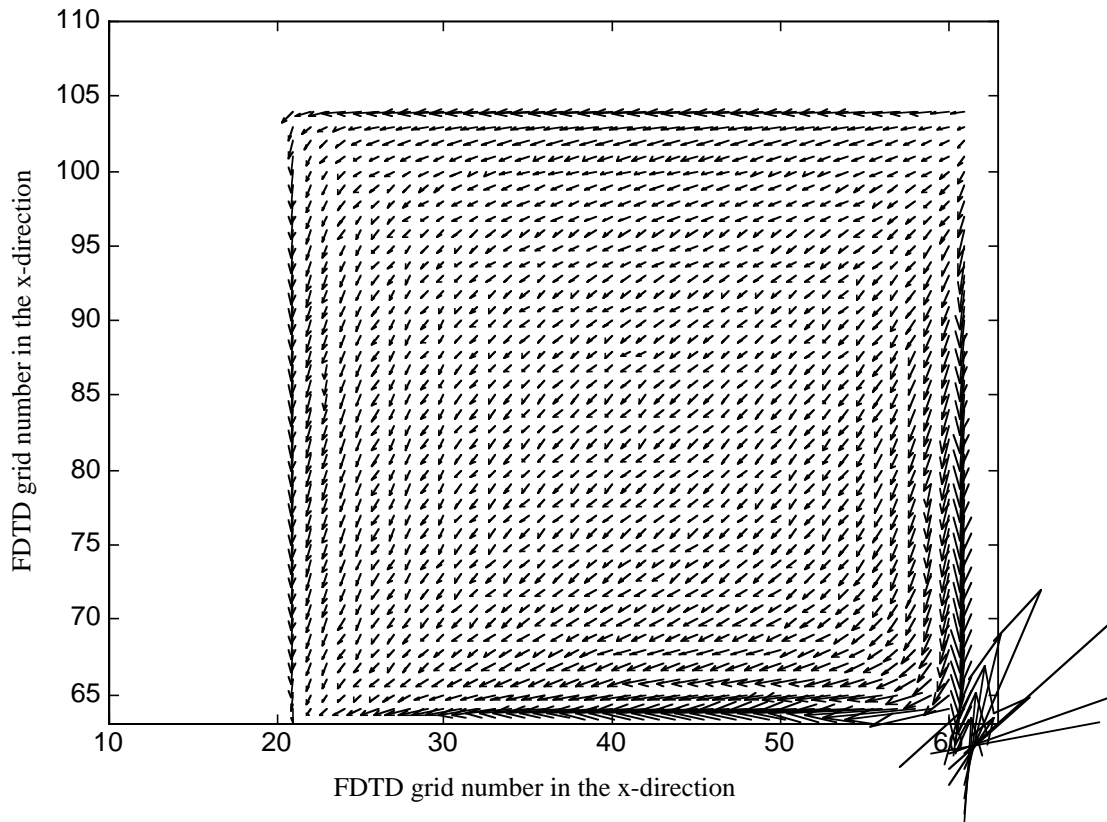


**Figure 5.17** Current distribution at 5 GHz on square #2 of the parasitic squares on the Foursquare antenna of Fig. 5.1.

The currents at the mid-band frequency of 6 GHz distributed across both the diagonally excited squares and the parasitic squares; see Fig. 5.18 and Fig. 5.19. Therefore, the current is radiating from both squares.

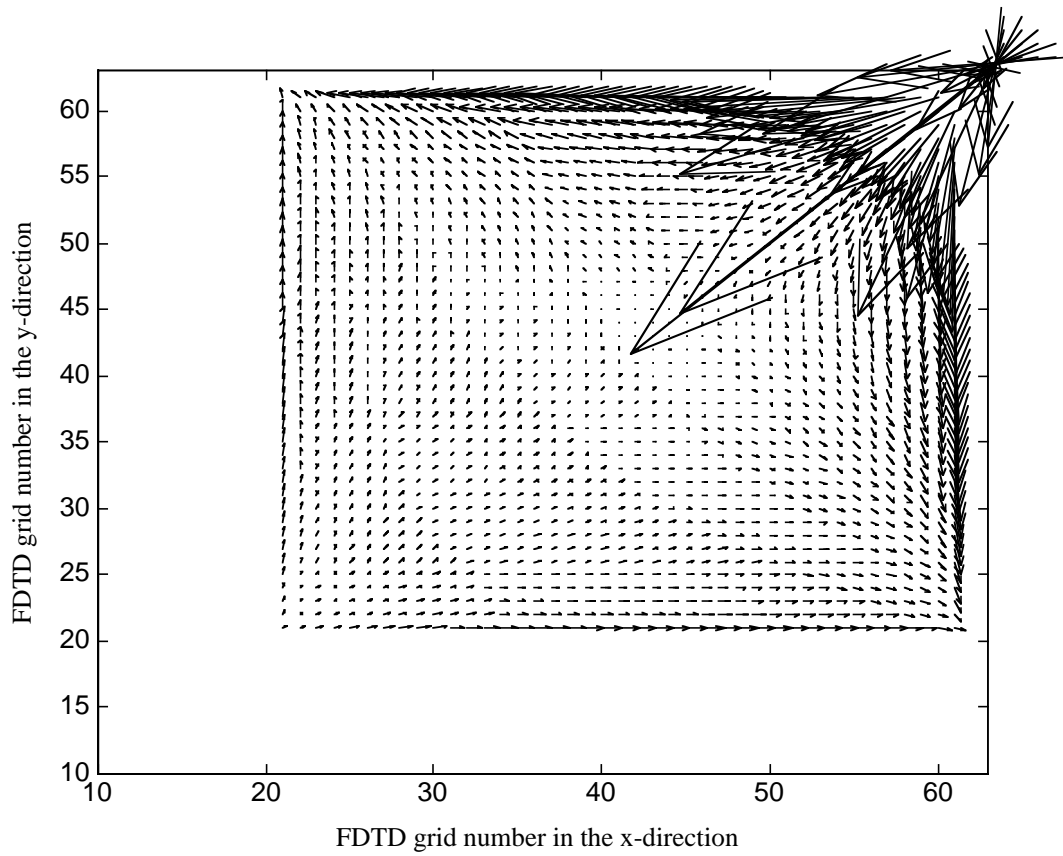


**Figure 5.18** Current distribution at 6 GHz on square #1 of the excited pair on the Foursquare antenna of Fig. 5.1.



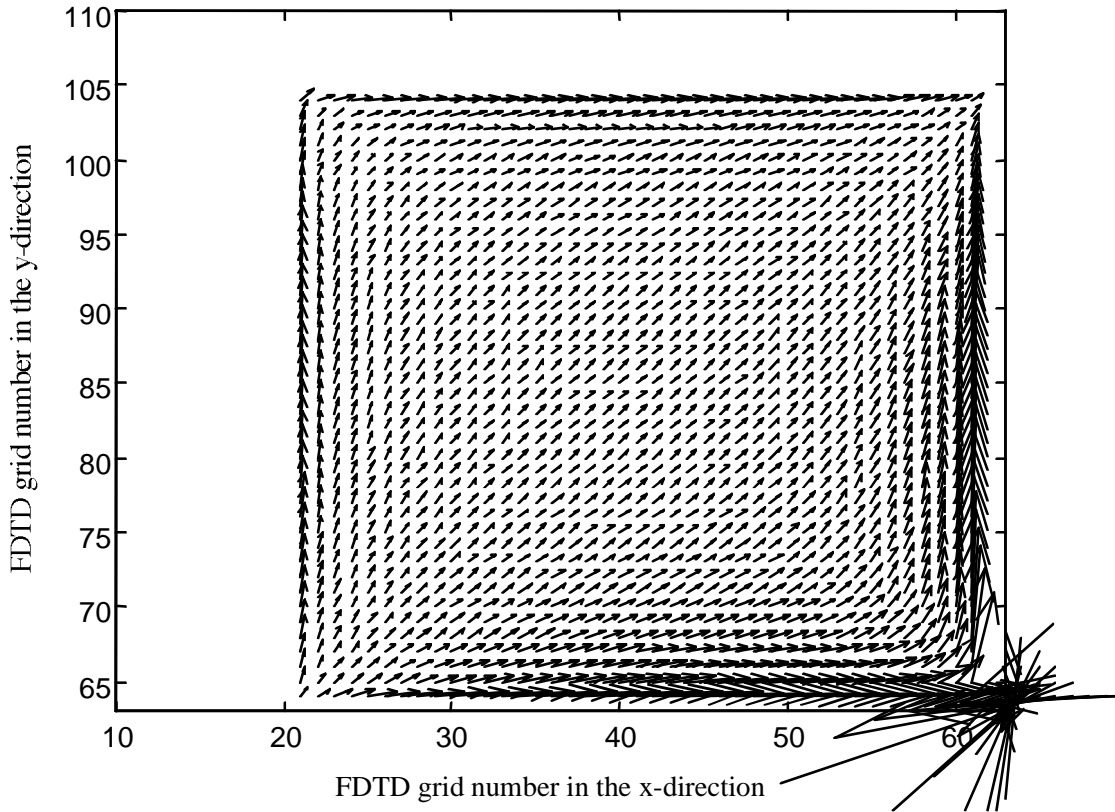
**Figure 5.19** Current distribution at 6 GHz on square #2 of the parasitic squares on the Foursquare antenna of Fig. 5.1.

The currents at the highest frequency of 7 GHz predominantly occupy the parasitic square; see Fig. 5.20. The currents on the diagonally excited squares are small everywhere except at the edges where they are coupling to the parasitic squares; see Fig. 5.21.



**Figure 5.20** Current distribution at 7 GHz on square #1 of the excited pair on the Foursquare antenna of Fig. 5.1.





**Figure 5.21** Current distribution at 7 GHz on square #2 of the parasitic squares on the Foursquare antenna of Fig. 5.1.

It may be difficult to say which part of the antenna is radiating simply from the current distribution. The far-field contribution of the current distribution on a square can be determined if an equivalent surface is placed around that square and the magnitude of the power radiating,  $P_i$ , in the  $0^\circ$  direction is calculated from the equivalent currents.  $P_i$  represents the power radiating from the  $i$ th square. Therefore, by placing the equivalent boundaries around each of the squares of the Foursquare antenna separately the percent contribution to the total radiation pattern in the  $0^\circ$  direction of the Foursquare antenna can be determined by

$$\%P_i = \frac{P_i}{P_1 + P_2 + P_3 + P_4} \text{ for } i = 1, 2, 3, 4 \quad (5.7)$$

The equivalent boundaries and far-fields are modeled using the FDTD code described in Chapter 4. Using this formulation, the dominant radiating squares at 4.5 GHz are the diagonally excited pair of squares, accounting for approximately  $\%P_1+\%P_3=95\%$  of the radiation. At 6.0 GHz the diagonally opposed squares account for approximately  $\%P_1+\%P_3=75\%$  of the radiation. At 7.25 GHz the radiation from the diagonally excited pair of squares is  $\%P_1+\%P_3=50\%$  and the other  $\%P_2+\%P_4=50\%$  is radiating from the parasitic elements. Thus, the Foursquare antenna radiates predominantly from the diagonally opposed square at the lower frequencies of operation. As frequency increases, the contribution to the far-field pattern from the parasitic squares increases.

The current distribution over the Foursquare antenna changes with frequency. The frequency dependence of current based on these calculated results is characteristic of frequency independent antennas. A simplified description of the current flow versus frequency shows that the radiating currents shift position on the antenna to approximate a resonant mode on the antenna at that frequency. The currents at the lower frequency of operation radiate from the diagonally excited squares, #1 and #3, of the Foursquare. As the frequency is increased to mid-band the current is distributed on the diagonally excited squares, #1 and #3, and the parasitic squares, #2 and #4. At the high frequency the currents mainly occupy the parasitic squares, #2 and #4, of the Foursquare. Similar to other broadband antennas, such as the log-periodic dipole array or spiral antennas, the Foursquare radiates from different region of the antenna depending on the frequency of excitation. This type of current redistribution with frequency is common in broadband antennas.

## CHARACTERISTICS OF STRONGLY COUPLED FINITE ARRAYS

Arrays with strong mutual coupling between elements are difficult to analyze. The active element pattern of an element in a strongly coupled array differs significantly from that of the isolated element. In addition to the pattern, the input impedance of an element is affected by coupling. The input impedance of an element in a fully active array is different from that of a single active element in an array, as used to find the active element pattern. The single active element impedance does not account for the contribution to input impedance from the coupled elements. The result of measuring the input impedance of a single active element can be seen in the simple transmission line model described in this chapter.

This chapter presents results of a numerical investigation of mutual coupling effects in arrays on patterns, impedance, resonant frequency and beam scanning angle. The resonant frequency of an element can shift significantly when used as an element in an array. This shift in resonant frequency is demonstrated with an example of a three element array of off set half-wave dipoles shown in Fig. 6.3. The dipoles are offset to allow for lower frequency modes of currents on the dipoles. Even when the dipoles are not off set from each other, as in a three element array of parallel half wave dipoles shown in Fig. 6.2, there is a significant change in the input impedance.

Strong mutual coupling in an array also causes the scanned beam direction to vary from the desired direction. A compensation technique that corrects for this variation is presented in this chapter. This compensation technique, to correct the pattern, is illustrated using the scanned three element array of Fig. 6.2 and the cardoid pattern of a strongly coupled two element array.

## 6.1 Active Element Pattern

Measuring the performance parameters of a large, fully active array requires complicated hardware because all the elements of the array require their own feed networks for simultaneous excitation. However, the fully active pattern can be obtained through superposition of the active element patterns. Active element patterns only require a single feed network. The active element pattern is found by exciting a single element in the array and match loading all other elements. In nearly all cases, the antenna elements are linear devices; therefore, superposition can be used to analyze the total antenna pattern. This is accomplished by exciting each element of the array one at a time and measuring the corresponding active element pattern. The superposition of the active element patterns gives the total far-field pattern as

$$F_{un}(\theta, \phi) = \sum_{n=1}^N g_{ae}^n(\theta, \phi) I_n e^{j\xi_n} \quad (6.1)$$

where  $I_n e^{j\xi_n}$  is the magnitude and relative phase of the element's excitation.  $g_{ae}^n(\theta, \phi)$  is the active element pattern of the  $n$ th element and it is found by exciting the element while terminating all other elements in the impedance of the generator,  $Z_g$ . This impedance,  $Z_g$ , does introduce a loss in the system that shows up as a decrease in the gain.

The active element pattern gives insight into where significant gain loss will appear when scanning the array. If there is a null in an active element pattern, the array when scanned to the angle at which the null occurs will have a loss in gain. The active element pattern of an element in an infinite array will be identical to all the other elements. Therefore, the far-field pattern given by (6.1) can be written as

$$F_{un}(\theta, \phi) = g_{ae}^n(\theta, \phi) \sum_{n=1}^N I_n e^{j\xi_n} \quad (6.2)$$

where the summation is the traditional array factor:

$$AF = \sum_{n=1}^N I_n e^{j\xi_n} \quad (6.3)$$

The far-field pattern given by (6.2) is found by pattern multiplication of the active element pattern and the array factor. Therefore, when an infinite array is scanned to the angle at which a null occurs in the active element pattern there will be a loss in gain from all the elements. This loss in element gain will result in a severe loss in gain for the fully excited array when scanned to this angle.

The gain of an element in a strongly coupled array can be significantly less than when the element is isolated due to the power lost in the generator impedance,  $Z_g$ . The power lost in  $Z_g$  for a single element excitation is given by

$$P_{mn} = \frac{1}{2} \operatorname{Re} \left( \frac{V_{mn}^2}{Z_g} \right). \quad (6.4)$$

where  $V_{mn}$  is the voltage induced at element  $m$  when element  $n$  is excited. In order to apply superposition, the total voltage,  $V_{t_m}$ , induced across  $Z_g$  is given as

$$V_{t_m} = \sum_{n=1}^N V_{mn} \quad (6.5)$$

The total power,  $P_{t_m}$  lost in element  $m$  for the fully excited array is given as

$$P_{t_m} = \frac{1}{2} \operatorname{Re} \left( \frac{V_{t_m}^2}{Z_g} \right). \quad (6.6)$$

The magnitude of  $V_{t_m}$  can be significantly less than the voltage induced from a single element excitation because of phase cancellation. Therefore, an increase or decrease in the lost power in the load resistance of element  $m$  is determined by the relative phasing of the  $V_{mn}$  voltages.

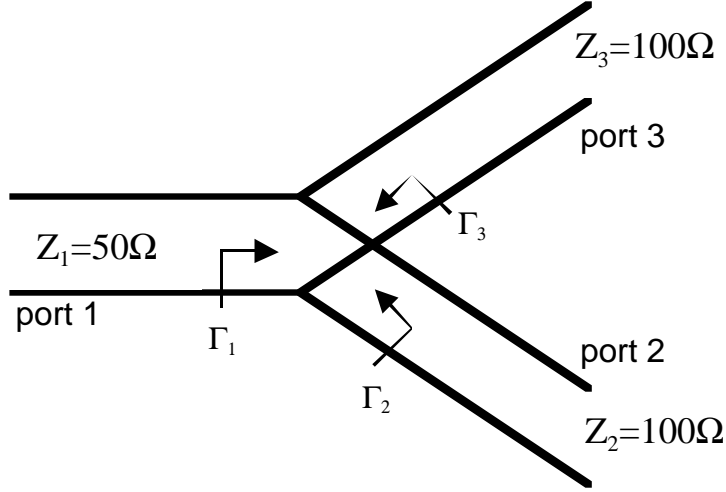
## 6.2 Power Loss in a Transmission Line Model

A two-element array has three ports through which power can be transferred. These ports are the ports of the two antennas and the third is free-space where power is radiated. This two-element array can be represented as a three port transmission line model as in Fig. 6.1. The two identical ports (ports 2 and 3) represent the antennas and the other port (port 1) represents power radiated. Using this simple three port transmission line model power loss can be demonstrated. By exciting ports 2 and 3 separately and then exciting them simultaneously, the difference in the percent power transmitted to the port representing radiation (port 1) can be calculated. For a transmitting array it is desired to have all the power transmitted from the two coupled antenna ports, ports 2 and 3, to the radiation port, port 1. By reciprocity, the a receiving array is desired to have all the power transmitted from the radiation port, port 1, to the two coupled antenna ports, port 2 and should have identical power loss. The power transmitted from one coupled antenna to the other or from port 2 to port 3 would result in a loss of power to the system.

Consider the junction of three transmission lines as shown in Fig. 6.1. The characteristic impedance of the first transmission line is  $Z_1=50\Omega$  and the other two are  $Z_2=Z_3=100\Omega$ . The reflection coefficient at the junction looking from port  $i$  is found from

$$\Gamma_i = \frac{Z_j \| Z_k - Z_i}{Z_j \| Z_k + Z_i} \quad (6.7)$$

where  $(i, j, k) = (1,2,3), (2,3,1)$  or  $(3,1,2)$ . At the junction,  $\Gamma_1 = 0.0$  and  $\Gamma_2=\Gamma_3=-0.5$ . The transmission coefficients can be found from the reflection coefficients as  $T_i=1+\Gamma_i$  where  $T_1=1.0$  and  $T_2=T_3=0.5$ .



**Figure 6.1** Transmission line model of radiation from a two element array. Port 1 represents the radiation port of the array. Ports 2 and 3 represent the antenna ports.

The normalized S-parameters of the system are found from the corresponding incident and reflected voltages,  $V_j^+$  and  $V_i^-$ , given by the reflection and transmission coefficients:

$$S_{ij} = \left. \frac{V_i^- / \sqrt{Z_i}}{V_j^+ / \sqrt{Z_j}} \right|_{V_k=0, \text{ for } k \neq j} \quad (6.8)$$

At port 1,  $S_{11}=0$  and  $S_{31}=S_{21}=0.7071$ . At port 2,  $S_{22}=-0.5$  and  $S_{32}=0.5$ . Assuming symmetry of the system, the remainder of the S-matrix can be filled to give

$$[b] = [S][a] \quad \text{or} \quad \begin{bmatrix} b_1^- \\ b_2^- \\ b_3^- \end{bmatrix} = \begin{bmatrix} 0 & 0.7071 & 0.7071 \\ 0.7071 & -0.5 & 0.5 \\ 0.7071 & 0.5 & -0.5 \end{bmatrix} \begin{bmatrix} a_1^+ \\ a_2^+ \\ a_3^+ \end{bmatrix} \quad (6.9)$$

First, the ports are excited separately to give the  $a$  vectors for the separate excitations for ports 1, 2 and 3 respectively as

$$a_1 = \begin{bmatrix} \sqrt{2} \\ 0 \\ 0 \end{bmatrix}, a_2 = \begin{bmatrix} 0 \\ \sqrt{2} \\ 0 \end{bmatrix}, a_3 = \begin{bmatrix} 0 \\ 0 \\ \sqrt{2} \end{bmatrix} \quad (6.10)$$

Substituting into (6.9) gives the corresponding  $b$  vectors for ports 1, 2 and 3, respectively, as

$$b_1 = \begin{bmatrix} 0 \\ 1 \\ 1 \end{bmatrix}, b_2 = \begin{bmatrix} 1 \\ -0.707 \\ 0.707 \end{bmatrix}, b_3 = \begin{bmatrix} 1 \\ 0.707 \\ -0.707 \end{bmatrix} \quad (6.11)$$

The power received at each port  $i$  is found from  $P_i^r = \frac{1}{2}b_i^2$  and the power transmitted from each port  $i$  is found from  $P_i^t = \frac{1}{2}a_i^2$  where the vector of power received,  $P^r$ , at the three ports with an excitation of ports 1, 2 and 3, respectively, are given by

$$P_1^r = \begin{bmatrix} 0 \\ 0.5 \\ 0.5 \end{bmatrix}, P_2^r = \begin{bmatrix} 0.5 \\ 0.25 \\ 0.25 \end{bmatrix}, P_3^r = \begin{bmatrix} 0.5 \\ 0.25 \\ 0.25 \end{bmatrix} \quad \text{W} \quad (6.12)$$

And the vector of power transmitted,  $P^t$ , from each of the three ports 1, 2 and 3 is given by

$$P_1^t = \begin{bmatrix} 1 \\ 0 \\ 0 \end{bmatrix}, P_2^t = \begin{bmatrix} 0 \\ 1 \\ 0 \end{bmatrix}, P_3^t = \begin{bmatrix} 0 \\ 0 \\ 1 \end{bmatrix} \quad \text{W} \quad (6.13)$$

Therefore, when port 1 is excited half the power goes to port 2 and the other half goes to port 3, as given by  $P_1^r$ . Since it is desired to transmit from port 1 to port 2 and port 3, the resulting efficiency,  $e=P^r/P^t$ , is 100%. However, if port 2 is excited, half the power goes to port 1, a quarter is reflected back down port 2 and another a quarter is transmitted to



port 3 as given by  $P_2^r$ , resulting in a 50% efficiency if it is desired to transmit from port 2 to port 1. The same can be said for exciting port 3 due to symmetry.

Now, consider exciting ports 2 and 3 simultaneously. The  $a$  and  $b$  vectors become

$$a = \begin{bmatrix} 0 \\ 1 \\ 1 \end{bmatrix}, \quad b = \begin{bmatrix} 1.414 \\ 0 \\ 0 \end{bmatrix} \quad (6.14)$$

The corresponding transmit and receive power vectors are

$$P^t = \begin{bmatrix} 0 \\ 0.5 \\ 0.5 \end{bmatrix}, \quad P^r = \begin{bmatrix} 1 \\ 0 \\ 0 \end{bmatrix} \text{ W} \quad (6.15)$$

representing that all the power is transmitted to port 1. Therefore, when both ports 2 and 3, which represent the coupled antennas, are excited simultaneously, the power transmitted to the radiation port, port 1, is 100%. However if ports 2 or 3 are excited separately, only 50% of the power is transmitted to port 1.

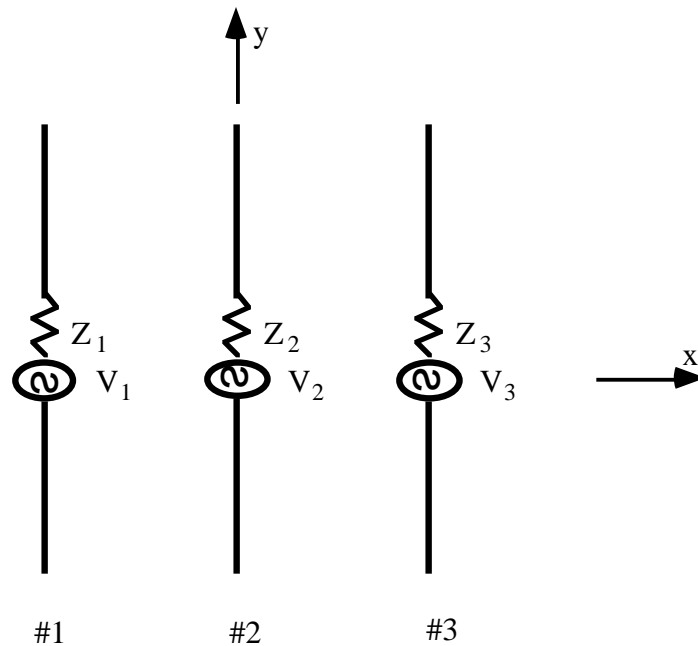
### 6.3 An Array of Three Half-Wave Dipoles

Mutual coupling effects on power and efficiency are illustrated in this section using an array of three parallel half-wave dipoles spaced a quarter wave apart as shown in Fig. 6.2. The transmission line model in the previous section is used to find the power distribution in an array of two antennas represented by the two identical ports and the third port is the power radiated. This same theory of power distribution can be shown by modeling a three element array of antennas using the Method of Moments formulated in the WIRE code [31]. A three element array is chosen because the input impedance of the center element has a different impedance environment from that of the two outer elements. Therefore, the three element array is a more general model than the two element array.

The three elements are parallel half-wave dipoles spaced  $1/4 \lambda$  apart to produce strong mutual coupling; see Fig. 6.2. Each element of the array has an impedance  $Z_1=Z_2=Z_3=75\Omega$  placed in series with a ideal voltage generator  $V_1, V_2$  and  $V_3$ . The power dissipated in the impedances,  $Z_1, Z_2$  and  $Z_3$ , can be found from

$$P_i = \frac{1}{2} I_i^2 Z_i \text{ for } i = 1, 2, 3 \quad (6.16)$$

First, the center element is excited using a generator of  $V_2 = 1\angle 0^\circ$  while the other two sources are turned off,  $V_1 = V_3 = 0\angle 0^\circ$ . The power dissipated in each of the resistances,  $Z_1, Z_2$  and  $Z_3$ , is calculated from (6.16) to be  $P_1=2.08 \times 10^{-4} \text{W}$ ,  $P_2=1.451 \times 10^{-3} \text{W}$ , and  $P_3=2.08 \times 10^{-4} \text{W}$ . The total power lost to impedance is  $P_L=P_1+P_2+P_3=1.867 \times 10^{-3} \text{W}$ . The total power delivered to the system, as calculated from the Method of Moments code, is  $P_T=2.518 \times 10^{-3} \text{W}$ . This gives an efficiency of  $e=(P_T-P_L)/P_T=P^r/P^t=25.9\%$ .



**Figure 6.2** Array of 3 parallel half-wave dipoles

Next, we examine the case where all three elements of the array, as shown in Fig. 6.2, have a generator voltage of  $V_1 = V_2 = V_3 = 1\angle 0^\circ$ . The power dissipated in impedance,  $Z_1$ ,  $Z_2$  and  $Z_3$ , is calculated to be  $P_1=7.77\times 10^{-4}\text{W}$ ,  $P_2=2.68\times 10^{-4}\text{W}$  and  $P_3=7.77\times 10^{-4}\text{W}$ . The total power lost to impedance is  $P_L=P_1+P_2+P_3=1.82\times 10^{-3}\text{W}$ . The total power delivered to the system, as calculated from the Method of Moments code, is  $P_T=5.839\times 10^{-3}\text{W}$ . This gives an efficiency  $e=69\%$ .

The efficiency of the single center element excited in this example array is 25.9% and is much lower than the efficiency of 69% when the entire array is excited. Therefore, exciting a single element in an array does not give valid information about the efficiency of the fully excited array. The gain of an antenna is found from

$$G = eD \tag{6.17}$$

where  $D$  is the directivity and gain,  $G$ , is a function of efficiency,  $e$ . Therefore, if the efficiency,  $e$ , cannot be determined from the excitation of a single element in an array, the gain of the fully excited antenna cannot be inferred from this measurement.

### 6.3.1 Input Impedance

The input impedance of an array element depends on the level of mutual coupling with the other array elements. The impedance of the transmission line must match the element input impedance to reduce the mismatch loss. Therefore, the desired impedance of the transmission line depends on the input impedance of the attached antenna element operating in the array. In a tightly coupled array, the input impedance of the element will not be the same as the input impedance of the single isolated element. This change in impedance will be shown with an array of three parallel dipoles. The desired impedance of the transmission line is that which gives the maximum power delivered to the antenna when the entire array is excited. In addition, the array coupling can also change the resonant frequency of the element in an array. This frequency shift will be demonstrated with an off-set array of three dipoles.

The active element pattern is measured with all elements terminated in an impedance equal to that of the generator,  $Z_g$ , to be connected to the elements of the fully excited

array. Measuring the impedance of a single active element would not take into consideration the coupling from the other antennas in the array when the array is fully excited. Therefore, the active element impedance does not give enough information to determine the fully active input impedance of the antenna. However, there are other methods for determining the fully active input impedance of an element in an array.

The input impedance of an element is the ratio of input voltage to input current. In an array this definition implies that the input impedance of an element is the total voltage divided by the total current of the fully excited array. However, in measurements it is not always feasible to excite an entire array at once to measure the input impedance. For the three element array model of Fig. 6.2, the total current at a single element can be found by exciting each element separately with  $V_1$ ,  $V_2$  or  $V_3=1\angle 0^\circ$  V excitation while the other elements are shorted by setting  $Z_i=0$ . Therefore, the induced currents on each antenna due to the excitation of each of the three antennas can be determined. The three element array of Fig.6.2 was modeled using the Method of Moments. The induced currents  $I_{mn}$  are given by

$$I_{mn} = \begin{bmatrix} 6.872 - j5.408 & 1.876 + j5.558 & 0.134 - j0.722 \\ 1.876 + j5.558 & 3.218 - j5.678 & 1.876 + j5.558 \\ 0.134 - j0.722 & 1.876 + j5.558 & 6.872 - j5.408 \end{bmatrix} \times 10^{-3} \text{ A} \quad (6.18)$$

where  $m$  is the excited element and the current is measured on element  $n$ . The sum of the three currents induced on each antenna due to each of the other three antennas gives the total current. Therefore the total current induced on element  $n$  can be found by summing the values in row  $n$  of  $I_{mn}$  in (6.18).

$$I_n^t = \sum_{n=1}^3 I_{nm} \quad (6.19)$$

Substituting  $I_{mn}$  into (6.19) gives the total current  $I_n^t$  as

$$I_n' = \begin{bmatrix} 8.882 - j0.572 \\ 6.970 + 5.438 \\ 8.882 - j0.572 \end{bmatrix} \times 10^{-3} \text{ A} \quad (6.20)$$

Since the voltage used to excite each element is  $1\angle 0^\circ \text{V}$ , then the input impedance, which is the impressed voltage,  $V^i$ , divided by the total current,  $I'$ , is the inverse of the values of the total current vector of (6.20). Therefore, the input impedance is

$$Z = \begin{bmatrix} 112.1 + j7.22 \\ 89.18 - j69.58 \\ 112.1 + j7.22 \end{bmatrix} \Omega \quad (6.21)$$

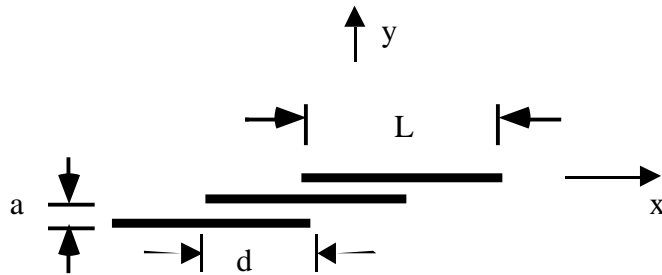
To test the validity of the calculated input impedance, each element of the array was terminated with the calculated input impedance. If the input impedance values are correct, the power dissipated in the resistances is 50% of the total power dissipated in the array. For this example, the total power dissipated in the system is given by the Method of Moments code as 6.184 mW. The power dissipated in each resistance is found from (6.16) as

$$P_d = \begin{bmatrix} 1.11 \\ 0.871 \\ 1.11 \end{bmatrix} \text{ mW} \quad (6.22)$$

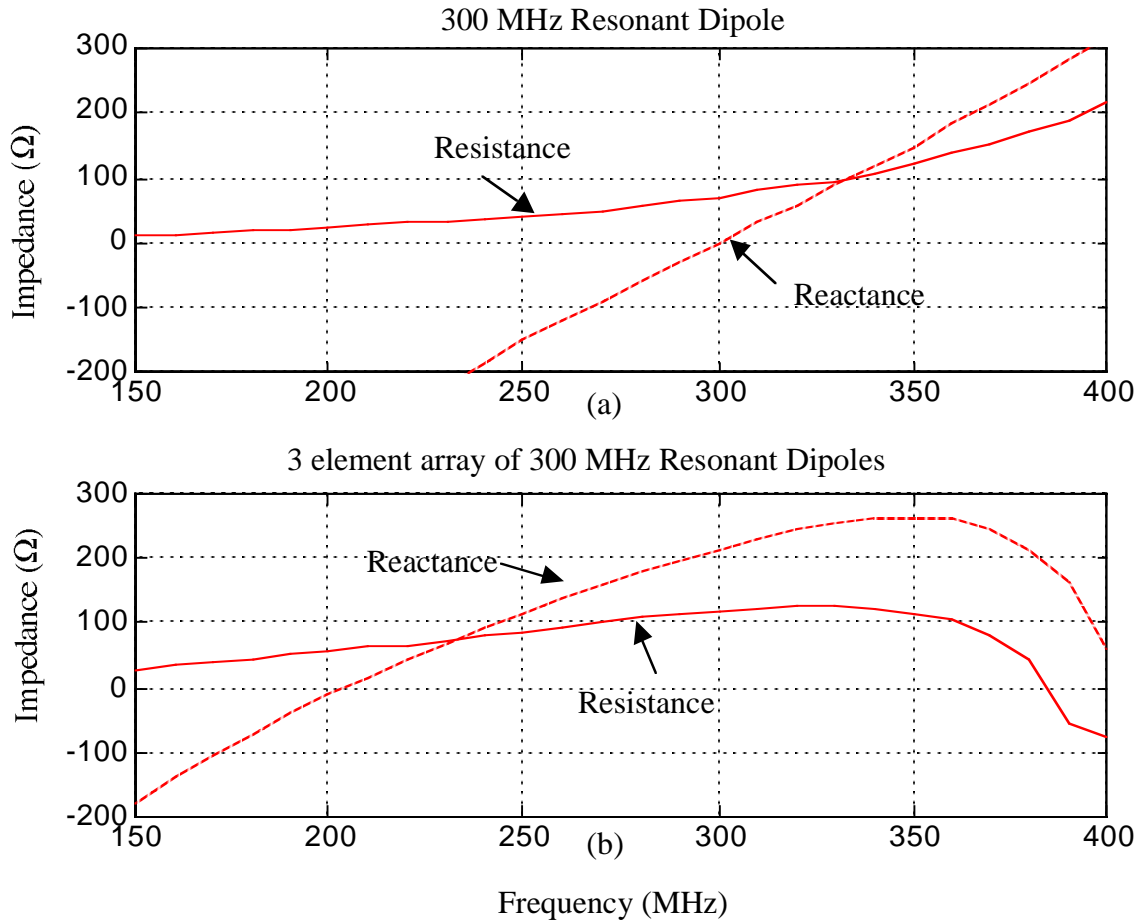
The total power dissipated in the three resistances is 3.092 mW or 50% of the power dissipated in the entire system. A 50% power loss is consistent with the power loss to a single antenna terminated in its input impedance.

Not only can the input impedance of an antenna change due to strong coupling in an array, the resonant frequency of the antenna can also shift significantly. In an array the resonant frequency can be significantly lower than that of the single isolated element. The amount of frequency shift depends on the strength of the mutual coupling. To show this shift in frequency response, the input impedance of an array of three tightly spaced

resonant dipoles as shown in Fig. 6.3 was modeled using the Method of Moments. The computed input impedance is shown in Fig.6.4 for frequencies from 150 MHz to 400 MHz. The isolated antenna element is resonant at 300 MHz. The three element array is resonant at 200 MHz which is a significant shift from the resonant frequency of the single element.



**Figure 6.3** Tightly spaced 3 element offset array of 300 MHz resonant dipoles ( $L=0.479\text{m}$ ,  $a=.005\text{m}$  and  $d=0.25\text{m}$ ).



**Figure 6.4** Calculated input impedance for: (a) a single 300 MHz resonant dipole and (b) the 3 element array of 300 MHz resonant dipoles shown in Fig. 6.3.

### 6.3.2 Scanning a Parallel Dipole Array

A finite array of strongly coupled elements introduces mutual coupling which affects the array performance. The required voltage phase taper to scan the beam to the desired pointing angle is much larger than expected. However, the larger the array, the more predictable the scanning due to the increased uniformity of the active element pattern and input impedance. There are compensation techniques that determine the necessary voltage phase taper that yields the desired current phase taper [32]. These techniques are most effective when the elements of the array have a single mode of operation. Furthermore, the input impedance to the elements in the array will vary with scan angle.

The variation in the input impedance with scan angle will increase with increased levels of mutual coupling.

Variations in the array element characteristics with mutual coupling are demonstrated using a small array of dipoles. Consider a three element array of  $1/4 \lambda$  spaced  $1/2 \lambda$  parallel dipoles shown in Fig. 6.2. The close element spacing in the array creates strong mutual coupling. The array is modeled using the method of moments. The inter element phase shift  $\alpha$  is found from the spacing  $d$  and  $\theta_0$  as

$$\alpha = -\beta d \sin(\theta_0) \quad (6.23)$$

The inter element phase shifts,  $\alpha$ , for

$$\theta_0 = \begin{bmatrix} 10^\circ \\ 20^\circ \\ 30^\circ \\ 40^\circ \end{bmatrix} \text{ are } \alpha = \begin{bmatrix} 15.63^\circ \\ 30.78^\circ \\ 45.00^\circ \\ 57.85^\circ \end{bmatrix} \quad (6.24)$$

The maximum pattern locations calculated using the Method of Moments were found to be  $7^\circ$ ,  $15^\circ$ ,  $25^\circ$  and  $35^\circ$  for desired pointing angles of  $10^\circ$ ,  $20^\circ$ ,  $30^\circ$  and  $40^\circ$ .

Now consider a five element array of  $1/4 \lambda$  spaced parallel half wave dipoles. For the same four scan angles, the maximum of the pattern angles were found to be  $9^\circ$ ,  $18^\circ$ ,  $27^\circ$  and  $36^\circ$  which are closer to the desired scan angles of  $10^\circ$ ,  $20^\circ$ ,  $30^\circ$  and  $40^\circ$ . The outer elements, which have the greatest impedance variation, are less significant contributors to the radiation pattern for larger arrays. Therefore, as the size of the array is increased the pattern maximum is closer to the desired angle without using compensation techniques.

If the three element dipole array of Fig 6.2 had the desired current phase taper, the beam would have the correct pointing angle. The current phase taper differs from the voltage phase taper due to the mutual coupling. The mutual coupling causes an impedance environment that varies depending on the element's position in an array.



Therefore, a phase tapered voltage excitation will not produce the same phase taper for the currents induced on the antennas. However, a mutual coupling compensation technique can be used to determine the required excitation voltage to achieve the desired current phase taper.

The required voltage excitations that give the desired current phases are found by first determining the admittance matrix,  $Y$ , of the array where the admittance  $Y_{mn}$  can be found from

$$Y_{mn} = \frac{I_m}{V_n} \quad (6.25)$$

where  $I_m$  is the short circuit current at the input to antenna  $m$  and  $V_n$  is the voltage at terminal  $n$ .

$$Y = \begin{bmatrix} 6.872 - j5.408 & 1.876 + j5.558 & 0.134 - j0.722 \\ 1.876 + j5.558 & 3.218 - j5.678 & 1.876 + j5.558 \\ 0.134 - j0.722 & 1.876 + j5.558 & 6.872 - j5.408 \end{bmatrix} \times 10^{-3} \text{ S} \quad (6.26)$$

The impedance matrix,  $Z$ , is the inverse of the admittance matrix,  $Y$ :

$$Z = \begin{bmatrix} 79.5342 + j38.2919 & 40.0721 - j35.3559 & -20.4926 - j31.2816 \\ 40.0721 - j35.3559 & 76.1926 + j37.2394 & 40.0721 - j35.3559 \\ -20.4926 - j31.2816 & 40.0721 - j35.3559 & 79.5342 + j38.2919 \end{bmatrix} \Omega \quad (6.27)$$

The voltage excitation for equal amplitude and phase currents can be found from the impedance matrix,  $Z$ , and the desired current excitation  $I$  as

$$V = ZI \quad (6.28)$$

For  $\theta_0=0^\circ$  the desired current excitation would be

$$I = \begin{bmatrix} 1 \\ 1 \\ 1 \end{bmatrix} \text{ A} \quad (6.29)$$

The excitation voltage is found by substituting (6.27) and (6.29) into (6.28) to give

$$V = \begin{bmatrix} 99.11 - j28.35 \\ 156.34 - j33.47 \\ 99.11 - j28.35 \end{bmatrix} \text{ V} \quad (6.30)$$

The current excitation for  $\theta_0=30^\circ$  is

$$I = \begin{bmatrix} 0.707 + j0.707 \\ 0.0 + j1.0 \\ -0.707 + j0.707 \end{bmatrix} \text{ A} \quad (6.31)$$

and the required voltage excitation is

$$V = \begin{bmatrix} 1.0112 + j1.3100 \\ 0.1275 + j1.3285 \\ -0.4032 + j0.3263 \end{bmatrix} \times 10^2 \text{ V} \quad (6.32)$$

The Method of Moments model of the array with excitation voltages from (6.32) give a beam maximum at  $\theta_0=32^\circ$ . The beam is off by  $2^\circ$  from the desired pointing angle of  $30^\circ$ . Exceeding the specified angle is to be expected in an array with a broad element pattern and few elements. It is important to note that this method of compensation can be modified to use with any linear parameters that fully describe the mutual coupling between the elements of the array such as  $S$ -parameters.

When the beam is scanned, mutual coupling will also cause the input impedance of the elements of the array to change from that of the  $\theta_0=0^\circ$  example. However, the input impedance for  $\theta_0=0^\circ$  and  $\theta_0=30^\circ$  is found from

$$z_n = \frac{V_n}{I_n} \quad (6.33)$$

Therefore by substituting (6.29) and (6.30) into (6.33) gives input impedance,  $z$ , for  $\theta_0=0^\circ$ .

$$z = \begin{bmatrix} 99.11 - j28.35 \\ 156.34 - j33.47 \\ 99.11 - j28.35 \end{bmatrix} \Omega \quad (6.34)$$

and by substituting (6.31) and (6.32) into (6.33) the input impedance,  $z$ , for  $\theta_0=30^\circ$

$$z = \begin{bmatrix} 1.64 + j0.21 \\ 1.33 - j0.128 \\ -0.32 + 0.21 \end{bmatrix} \times 10^2 \Omega \quad (6.35)$$

#### 6.4 Pattern Compensation Example Using a Cardioid Pattern

The current compensation method can also be used to correct the distorted cardioid pattern formed by exciting the two dipoles separated by  $\lambda/4$  with voltage excitations that are  $90^\circ$  out of phase. Simple array theory says that a cardioid pattern can be formed by two elements  $\lambda/4$  apart where one is  $90^\circ$  out of phase with the other. However the currents must be  $90^\circ$  out of phase and in most situations the antenna is excited with a voltage source. The input impedances of the two antennas are not the same because of the effects of mutual coupling. Therefore, the currents do not have the same relative phase shift as the voltage excitation and will not correctly form the cardioid pattern. To solve for the voltage excitation that gives the correct current excitation, first find the admittance matrix of the two element array using (6.25) as.

$$Y = \begin{bmatrix} 1.245 \times 10^{-2} - j6.278 \times 10^{-3} & -3.741 \times 10^{-3} + j9.036 \times 10^{-3} \\ -3.741 \times 10^{-3} + j9.036 \times 10^{-3} & 1.245 \times 10^{-2} - j6.278 \times 10^{-3} \end{bmatrix} \text{ S} \quad (6.36)$$

Therefore, the impedance matrix is  $Z=1/Y$  which gives

$$Z = \begin{bmatrix} 68.23 - j0.987 & 35.63 - j31.72 \\ 35.63 - j31.72 & 68.23 - j0.987 \end{bmatrix} \Omega \quad (6.37)$$

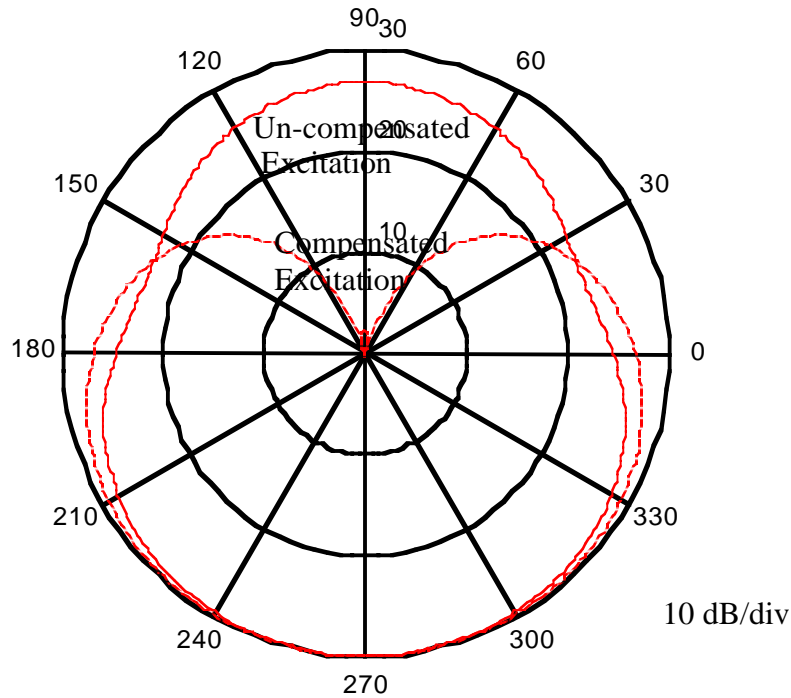
The desired currents for proper excitation are

$$I = \begin{bmatrix} 1 \\ j1 \end{bmatrix} \text{ A} \quad (6.38)$$

The input voltage for the given the desired currents can be found from  $V=ZI$  where  $V$  is

$$V = \begin{bmatrix} 99.95 + j34.65 \\ 36.62 + j36.51 \end{bmatrix} \text{ V} \quad (6.39)$$

By applying these voltages to the input of the two dipoles, the cardioid pattern can be formed as shown in Fig. 6.5.



**Figure 6.5** Normalized cardioid pattern formed from two parallel resonant dipoles  $\lambda/4$  apart with compensated voltages compared to the normalized pattern without compensation.

## 6.5 Summary

The characteristics of an isolated antenna element can vary greatly from that of the element in a strongly coupled array. This chapter demonstrated the effect that mutual coupling has on the characteristics of antennas such as the input impedance, far-field pattern, resonant frequency and beam scanning.

The three element array of off-set half wave dipoles shown in Fig. 6.3 demonstrates a shift in the resonant frequency when an element is placed in an array. For this array configuration the resonant frequency shifted from 300 MHz to 200 MHz. The three element array of parallel dipoles shown in Fig. 6.2 demonstrated that the input impedance of an isolated element varies from that of the element in a fully active array. When this same parallel dipole array is scanned the pointing angle is less than expected due to the mutual coupling. Compensation techniques are effective in producing the desired pointing angle because the dipoles have only a single mode of excitation.

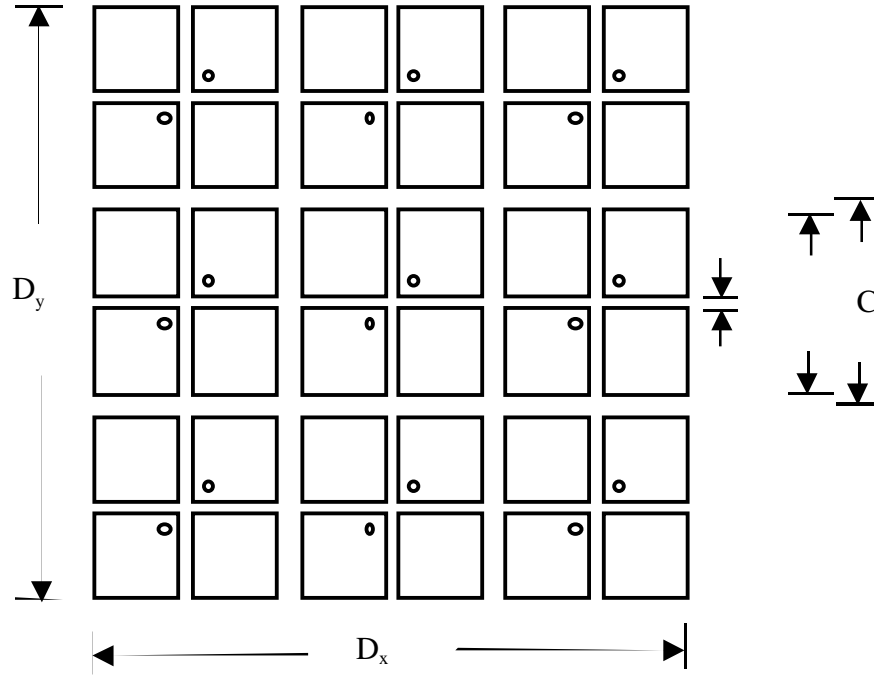
Compensation techniques were also effective in producing a cardioid pattern with two strongly coupled dipoles.

## **THE FOURSQUARE AS A FINITE ARRAY ELEMENT**

The properties of isolated elements can change dramatically when placed in an array. The most obvious change is the element pattern. When a single element is excited in an array, the resulting pattern is the active element pattern. The active element pattern varies from that of the isolated element pattern due to mutual coupling between elements in the array. Pozar predicts scan blindness through coupling of Floquet modes to surface wave modes on the substrate [33]. Pozar later described the active element pattern relations in terms of scattering parameters in order to predict the scan performance of an array [34]. The input impedance of an antenna also changes when implemented as an element in an array. Depending on the level of mutual coupling the impedance can vary greatly from that of the isolated element. Pozar and Allen modeled an infinite array of printed dipoles to demonstrate the change in array impedance versus scan angle [33],[35]. Pozar also modeled the impedance and active element pattern of a finite array of printed dipoles [36]. Edelberg et al. modeled a two-dimensional array of slots fed by waveguides as a periodic structure to analyze the impedance properties of a large antenna array [37]. This chapter describes the effect of mutual coupling on input impedance and the array pattern for the Foursquare antenna as an element.

The effects of mutual coupling on the Foursquare antenna are studied by modeling the finite 3x3 array shown in Fig. 7.1. The array was modeled using the FDTD program described in Chapter 4. The effects of mutual coupling can be seen by calculating the input impedance and the active element pattern of the center element. However, variations in the input impedance and the far-field pattern from that of the isolated Foursquare element do not affect gain of the fully excited array. However the mutual

coupling will affect the scanned patterns of the array. The scanned patterns are shown for a true time delay (TTD) phased excitation.



**Figure 7.1** 3x3 array of Foursquare elements

### 7.1 Far-field Patterns of a 3x3 Foursquare Array

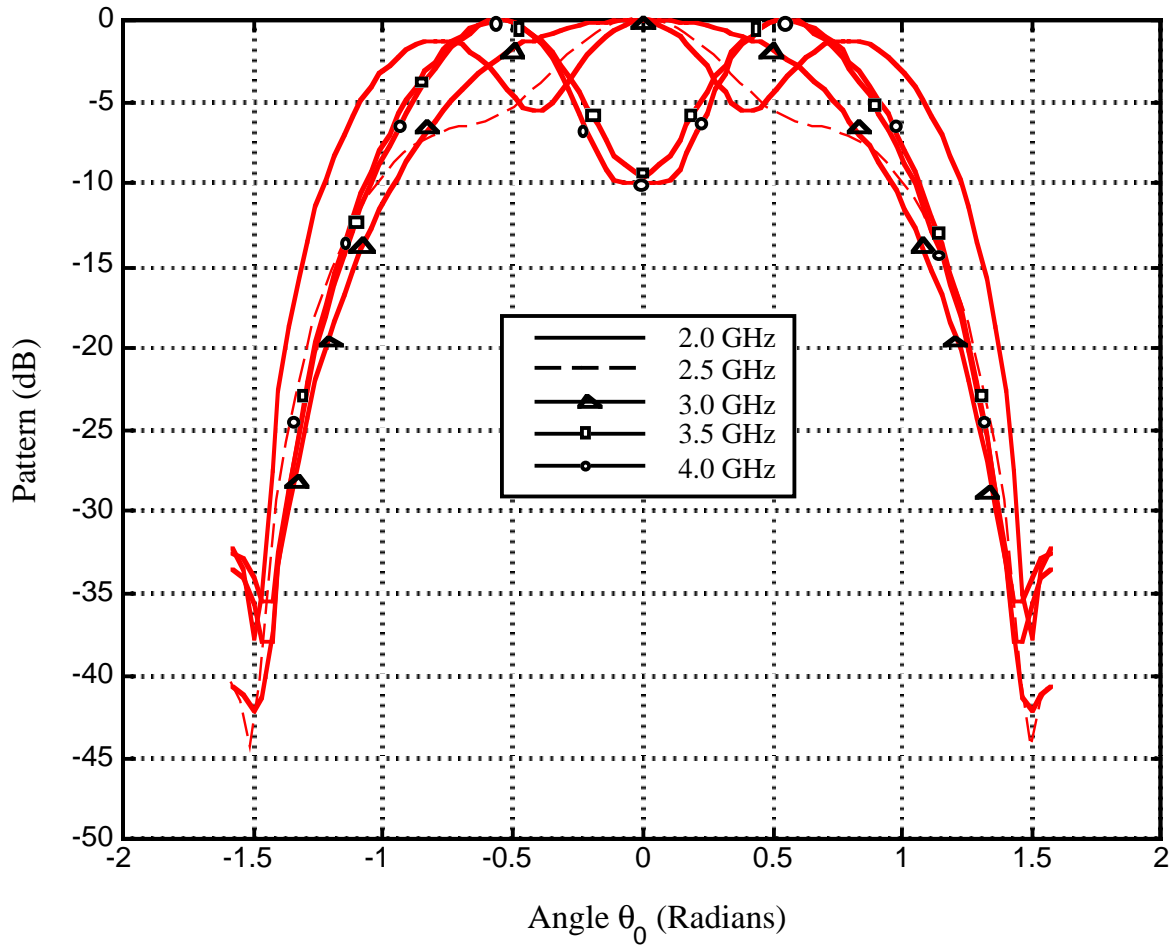
The 3x3 Foursquare array geometry, shown in Fig. 7.1, is summarized in Table 7.1. The array is placed a height  $h=0.5''$  above a ground plane. The Foursquare elements are placed in a uniform square grid with a cell length of  $C=1.513''$ . The length along each side of the Foursquare element is  $L=1.478''$ .



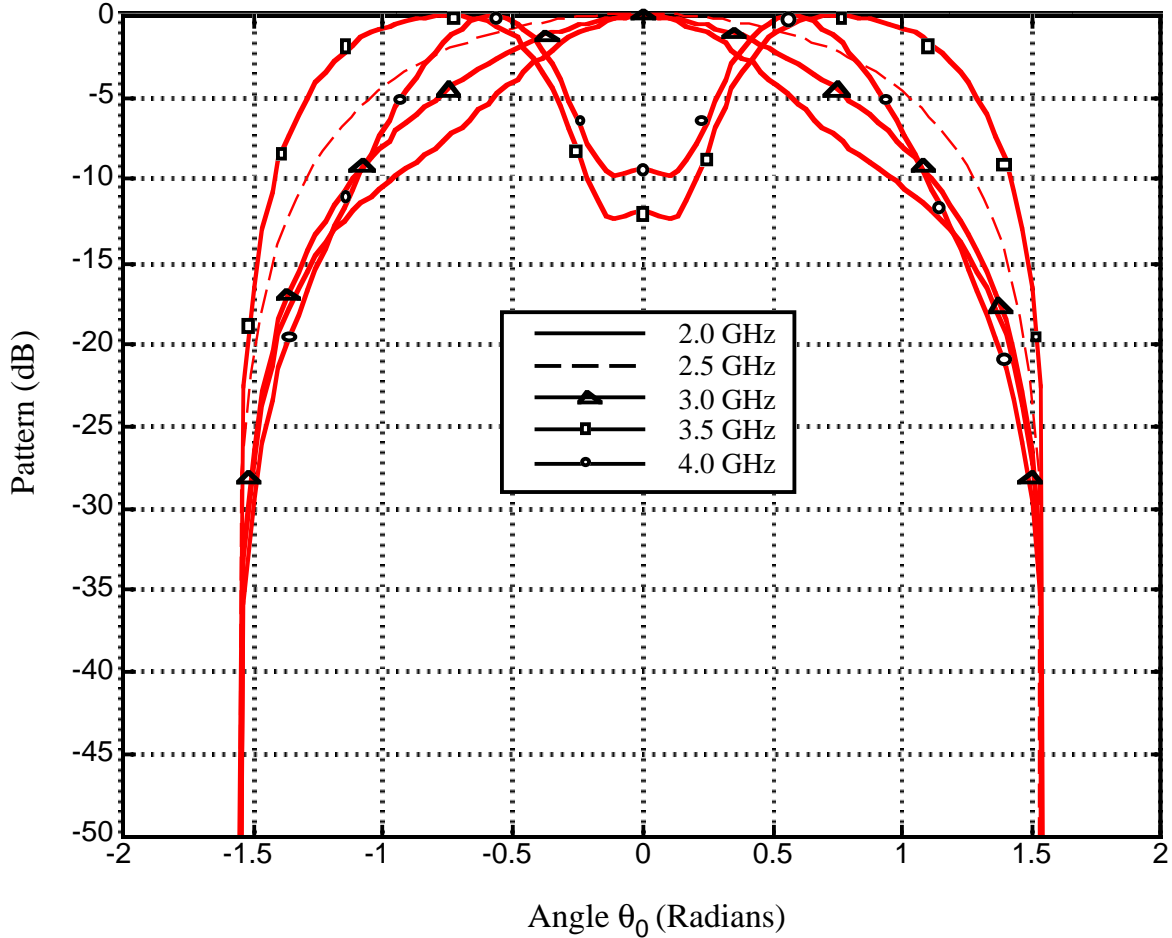
**Table 7.1** 3x3 Foursquare array geometry

Parameter	Symbol	Value mm	Value inches
Substrate Thickness	$t_s$	0.71	0.028
Distance from ground plane	$t_d$	12.7	0.5
Side Length of Foursquare	L	37.5	1.478
Side Length, Including Distance Between Elements	C	38.4	1.513
Spacing Between Squares	W	0.51	0.02
Relative Dielectric Constant	$\epsilon_r$	2.33	2.33

The E- and H-plane active element patterns of the center element in the 3x3 Foursquare array were calculated using the FDTD code for frequencies from 2.0-4.0 GHz and are shown in Fig. 7.2 and Fig. 7.3. The active element pattern of the 3x3 Foursquare array has nulls at  $0^\circ$  for the 3.5 and 4.0 GHz patterns in both the E- and H-plane. At all frequencies, the patterns are significantly different from that of the isolated Foursquare element patterns of Fig. 5.7 through Fig. 5.12.



**Figure 7.2** Calculated E-plane active element patterns for center element of the 3x3 Foursquare array of Fig. 7.1 for frequencies from 2.0-4.0 GHz.



**Figure 7.3** Calculated H-plane active element patterns for center element of the 3x3 Foursquare array of Fig. 7.1 for frequencies from 2.0-4.0 GHz.

The fully active array pattern for the E- and H- plane is also calculated using the FDTD code as shown in Fig. 7.4 and Fig. 7.5. When fully excited, the far-field pattern has a maximum at  $0^\circ$  and sidelobe levels below 20 dB; see Fig. 7.4. The fully excited array is radiating from all the elements of the array. The edge elements of the array do not have the same active element pattern as the center element. The fully active array pattern is the sum of these active element patterns, which fill in the null at  $0^\circ$ .

It is desirable to perform an independent evaluation of the array pattern as a check on the FDTD code. This can be done using an approximate beamwidth formula. This

approximation is derived from the predicted directivity for an aperture of this size the directivity

$$D = \frac{4\pi}{\lambda^2} A \quad (7.1)$$

where A is the aperture area. Next, beamwidth is related to directivity using [28].

$$D = \frac{26,000}{HP_{E^\circ} HP_{H^\circ}} = \frac{26,000}{HP^{\circ 2}} \quad (7.2)$$

since  $HP_{E^\circ}$  and  $HP_{H^\circ}$  are the half power beamwidths in the E- and H-plane and  $HP_{E^\circ} = HP_{H^\circ} = HP^\circ$  for this square array. Rearranging this equation to find the beamwidth:

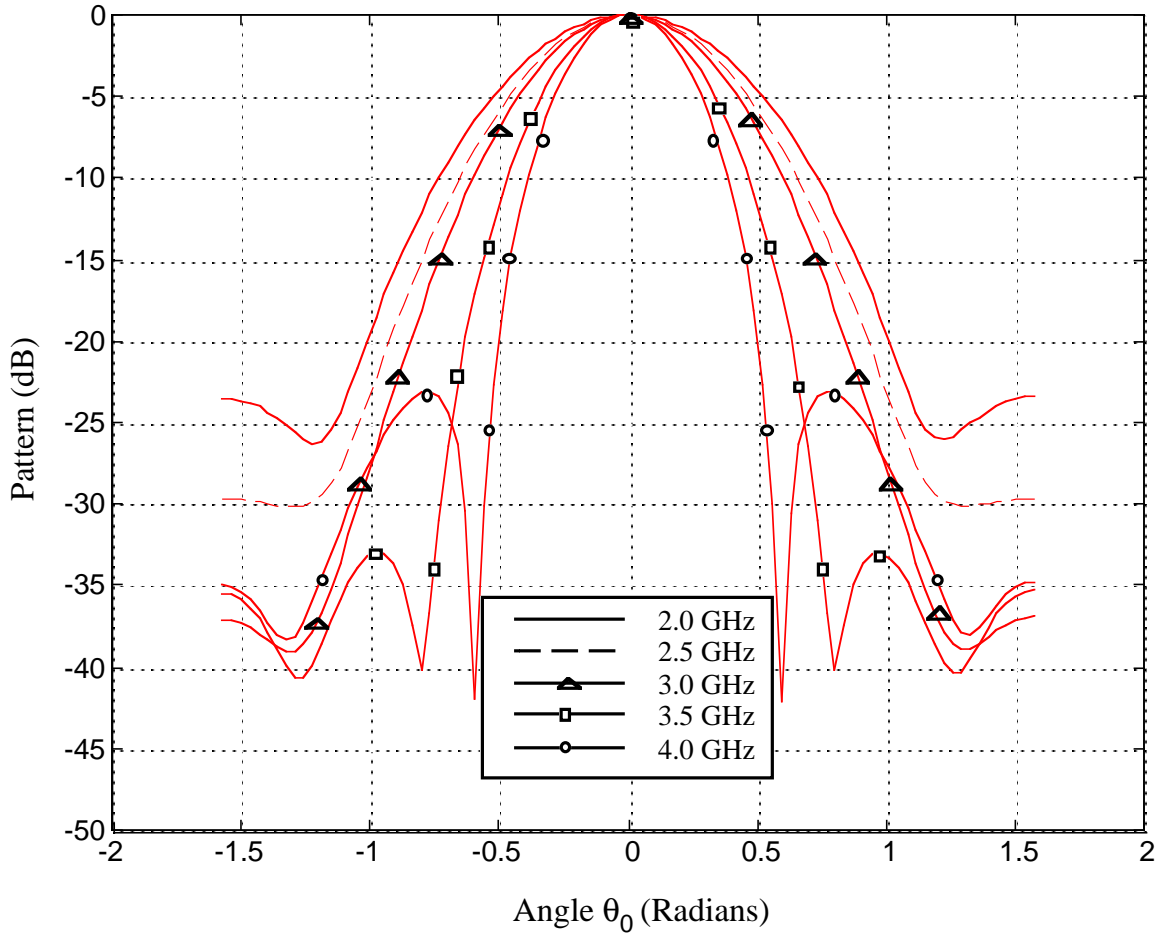
$$HP^\circ = \sqrt{\frac{26,000}{D}} \quad (7.3)$$

This can then be used with (7.1) to find  $HP^\circ$  for the array with dimensions  $D_x = D_y = 0.115\text{m}$ , from Fig. 7.1, which yields an array area of  $A = D_x D_y = 0.013\text{m}^2$ . The directivity, D, at 2.0 GHz and 4.0 GHz found from (7.1) is 8.7 dB and 14.7 dB. At 2.0 GHz, the half power beamwidth found from (7.3) using the directivity value of 8.7 dB is  $HP^\circ = 60^\circ$ . At 4 GHz, the half power beamwidth found from (7.3) using the directivity value of 14.7 dB is  $HP^\circ = 30^\circ$ . These beamwidths should be close to the values found from the FDTD simulated pattern if the mutual coupling is not causing distortions in the pattern.

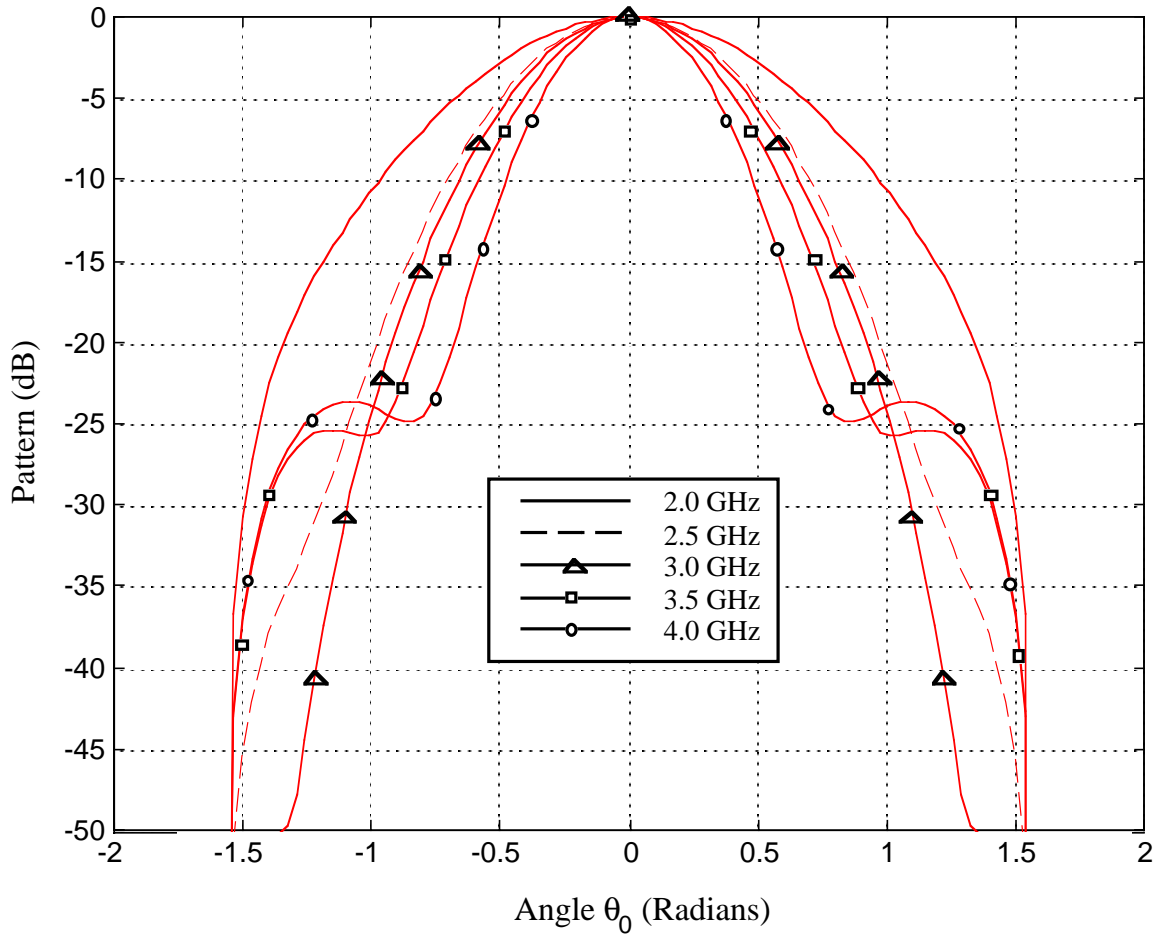
The E- and H-plane array patterns, calculated using the FDTD code, shown in Fig. 7.4 and Fig. 7.5 have beamwidths of  $52^\circ$  and  $58^\circ$ , respectively, at 2 GHz and  $29^\circ$  and  $32^\circ$ , respectively, at 4 GHz. These beamwidths are very close to the approximation for half

power beamwidth found from (7.3) as  $60^\circ$  and  $30^\circ$  for a 2.0 and 4.0 GHz excitation respectively.

The active element patterns are significantly different from those of the single isolated element; see Figures 5.7-5.12. The active element patterns are broader and at the higher frequencies have nulls at  $0^\circ$ . However, the isolated patterns have uniform patterns across the frequency band with their maximum at  $0^\circ$ . The active element pattern changes with input impedance. Therefore, comparison of measured data is difficult since the FDTD program does not model input impedance. However, the strong effect of mutual coupling on the active element pattern can be seen in these patterns. The mutual coupling in the array does not distort the fully excited array since the beamwidth, given by (7.3) accurately predicts the beamwidth of the fully active array given by the FDTD code. However, coupling could cause the impedance to deviate from the isolated element impedance and thus distort the scan angle. The amount of the impedance changes is directly related to the level of the mutual coupling.



**Figure 7.4** E-plane pattern of fully active 3x3 Foursquare array for frequencies from 2.0-4.0 GHz.



**Figure 7.5** H-plane pattern of fully active 3x3 Foursquare array for frequencies from 2.0-4.0 GHz.

## 7.2 Far-field Pattern Scanning

The far-field pattern of an array antenna depends on the current distribution on the antenna. If the elements of the array are weakly coupled, the element current excitations are independent of each other. However, when mutual coupling is present, element excitations are not independent. For example, mutual coupling causes element input impedance variations between elements in a finite array. However, this is not true for an infinite array because all the input impedance of every element is the same.

The radiation pattern of an array can be scanned in angular space by adding a phase taper across the elements that varies linearly with position. The variation of input impedance due to the mutual coupling will cause the current excitations to differ from a linear phase taper, resulting in a scan error. For a resonant antenna, such as the three dipoles of Fig. 6.2, simple linear array theory techniques can be used to solve for the voltage excitation that gives the desired current excitation. For broadband elements the situation is not simple. Broadband elements such as the Foursquare have multiple “modes” of excitation. Therefore, not only will the magnitude of the currents on the antenna change, the shape of the current distribution will change with position in the array. Most broadband antennas can support this type of multi-mode operation. Therefore, solving for the voltage excitation that gives the desired current phase taper at a single point on the antenna does not guarantee a correct pointing angle of an array. The effect that mutual coupling has on the scan performance of a finite 3x3 array of Foursquare elements for frequencies from 2.0 to 4.0 GHz is shown for desired scan angles of 30°, 40° and 50° in Figs. 7.6, 7.7 and 7.8. The resulting beam pointing angles are summarized in Table 7.2.

**Table 7.2** The desired versus the actual scan angles of the 3x3 Foursquare array

		<i>Actual Scan Angle (degrees, radians)</i>				
<i>Frequency (GHz)</i>		<b>2.0</b>	<b>2.5</b>	<b>3.0</b>	<b>3.5</b>	<b>4.0</b>
<i>Desired Scan Angle (degrees, radians)</i>	<b>30°</b>	14°	15°	23°	29°	29°
	<b>0.52rad</b>	0.25rad	0.26rad	0.4rad	0.5rad	0.5rad
	<b>40°</b>	17°	26°	34	37°	37°
	<b>0.70rad</b>	0.3rad	0.45rad	0.6rad	0.65rad	0.65rad
	<b>50°</b>	17°	31°	34°	34°	43°
	<b>0.87rad</b>	0.3rad	0.55rad	0.6rad	0.6rad	0.75rad
<i>Geometry of 3x3 array : h=0.5”, L=1.478”, W=0.035” and C=1.513”</i>						



The array was scanned in the H-plane where the element spacing is along the H-plane axis is 1.51 cm. The inter-element time delay was calculated for scan angles of 30°, 40° and 50° in the H-plane. In an FDTD model of an array this phase shift is represented by a time delay. A phased array beam can be scanned to a desired pointing angle by applying a relative phase shift to each of the elements in the array. The desired time delay can be found by first considering the  $n$ -th element pattern given by

$$e^{-j(\beta nd \sin \theta + \alpha_n)} \quad (7.4)$$

where  $\alpha_n$  is the phase shift at the  $n$ th element and can be found from

$$\alpha_n = -\beta nd \sin \theta_0 \quad (7.5)$$

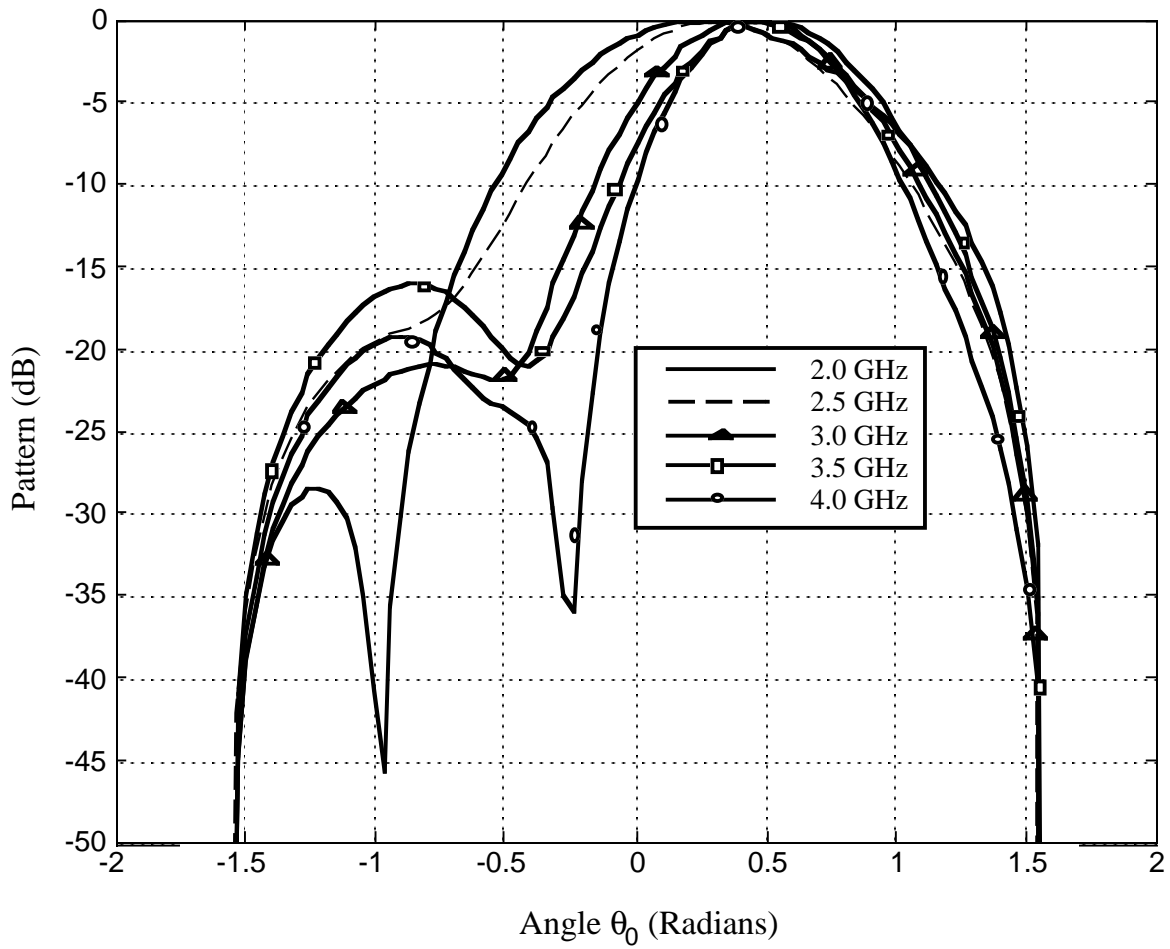
and  $\alpha_n$  can also be found from

$$\alpha_n = \omega t_n \quad (7.6)$$

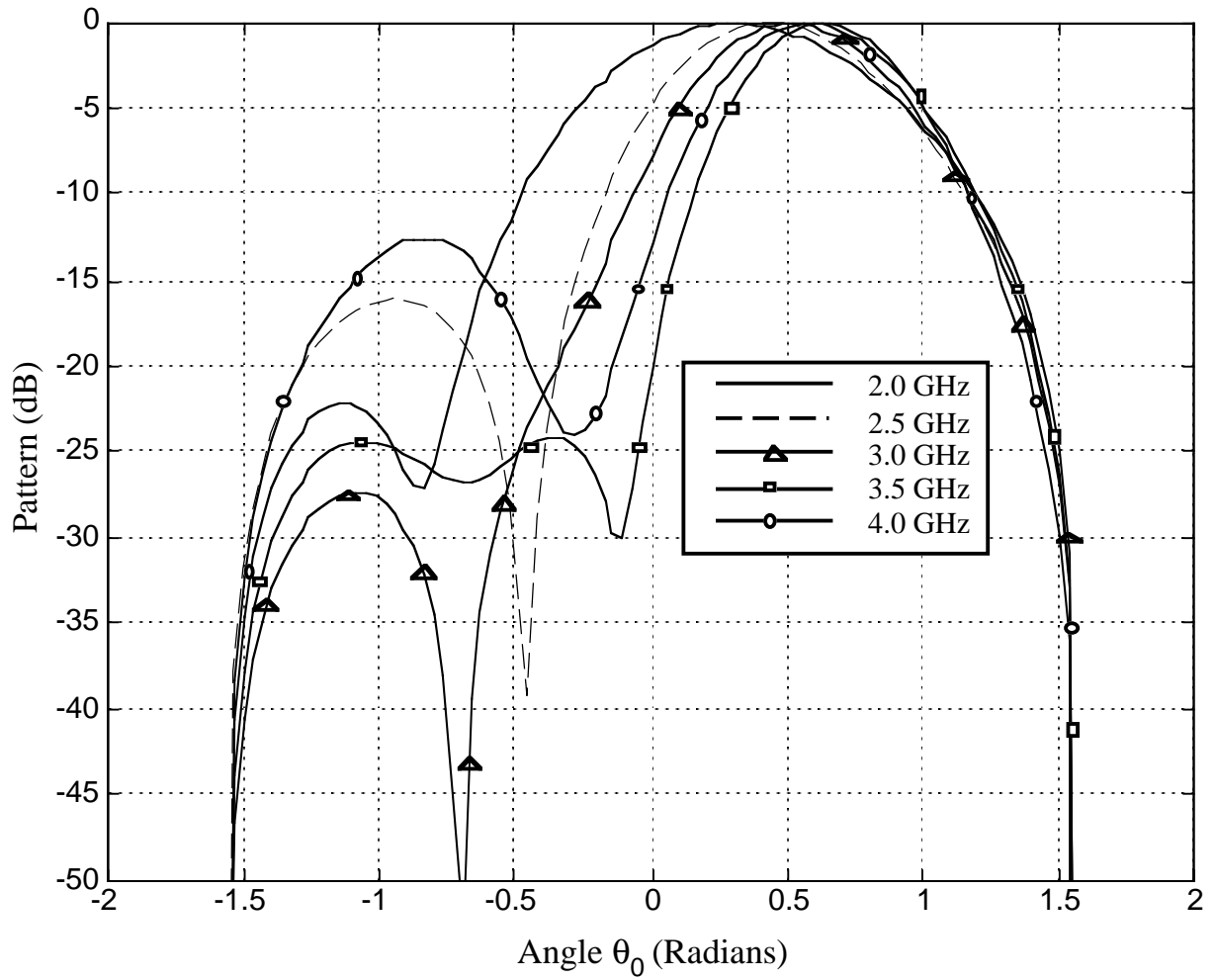
where  $t_n$  is the time delay to the  $n$ -th element. Equating (7.5) and (7.6), the time delay  $t_n$  in terms of the pointing angle  $\theta_0$  can be determined as

$$t_n = \frac{-nd \sin \theta_0}{c} \quad (7.7)$$

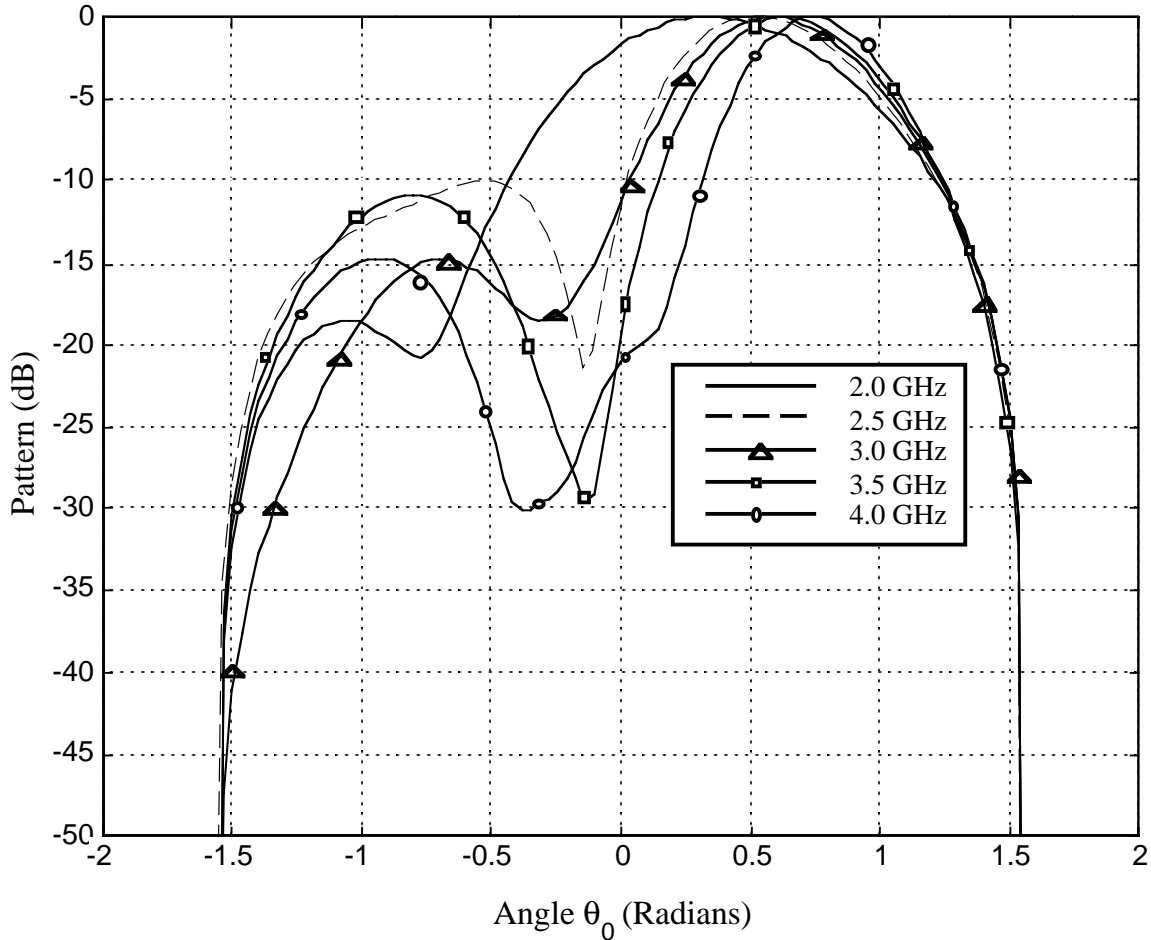
where  $c$  is the speed of light. Therefore, the time delay that is desired for each element is frequency independent. However, the phase shift is frequency dependent.



**Figure 7.6** Calculated H-plane patterns of 3x3 Foursquare array for frequencies from 2.0-4.0 GHz. The excitation voltage is for a desired scan angle of 30° or 0.52 rad.



**Figure 7.7** Calculated H-plane patterns of 3x3 Foursquare array for frequencies from 2.0-4.0 GHz. The excitation voltage is for a desired scan angle of 40° or 0.70 rad.

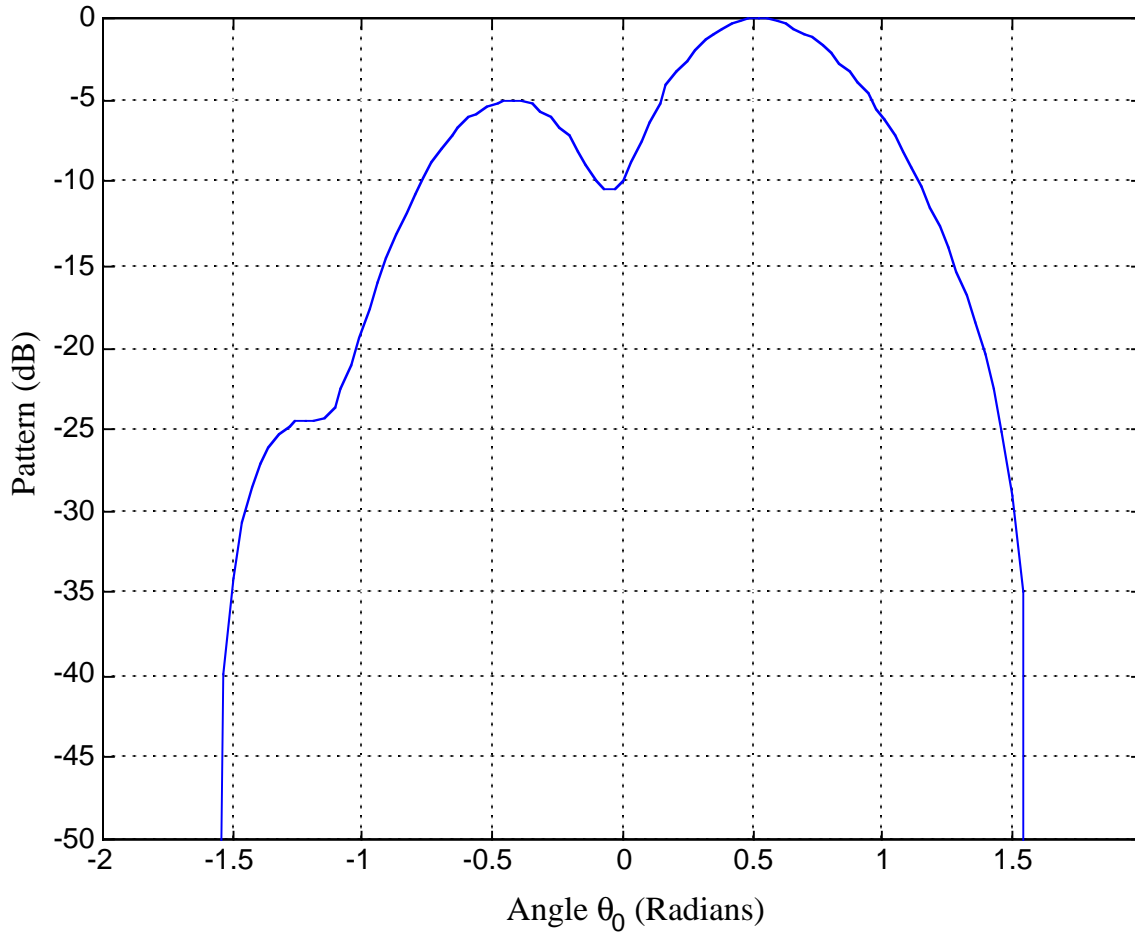


**Figure 7.8** Calculated H-plane patterns of 3x3 Foursquare array for frequencies from 2.0-4.0 GHz. The excitation voltage is for a desired scan angle of 50° or 0.87 rad.

The beam pointing effects observed for the array of Foursquare elements were also noted in Chapter 6 for the parallel dipole array. However, the strong mutual coupling between the elements of the Foursquare array make the effect much more pronounced.

The time delay between elements for the three scan angles was applied to the elements of the array for angles of 30°, 40° and 50°. The angle to which the beam scans depends on the frequency of excitation. The variation in the mutual coupling with frequency causes the scan angle to vary with frequency. The mutual coupling also reduces the scan angle as seen in Table 7.2. Compensation for reduced scan angle is possible by exciting the array with an increased phase taper. Fig. 7.9 shows the case of a

very large phase taper, 10 times that of the ideal phase taper, applied to the elements at 2.0 GHz. The beam then scans to  $30^\circ$  as shown in Fig. 7.9.



**Figure 7.9** Scanned beam of 3x3 Foursquare array with a voltage phase taper ten times larger than the expected phase taper for a  $30^\circ$  scanned beam.

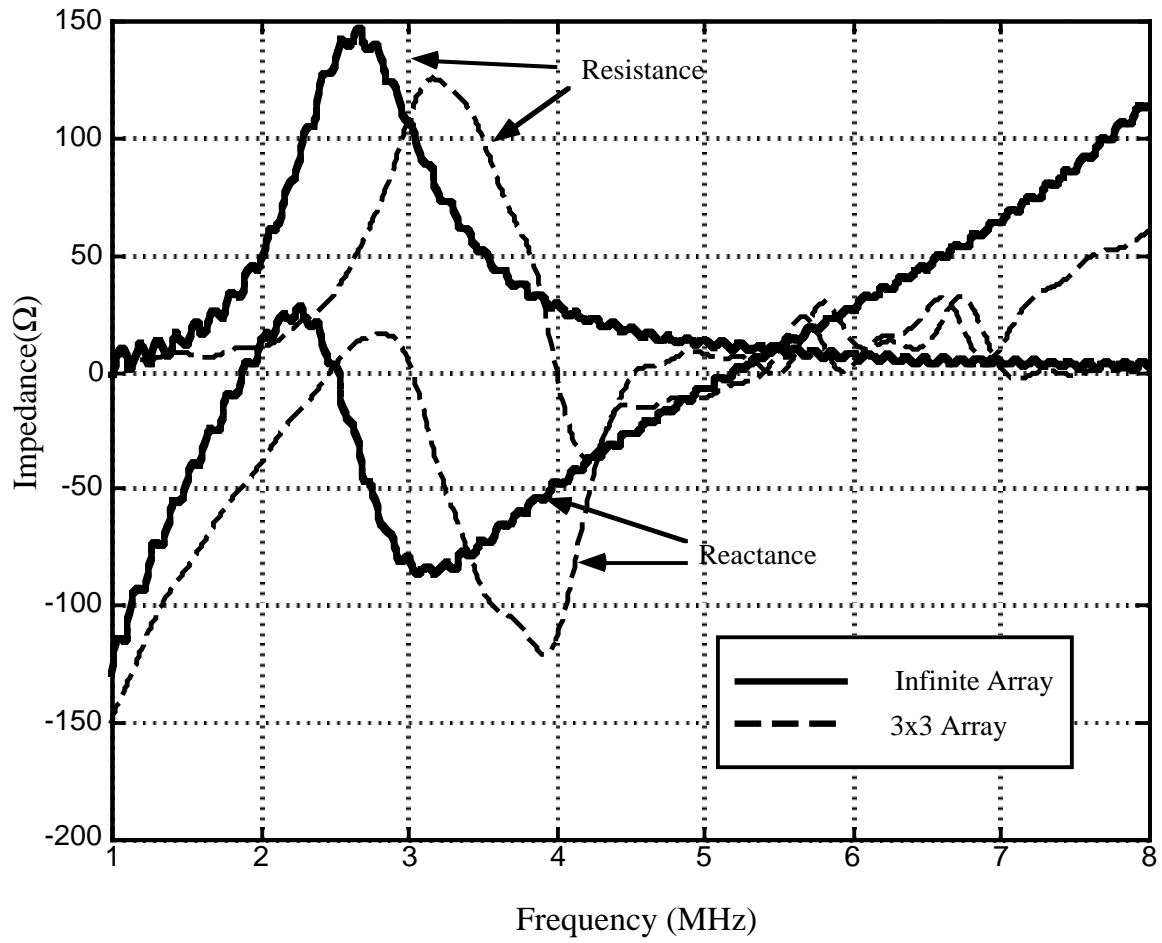
Unlike a dipole, the current on a Foursquare antenna is not confined to a specific path and therefore is largely uncontrolled by compensation methods. Compensation techniques can only enforce current at a single point. However we can assume that because larger phase tapers are required than the phase center of the elements are much further apart than predicted. Also, as seen in the dipole array, the larger the array the less

the mutual coupling inhibits the scan angle due to the uniformity of the input impedance across most of the array. In an infinite array, the phase center of the element is the same as the single isolated element. This shift in the phase center of an element in an array will not be seen in a single mode antenna such as a dipole. However, with a broadband multi-mode antenna the phase center is likely to shift significantly, as did the phase center of the Foursquare antenna

### **7.3 Input Impedance of the 3x3 Foursquare Array**

To calculate the input impedance of the modeled Foursquare array, the entire array is excited and the voltage and current ratio is calculated at the input to each of the antennas. This fully active input impedance was calculated for a 3x3 array and an infinite array. The input impedance of the center element of the 3x3 array shows a significant shift in the impedance. The input impedance of the infinite array also shows the same shift to a lower frequency of operation. The active input impedance for 1.0 – 8.0 GHz is shown in Fig. 7.10. The single isolated Foursquare element operates in a band around 6 GHz when in an array its operating frequency shifts to around 3 GHz. This shift is due to the strong mutual coupling in the array. This mutual coupling has the effect of making the element size seem bigger because it radiates at a lower frequency. The reason the element size seems larger is due to currents being excited on adjacent elements. Therefore, the elements are effectively larger, explaining the shift in the resonance to a lower frequency.

The advantage to this shift to a lower frequency of operation is that the elements stay within their  $\lambda/2$  spacing over the entire frequency band of operation. This tight spacing meets the requirements for maximum scan angles without the appearance of sidelobes. Floquet's Theorem for infinite periodic structures allows for only specular components to the scattered field no matter what the incident angle if the cell size is  $<\lambda_0/2$ . This would imply that for an infinite or very large array the mutual coupling between elements is not going to have an effect on the beam pointing angle. However, the input impedance of the array may still change.



**Figure 7.10** Active input impedance for 3x3 and infinite Foursquare array.

## INFINITE ARRAY OF FOURSQUARE ELEMENTS

Mutual coupling is very strong in an array of Foursquare elements. Numerical evaluation of the input impedance in a finite yet very large array requires a huge amount of memory and computational time. Therefore, the Foursquare antenna was modeled as an element in a uniformly excited infinite array by modifying the FDTD code as described in Chapter 4 to simulate an infinite array of antennas. Variations in the input impedance with element spacing and height above the ground plane were modeled.

### 8.1 Geometry of Arrays Investigated

The variation in the input impedance of the infinite array of Foursquare elements with height above the ground plane of  $h=7.0$  mm, 12.0 mm and 3.5 mm, was investigated. The separation between Foursquares of  $G=0.5$  mm and the other parameters listed in Table 8.1 remained constant.

The variation in the input impedance of the infinite array of Foursquare elements with separation between Foursquares of  $G=0.5$  mm, 1.0 mm, and 2.5 mm was investigated. The height above the ground plane of  $h=7.0$  mm and the other parameters listed in Table 8.1 remained constant.

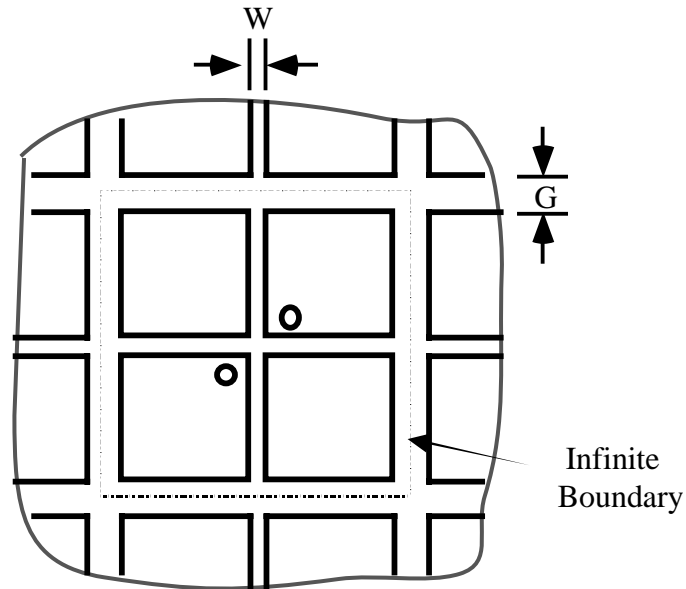


**Table 8.1** Geometry of Foursquare in an infinite array

<i>Foursquare Geometry Parameters</i>	<i>Geometry I</i>	<i>Geometry II</i>	<i>Geometry III</i>	<i>Geometry IV</i>	<i>Geometry V</i>
<i>Length of square, L</i>	10.6mm	10.6mm	10.6mm	10.6mm	10.6mm
<i>Separation between squares, W</i>	0.25mm	0.25mm	0.25mm	0.25mm	0.25mm
<i>Separation between Foursquares, G</i>	0.5mm	0.5mm	0.5mm	1.0mm	2.5mm
<i>Height above ground plane, h</i>	7.0mm	12.0mm	3.5mm	7.0mm	7.0mm
<i>Element Spacing, d</i>	11.1mm	11.1mm	11.1mm	11.6mm	13.1mm
<i>Thickness of dielectric, t<sub>d</sub></i>	0.8mm	0.8mm	0.8mm	0.8mm	0.8mm
<i>Percent Bandwidth</i>	37%	35%	25%	39%	58%

## 8.2 FDTD Model for Infinite Array Computations

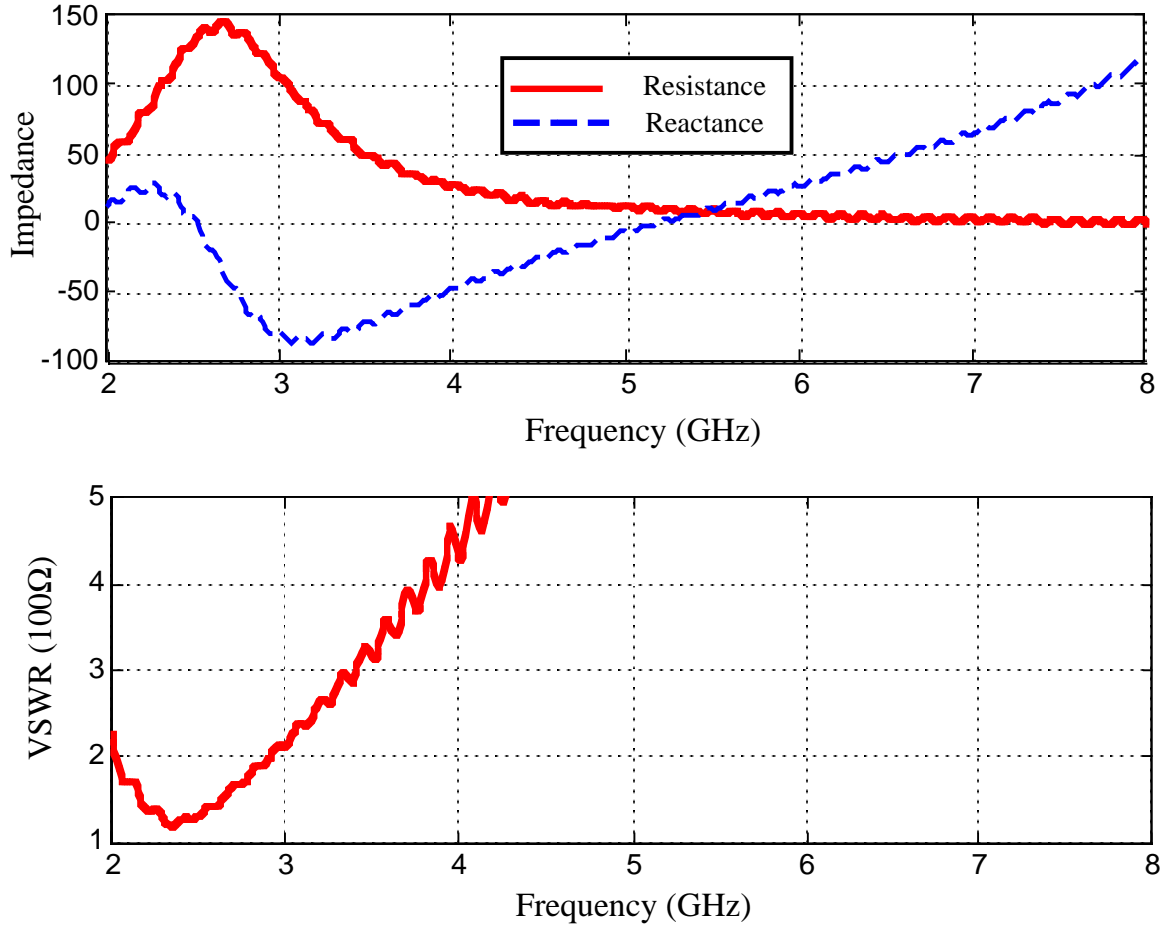
Infinite array modeling in the FDTD code requires only the geometry specifications of a single element of the array. The placement of the infinite boundary conditions in the FDTD code relative to the element determines the separation between elements in the array. For example if the separation between Foursquares is  $G=0.5\text{mm}$  the infinite boundary conditions should be placed  $0.25\text{ mm}$  from the outer edge of the squares on all four sides. The infinite array geometry is shown in Fig. 8.1 where the separation between square is  $W=0.254\text{ mm}$ , the length of the square is  $L=10.6\text{ mm}$  and the thickness of the dielectric is  $t_d=0.8\text{ mm}$ . The separation between Foursquares,  $G$ , and the height above the ground plane,  $h$ , are varied as in Table 8.1.



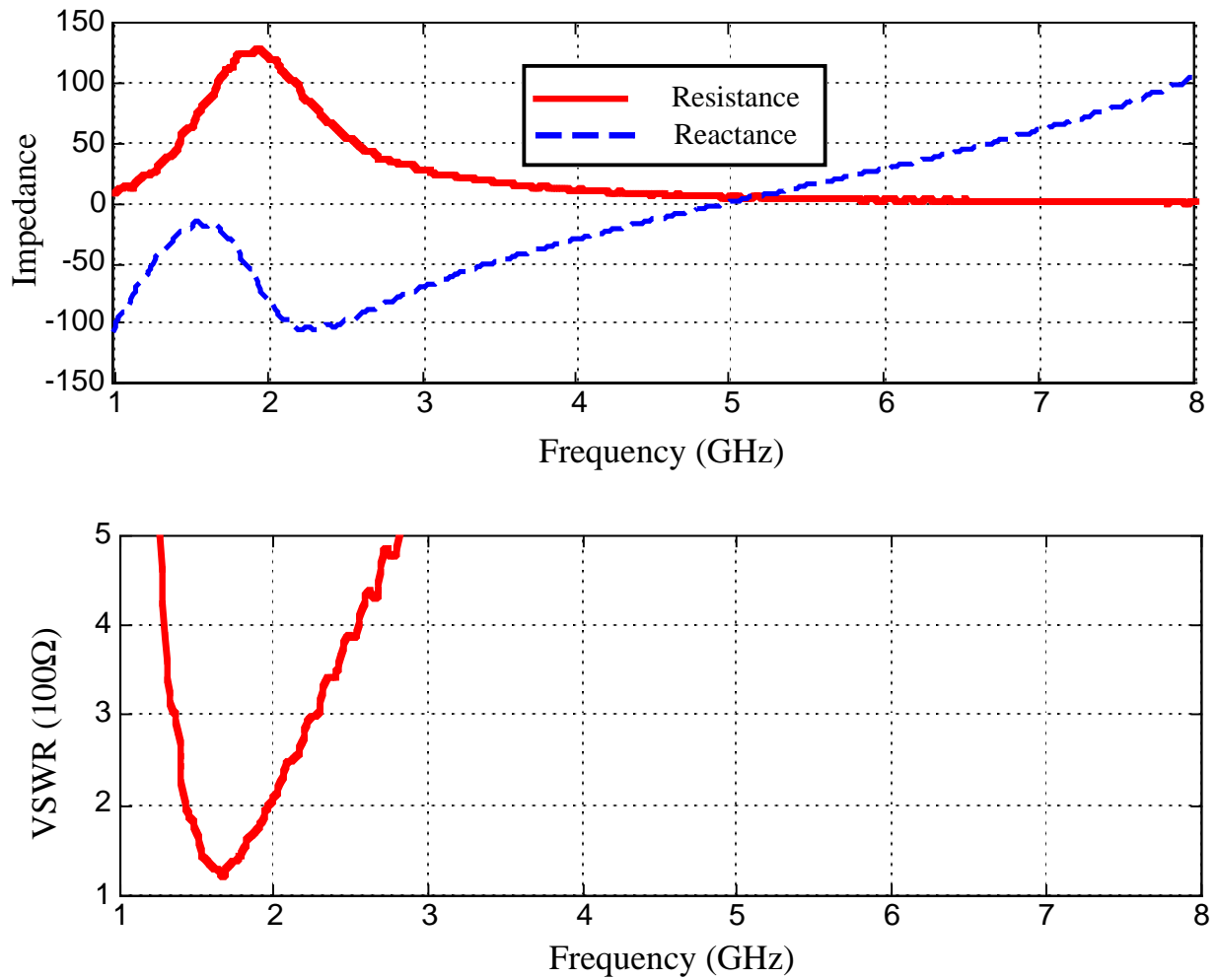
**Figure 8.1** Geometry of infinite array of Foursquare elements

### 8.3 Investigation of Height Above Ground Plane

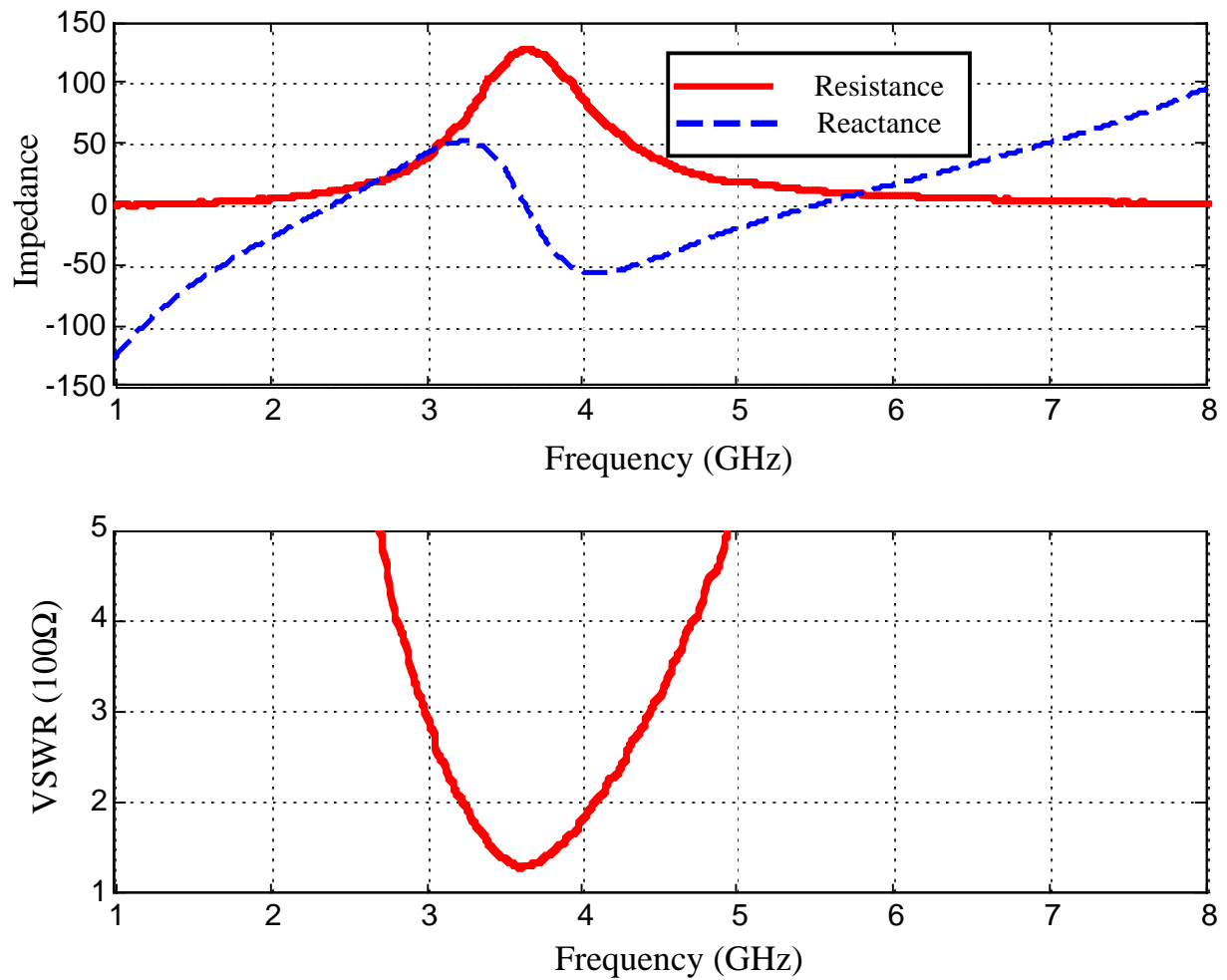
The height of the Foursquare element above the ground plane affects the operating frequency range of the Foursquare array. To observe the change in input impedance with height three arrays that varied only in height were modeled. These three array configurations are listed as Geometry I, II, and III in Table 8.1. Geometry I with element separation,  $G$ , twice that of the feed spacing,  $W$ , has a height  $h=7.0$  mm above the ground plane. Geometry II was raised to a height of  $h=12.0$  mm above the ground plane and Geometry III was lowered to a height of  $h=3.5$  mm above the ground plane. The input impedance and VSWR are shown in Figures 8.2, 8.3 and 8.4. The increased height caused the input resistance curve to shift in frequency from 2.7 GHz as seen in Fig. 8.2 to 2.0 GHz as seen in Fig. 8.3. The bandwidth relative to  $100 \Omega$  is 37% for  $h=7.0$  mm and reduces to 35% with  $h=12.0$  mm. The decreased height caused the input resistance curve to shift in frequency from 2.7 GHz as seen in Fig. 8.2 to 3.6 GHz as seen in Fig. 8.4. The bandwidth relative to  $100 \Omega$  is 37% at  $h=7.0$  mm and reduces to 25% with  $h=3.5$  mm



**Figure 8.2** Calculated input impedance and VSWR of infinite array of Foursquare elements with separation between Foursquares twice that of the separation between squares,  $W$ , as listed in Geometry I of Table 8.1. The height above the ground plane is  $h=7.0$  mm.



**Figure 8.3** Input impedance and VSWR of the infinite array of Foursquare elements with separation between Foursquares twice that of the separation between squares,  $W$ , as listed in Geometry II of Table 8.1. The height above the ground plane is  $h=12.0$  mm.

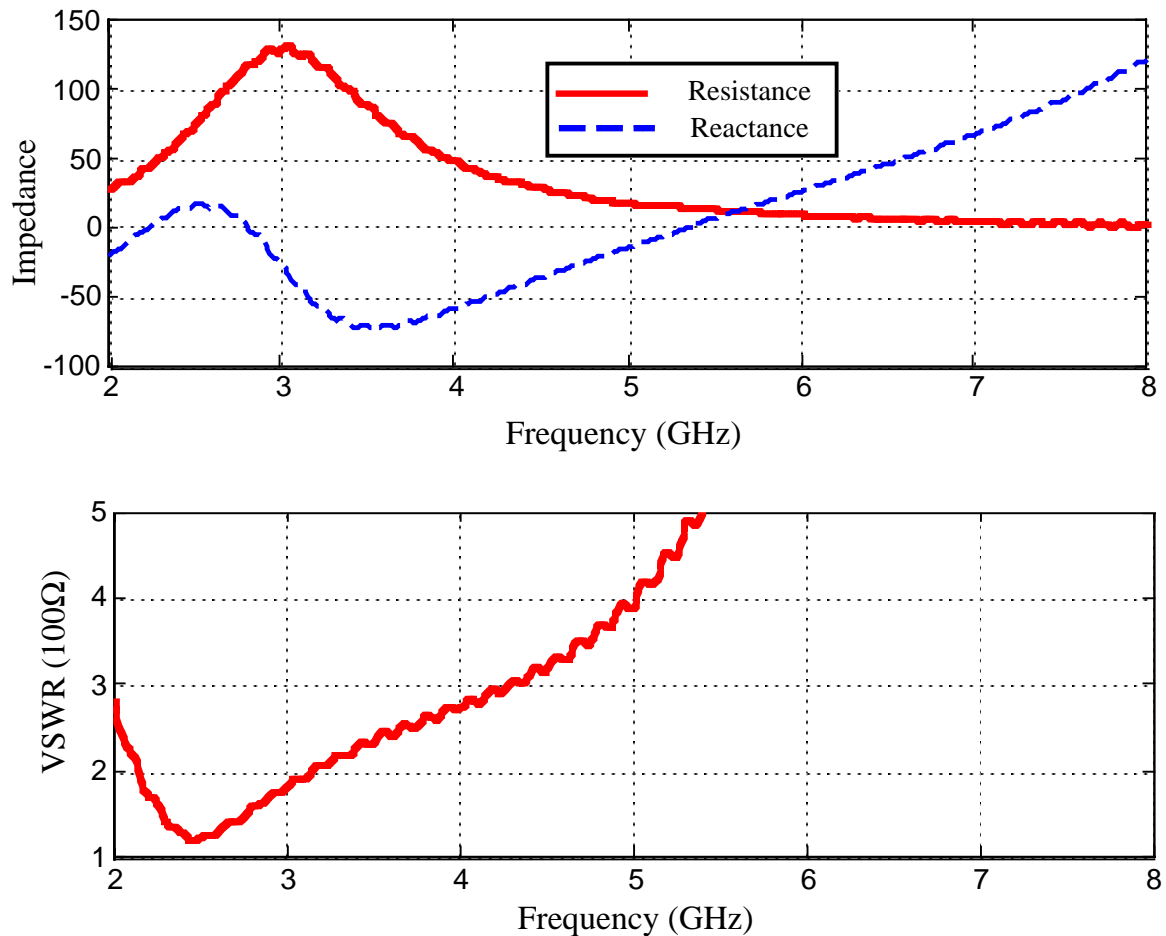


**Figure 8.4** Input impedance and VSWR of infinite array of Foursquare elements with separation between Foursquares twice that of the separation between squares,  $W$ , as listed in Geometry III of Table 8.1. The height above the ground plane is  $h=3.5$  mm.

#### 8.4 Element Spacing Variation Effects

The input impedance of the infinite Foursquare array has several parameters that affect the input impedance of the array. The effect of increased spacing between elements of the array on the VSWR bandwidth are shown in Fig 8.2 and Fig. 8.5 for Geometry I and Geometry IV in Table 8.1. The input impedance of the array of Foursquare elements

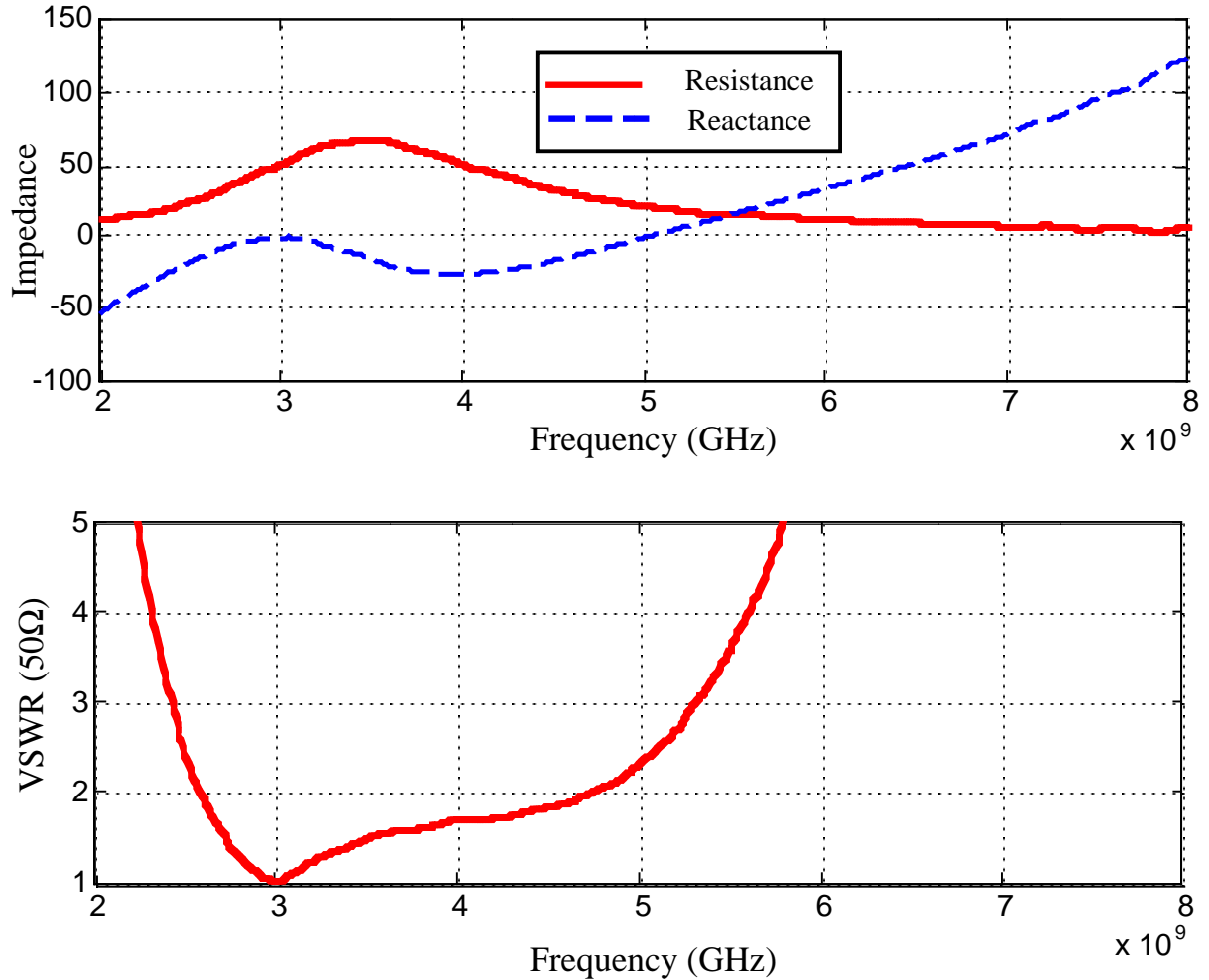
described in Chapter 5, with a separation between elements,  $G=0.5$  mm, twice that of the feed spacing,  $W=0.254$  mm, was found to have a VSWR limited by the reactance of the input impedance. Doubling the gap between the elements to  $G=1.0$  mm reduced the reactive part of the input impedance therefore increasing the VSWR bandwidth from 37% to 39%.



**Figure 8.5** Input impedance and VSWR of infinite Array of Foursquare elements with element spacing four times that of the feed spacing,  $w$  as listed in Geometry IV of Table 8.1. The height above the ground plane is  $h=7.0$  mm.

Next, the separation between elements was increased to 10 times that of the separation between squares,  $W=0.254$  mm, giving a gap,  $G=2.41$  mm. The input

impedance and VSWR are shown in Fig. 8.6. The VSWR<2 bandwidth increased from 39% to 58%. The element spacing,  $d$ , ranges from  $0.2 \lambda$  to  $0.4 \lambda$  for the 2.6 to 4.7 GHz operating range.



**Figure 8.6** Input impedance and VSWR of infinite Array of Foursquare elements with element spacing four times that of the feed spacing,  $w$  as listed in Geometry V of Table 8.1. The height above the ground plane is  $h=7.0$  mm.

## 8.5 Summary

Increasing the height from  $h=7.0$  mm to  $h=12.0$  mm above the ground plane does not yield a significant change in bandwidth and therefore does not show much promise for use in optimizing the bandwidth of the array. Furthermore, decreasing the height from  $h=7.0$  mm to  $h=3.5$  mm above the ground plane reduces the bandwidth, from 37% to 25%. However, there is a significant increase in bandwidth with the increased gap,  $G$ , between the elements. For maximum scanning capability, the element spacing is required to be less than  $0.5 \lambda$  over the operating band of the array. The element spacing is less than  $0.5 \lambda$  even with a gap between elements 10 times greater than that of the feed spacing,  $W$ .



## **SUMMARY AND CONCLUSIONS**

This dissertation discussed the beneficial effects of strong mutual coupling in arrays and in the Foursquare antenna. Previous array research has concentrated on eliminating the effects of mutual coupling in arrays see Chapter 2. A description of the operating characteristics of the Foursquare antenna is given in Chapter 2 and 5 along with other broadband elements. Chapter 3 discusses the consequences of choosing a relatively large broadband element for use in a broadband array and the effect the required increased spacing will have on the achievable scanning bandwidth of the array. The FDTD code to model the Foursquare antenna as an element and an array is discussed in Chapter 4. The effects of strong mutual coupling in arrays, such as impedance change, resonant frequency shift and reduced element spacing was demonstrated with simple dipole arrays and transmission line models in Chapter 6. These same mutual coupling effects are seen in the 3x3 Foursquare array model of Chapter 7 and the infinite Foursquare array model of Chapter 8. Original contribution from this work include:

- The broadband operating characteristics of the Foursquare antenna were explained by the strong mutual coupling between the diagonally excited squares and the parasitic squares (Chapter 5)
- Through numerical analysis, a shift in resonant frequency of antennas, in particular the Foursquare antenna, placed in a strongly coupled array was predicted and demonstrated.
- An increase in the effective size of the element due to mutual coupling by radiation from adjacent elements was demonstrated.

- Through numerical analysis, an increase in impedance bandwidth of the Foursquare element in an infinite array due to strong mutual coupling was predicted and demonstrated.
- Through numerical analysis, a decreased element spacing, achieved because of the downward shift in resonant frequency of the element in an array environment, was predicted and demonstrated.
- A numerical methods code was developed, specifically the FDTD code, for modeling the characteristics of the Foursquare antenna in a infinite array.

Continuing research into the operating characteristics of strongly coupled broadband arrays:

- The relative phase between the induced voltages due to the surrounding elements will vary with scan angle. Therefore, the input impedance of the element in the fully active array will vary with scan angle. Investigation of the input impedance variation with scan angle of a strongly coupled array may be necessary to optimize the feed design for the desired scan capability.
- Broadband elements require broadband balanced feeds. It is not trivial to design a low cost, broadband balanced feed. Therefore, development of a low cost, broadband balanced feed would be a valuable research contribution.

## REFERENCES

- [1] Jerry E. Boyns and J.H. Provencher, "Experimental results of a multifrequency array antenna," IEEE Trans. Antennas Propogat.,pp.106-107, Jan. 1972.
- [2] Laughlin, Gordon J.; Byron, Eugene V.; and Cheston, T.C.; "Very wideband phased array antennas", IEEE Transactions on Antennas and Propagation, Vol. AP-20, No. 6, November 1972.
- [3] S. J. Foti and M. W. Shelley, "An experimental wide band polarization diverse phased array," 1998
- [4] Kuan Min Lee, Allen T.S. Wang, and Ruey Shi Chu, "Dual-band, Dual-polarization, interleaved cross-dipole and cavity-backed disc elements phased array antenna," IEEE Ant. & Prop. Soc. Symp. (Montreal) pp. 694-697, July 1997.
- [5] Peter C. Strickland, "A dual-polarized, dual-band array for spaceborne SAR," North American Radio Science Meeting of URSI (Montreal ), pp. 204,July 1997.
- [6] Ralph Pokuls, Jaroslaw Uher D. M. Pozar, "Dual-frequency and dual-polarization microstrip antennas for SAR applications," IEEE transactions on Antennas and Propagation, pp.1289-1296 vol. 46,NO.9 Sept. 1998.
- [7] R. Gilbert, G. Pirrung, D. Kopf, P. Hoe3fler, F. Hayes, "Structurally-integrated optically-reconfigurable antenna array," Sept. 1995.
- [8] Leanard Mansky, (1984)"Broadband phased-array antennas,"
- [9] Mark J. Povinelli and C. Edward Grove , " Wideband apertures for active planar multifunction phased arrays," 1989.
- [10] Daniel H. Schaubert,"A Gap-induced element resonance in single polarized arrays of notch antennas," IEEE Ant. & Prop. Soc. Symp. Digest (Seattle), June 1994.
- [11] Ramakrishna Janaswamy and Daniel H. Schaubert, "Analysis of the tapered slot antenna," IEEE Transactions on Antennas and Propagation, vol. AP-35,September 1987.
- [12] Ehud Gazit, "Improved design of the Vivaldi antenna," IEE Proceedings, vol. 135, pp. 89-92, April 1988.
- [13] J. D. S. Langley, P. S. Hall, P. Newham, "Balanced antipodal Vivaldi antenna for wide bandwidth phased arrays," IEE Proceedings-Microwave Antennas Propagation, Vol. 143, April 1996.

- [14] Timothy A. Axness, Robert V. Coffman, Bruce A. Kopp, and Kenneth W. O'Haver, "Shared Aperture Technology Development," Johns Hopkins APL Technical digest, Vol. 17, 1996.
- [15] W. S.T. Rowe and R. B. Waterhouse, "Broadband CPW fed stacked patch antenna,"
- [16] K. Ghorbani and R.B. Waterhouse, "Design of large broadband patch arrays," IEEE Ant. And Prop. Soc. Inter. Symp. Digest (Orlando), July 1999.
- [17] Allen T. S. Wang, Ruey-Shi Chu, Kuan Min Lee, "Planar, low-profile, wideband, wide-scan phased array antenna using stacked-disc radiator," IEEE Ant. & Prop. Soc. (Montreal), pp. 702-705, July 1997.
- [18] W. L. Stutzman and G. A. Thiele, Antenna Theory and Design, Second Edition, John Wiley: New York, 1998.
- [19] D. G. Shively and W. L. Stutzman, "Wideband arrays with variable element sizes," IEE Proc.-Part H: Microwaves, Antennas, and Propagation, vol. 137, pp. 238-240, August 1990.
- [20] C. G. Buxton and W. L. Stutzman, "Implementation of the Foursquare antenna in broadband arrays," URSI National Radio Science Meeting (Orlando, FL), July 1999.
- [21] J.Randall Nealy, "Foursquare Antenna Radiating Element" U.S. Patent No. 5,926,137, July 20, 1999.
- [22] Tai-Tseng Chu and H. George Oltman Jr., " The sinuous antenna," Microwave Systems News and Communication Technology, vol. 18, pp. 40-48, June 1988.
- [23] Yee, K. S., "Numerical solution of initial boundary value problems involving Maxwell's equations in isotropic media," IEEE Trans. Antennas and Propagation, vol. 14, 1966, pp. 302-307.
- [24] Allen Taflove, Computational Electromagnetics, The Finite Difference Time Domain Method, Artech House, Inc.: Norwood , MA, 1995.
- [25] Gedney, S., "An anisotropic perfectly matched layer absorbing media for the truncation of FDTD lattices," IEEE Trans. Antennas and Propagation, Vol.44, 1996, pp. 1630-1639.
- [26] J. P. Berenger, " A perfectly matched layer for the FDTD solution of wave-structure interaction problems," IEEE Trans. Antennas and Propagation, , Vol. 44, 1996, pp. 110-117.

- [27] Allen Taflove, *Advances in Computational Electromagnetics, The Finite Difference Time Domain Method*, Artech House, Inc.: Norwood , MA, 1998.
- [28] W. L. Stutzman, W. A. Davis, J. W. LaPean, Jr., Randall Nealy, Gerry Ricciardi and J. M. Monkevich, "A Study of Elements for Use in Wideband Array Antenna Systems: Phase 2 – Log-periodic Radiator Development," Report No. 96-1, May 1996.
- [29] W. A. Davis, J. R. Nealy, G. F. Ricciardi and W. L. Stutzman, "Techniques for the Measurement of the Impedance of Wideband Balanced Antennas", *Proceedings of the Antenna Measurement Techniques Association Symposium*, (Williamsburg,VA), Nov. 1995.
- [30] David M. Pozar, *Microwave Engineering*, Addison-Wesley Publishing Company, Inc, 1990.
- [31] W. A. Davis, "WIRE," ver. 1.40, Blacksburg, VA; VA Tech, Mar. 1995
- [32] Robert J. Mailloux, *Phased Array Antenna Handbook*, Boston: Artech House, 1994
- [33] D. M. Pozar, "The active element pattern," *IEEE Trans. Antennas Propagat.*, vol. AP-42, pp.1176-1178, Aug. 1994.
- [34] D. M. Pozar and D. H. Schaubert, "Scan Blindness in infinite phased arrays of printed dipoles," *IEEE Trans. Antennas Propagat.*, vol. AP-32, pp.602-610, Oct. 1984.
- [35] J. L. Allen, "Gain and impedance variations in scanned dipole arrays," *IRE Trans. Antennas Propagat.*, vol. AP-10, pp. 566-572, Sept. 1962.
- [36] D. M. Pozar, "Analysis of finite phased arrays of printed dipoles," *IEEE Trans. Antennas Propagat.*, vol. AP-33, pp.1045-1053, Oct. 1985.
- [37] S. Edelberg and A. A. Oliner, "Mutual coupling effects in large antenna arrays: Part I - Slot arrays," *IRE Trans. Antennas Propagat.*, vol. AP-8, pp. 286-297, May. 1960

## VITA

Carey G. Buxton was born in Lexington, Kentucky on November 6, 1970. She attended the University of Kentucky from August 1988 through August 1994 where she received her degree of Bachelor of Electrical Engineering, Summa Cum Laude. While an undergraduate student at the University of Kentucky she participated in the cooperative education program and worked for five semesters at NASA Langley Research Center. As an undergraduate she participated in the NSF Research Experience for Undergraduates program.

August of 1994, Carey enrolled in the Master's Degree program at the University of Kentucky supported by a NSF Fellowship. She specialized in Electromagnetic Compatibility and Numerical Electromagnetics. She obtained her Master's Degree December 1996.

August of 1996 Carey began her doctorate degree at Virginia Polytechnic Institute and State University. She was supported by the Electrical and Computer Engineering department's Bradley Fellowship.

Carey is a member of Eta Kappa Nu, Tau Beta Pi and the Institute of Electrical and Electronics Engineers.